UNIVERSIDADE ESTADUAL PAULISTA "JÚLIO DE MESQUITA FILHO"
CAMPUS DE PRESIDENTE PRUDENTE
FACULDADE DE CIÊNCIAS E TECNOLOGIA
Programa de Pós-Graduação em Ciências Cartográficas

FROM OLIGO TO EUTROPHIC INLAND WATERS: ADVANCEMENTS AND CHALLENGES FOR BIO-OPTICAL MODELING

Presidente Prudente

2017

THANAN WALESZA PEQUENO RODRIGUES

FROM OLIGO TO EUTROPHIC INLAND WATERS: ADVANCEMENTS AND CHALLENGES FOR BIO-OPTICAL MODELING

Thesis presented to the Department of Cartography of the Faculty of Science and Technology of São Paulo State University as part of the requirements for obtaining the PhD degree in Cartographic Sciences.

Advisor: Prof. Dr. Nilton Nobuhiro Imai
Co-Advisor: Prof. Dr. Enner Herenio de Alcântara

Presidente Prudente

2017

FICHA CATALOGRÁFICA

Rodrigues, Thanan Walesza Pequeno.
R617f From oligo to eutrophic inland waters: advancements and challenges for bio-optical modeling / Thanan Walesza Pequeno Rodrigues. - Presidente Prudente : [s.n.], 2017
145 f. : il.

Orientador: Nilton Nobuhiro Imai
Coorientador: Enner Herenio de Alcântara
Tese (doutorado) - Universidade Estadual Paulista, Faculdade de Ciências e Tecnologia
Inclui bibliografia

1. Modelagem bio-óptica. 2. Águas interiores. 3. Sensoriamento remoto da água. 4. Sistema de reservatórios em cascata. I. Rodrigues, Thanan Walesza Pequeno. II. Imai, Nilton Nobuhiro. III. Alcântara, Enner Herenio de. IV. Universidade Estadual Paulista. Faculdade de Ciências e Tecnologia. V. Título.

UNIVERSIDADE ESTADUAL PAULISTA

Câmpus de Presidente Prudente

CERTIFICADO DE APROVAÇÃO

TÍTULO DA TESE: FROM OLIGO TO EUTROPHIC INLAND WATERS: ADVANCEMENTS AND CHALLENGES FOR BIO-OPTICAL MODELING

AUTORA: THANAN WALESZA PEQUENO RODRIGUES
ORIENTADOR: NILTON NOBUHIRO IMAI
COORIENTADOR: ENNER HERENIO DE ALCÂNTARA

Aprovada como parte das exigências para obtenção do Título de Doutora em CIÊNCIAS CARTOGRÁFICAS, área: AQUISIÇÃO, ANÁLISE E REPRESENTAÇÃO DE INFORMAÇOES ESPACIAIS pela Comissão Examinadora:

Prof. Dr. NILTON NOBUHIRO IMAI
Departamento de Cartografia / Faculdade de Ciencias e Tecnologia de Presidente Prudente

Prof. Dr. DEEPAK RANJAN MISHRA
Departament of Geography / University of Georgia

Prof. Dr. ARCILAN TREVENZOLI ASSIREU
Instituto de Recursos Naturais / Universidade Federal de Itajubá

Profa. Dra. MARIA DE LOURDES BUENO TRINDADE GALO
Departamento de Cartografia / Faculdade de Ciencias e Tecnologia de Presidente Prudente

Profa. Dra. FERNANDA SAYURI YOSHINO WATANABE
Pós-doutoranda / Faculdade de Ciencias e Tecnologia de Presidente Prudente

Presidente Prudente, 09 de março de 2017

To God.

To my beloved parents Waldete and Salatiel

To my beloved husband Ulisses

To my dear sisters and brother Suzan, Rejane and Walesson.

AGRADECIMENTOS

Agradeço antes de tudo à Deus por ter me concedido grandes oportunidades e me dado forças para sempre prosseguir. A caminhada durante o doutorado foi árdua e sem ele nada teria valido a pena. Nessa jornada contei com ajuda e colaboração de muitas pessoas e a elas eu expresso meus sinceros agradecimentos em especial:

A meus pais que tanto amo Waldete e Salatiel por me fazerem chegar onde estou hoje sem medirem esforços, agradeço a dedicação incondicional, amor e ensinamentos passados ao longo de toda minha vida.

Aos meus irmãos Waleska, Walesson e Rejane pelo companheirismo, amizade e amor.

A meu marido e amigo Ulisses que sempre esteve presente na minha caminhada acadêmica e profissional me incentivando e apoiando as decisões mais difíceis.

Aos meus tios e primos queridos: Cris, Walmir, Waldemir, Heloisa, Amandinha, Adonis e Ágatha.

Ao meu orientador Dr. Nilton Imai pelas contribuições e por ter possibilitado meu ingresso no Programa de Pós-Graduação da Unesp.

Ao meu co-orientador Dr. Enner Alcântara, profissional que realmente se dedica à pesquisa e ciência, que me incentivou desde o princípio a escrever e acreditar no meu potencial como pesquisadora.

Ao Dr. Deepak Mishra da Universidade da Geórgia, Estados Unidos, pelo exemplo de pesquisador, e que me ajudou, durante o período sanduíche, com discussões sobre a tese e artigos e que me inseriu no seu grupo de pesquisa em Athens. Agradeço ainda o Departamento de Geografia da UGA por ter concedido ajuda de custo para participar de um evento na cidade de São Francisco.

Agradeço a todos os meus colegas e grandes parceiros do grupo de pesquisa em Sensoriamento Remoto da água, em especial: Fernanda, Luiz, Nariane, Alisson, Bruno, Stela, Carol Ambrósio e todos aqueles que direta ou indiretamente fizeram com que as análises e campos ocorressem. Agradeço ainda a todos os meus colegas de Pós-Graduação que me ajudaram a sobreviver no primeiro ano de doutorado seja em sala de aula ou jogando vôlei de areia ou ainda futebol.

Agradeço ao Dr. Cláudio Clemente do INPE pelos equipamentos emprestados nos primeiros campos. Agradeço ainda o Renato e Daniel pela ajuda nos campos e nas análises laboratoriais.

Ao Dr. Edivaldo Velini e técnicos da Unesp Botucatu, por nos deixar utilizar os equipamentos para análises laboratoriais.

A todos os professores do PPGCC por todo ensinamento e discussões, em especial: as Professoras Lourdes, Ivana e Vilma pelas contribuições na tese e em artigos escritos com colaboração.

Aos meus colegas Ike e Kumar por ter tornado minha vida mais fácil nos EUA, e por terem me ajudado com discussões relacionados aos artigos. Agradeço ainda a Dipanwita e Shuvo pela gentileza e por terem me apresentado a cultura indiana. Agradeço também ao Benjamin pelas discussões relacionadas a programação ou mesmo com o idioma inglês.

Agradeço a CAPES pela concessão da bolsa de doutorado (Processo n° 1193768), ao CNPq pela concessão da bolsa sanduíche (Processo nº 200152/2015-7 - SWE) e por financiar projetos (Processos nº 472131/2012-5 e 400881/2013-6) e à FAPESP pelos projetos (Processos n° 2012/19821-1 e 2015/21586-9).

Por fim agradeço à Unesp e o PPGCC pela infraestrutura e suporte para estudo. Agradeço ainda os funcionários da Unesp, em especial a Cinthia, André e Ivonete da Secretaria da Pós-Graduação.

Obrigada a todos!

“We must have perseverance and above all confidence in ourselves. We must believe that we are gifted for something and that this thing must be attained.”

(Marie Curie)

RESUMO

O presente trabalho teve como objetivo realizar um levantamento detalhado das características bio-ópticas nos reservatórios de Barra Bonita (BB) e Nova Avanhandava (Nav) com o intuito de avaliar o desempenho de uma única abordagem voltada para a estimativa das propriedades ópticas inerentes (POIs), assim como, a concentração de totais sólidos suspensos (TSS). A investigação foi realizada utilizando dados coletados no campo entre 2014 e 2016, incluindo, as POIs, componentes opticamente significativos (COSs) e reflectância de sensoriamento remoto (R_{rs}). Os dados apresentados dos COSs confirmaram que BB é um ambiente mais túrbido que Nav por apresentar maior produção fitoplanctônica em função do recebimento de altas cargas de nutrientes provenientes da bacia de drenagem. Por outro lado, Nav é um ambiente mais transparente e com maior influência de material inorgânico, o que favorece o surgimento de macrófitas submersas. A concentração de clorofila-*a* (Chl-*a*) em BB alcançou máximo de 797.8 µg l^{-1} em outubro/2014, enquanto Nav apresentou máximo de 38.6 µg l^{-1} em maio/2016. A variabilidade nos COS esteve altamente vinculada a frequência de chuvas, sendo que no ano de 2014, ocorreu um evento extremo de seca alterando as características biogeoquímicas dos ambientes. BB reagiu de forma mais abrupta que Nav por apresentar um sistema de operação do tipo acumulação e por estar mais próxima das regiões potencialmente poluidoras, diferente de Nav que apresenta um sistema fio-d'água em que não há acumulação e sim fluxo constante da água. Além disso, no âmbito óptico, a absorção em Nav apresentou maior influência do particulado não-algal (NAP) enquanto que em BB, a absorção foi dominada por fitoplâncton. Com base nesses resultados pode-se concluir que os dois ambientes apresentam não só diferenças na qualidade da água, mas também nas propriedades ópticas, o que leva a afirmação de que um modelo único baseado nos dois ambientes pode não ter um bom resultado quando se pretende utilizar uma abordagem empírica. Um algoritmo quase-analítico (QAA) parametrizado para as condições de Nav (QAA_{OMR}) apresentou resultados significativos com erros (erro médio percentual absoluto – MAPE) inferiores a 17% para o coeficiente de absorção total (a_t), 19% para o coeficiente de absorção orgânico detrital (a_{CDM}) e 47% para o coeficiente de absorção do fitoplâncton (a_ϕ). O respectivo modelo foi utilizado para verificar seu desempenho em um ambiente eutrofizado como BB e a versão parametrizada por Watanabe et al. (2016) e denominada QAA_{BBHR} foi aplicada aos dados de Nav. Como resultado, observamos que as duas versões foram adequadas para estimar a_t com erros inferiores a 40%, no entanto, existe ainda a necessidade de melhorar as etapas para estimativa de a_{CDM} e a_ϕ. No caso de se aplicar um modelo empírico de única abordagem para estimar concentração de TSS para ambos os reservatórios, observamos que essa abordagem não apresentou resultados satisfatórios, portanto, modelos específicos baseados na banda do vermelho do MODIS foram utilizados para mapear TSS em cada um dos reservatórios. Pode-se concluir então, que o conhecimento acerca das propriedades ópticas da água se mostrou determinante para a modelagem bio-óptica, principalmente no que diz respeito aos ambientes altamente contrastantes como BB e Nav.

Palavras-chave: modelagem bio-óptica, águas interiores, sensoriamento remoto da água, sistema de reservatórios em cascata

ABSTRACT

The objective of the present work was to perform a detailed survey of the bio-optical characteristics of the reservoirs of Barra Bonita (BB) and Nova Avanhandava (Nav) in order to evaluate the performance of a single approach aimed at estimating the inherent optical properties (IOPs), as well as the concentration of total suspended solids (TSS). The research was carried out using data collected in the field between 2014 and 2016, including the IOPs, optically significant components (OSCs) and remote sensing reflectance (R_{rs}). The data presented from the OSCs confirmed that BB is more turbid than Nav because it presents higher phytoplankton production due to the input of high nutrient loads from the drainage basin. On the other hand, Nav is more transparent with greater influence of inorganic matter, which favors the appearance of submerged macrophytes. The concentration of chlorophyll-a (Chl-*a*) in BB reached a maximum of 797.8 μg l^{-1} in October/2014, while Nav presented a maximum of 38.6 μg l^{-1} in May/2016. The variability in the COS was highly related to the frequency of rainfall, in the year 2014, an extreme drought event occurred, altering the biogeochemical characteristics. BB reacted more abruptly than Nav because it presented an accumulation type operation system and because it is closer to the potentially polluting region. Nav presents a water system in which there is no accumulation but constant flow of water. In addition, in the optical context, the absorption in Nav presented greater influence of the non-algal particulate (NAP) while in BB, the absorption was dominated by phytoplankton. Based on these results, it can be concluded that the two environments present not only differences in water quality but also in optical properties, which leads to the assertion that a single model based on the two environments may not have a good result when it is intended to use empirical approach. A quasi-analytical algorithm (QAA) parameterized for Nav conditions (QAA_{OMR}) presented significant results with errors (mean absolute percentage error - MAPE) lower than 17% for the total absorption coefficient (a_t), 19% for the carbon detrital matter absorption coefficient (a_{CDM}) and 47% for the absorption coefficient of phytoplankton (a_ϕ). The respective model was used to verify its performance in a eutrophic environment such as BB and the version parameterized by Watanabe et al. (2016) and named QAA_{BBHR} was applied to the Nav data. Thus, we note that the two versions were suitable for estimating a_t with errors (MAPE) less than 40%, however, improvements must be carried out for estimating a_{CDM} and a_ϕ. In the case of applying a single empirical model to estimate TSS concentration for both reservoirs, we observed that it did not present satisfactory results, so specific models based on the MODIS red band were used to map TSS in each of the reservoirs. It can be concluded, therefore, that knowledge about the optical properties of water has proved to be determinant for the bio-optical modeling, especially with respect to highly contrasting environments such as BB and Nav.

Keywords: bio-optical modeling, inland waters, remote sensing of water, reservoirs in cascade system

LIST OF FIGURES

Figure 2.1. Graphic representation of the study area emphasizing (a) Brazil's territory, (b) Tietê River located at São Paulo State and the location of the reservoirs from upstream to downstream: Barra Bonita, Bariri, Ibitinga, Promissão, Nova Avanhandava and Três Irmãos, (c) sampling location of Nav and (d) BB. 25

Figure 2.2. Flowchart showing the methodological scheme for sampling stations definition. ρTOA represents the value of reflectance at the top of atmosphere (TOA), SD stands for the standard deviation, NDWI is the Normalized Difference Water Index, and PCA is the Principal Component Analysis. The box 1 refers to the multispectral images; box 2 stands for the reservoir's delimitation and box 3, stratified sampling. 27

Figure 2.3. Rainfall data from the period between 2011 to 2016 (boxplots) highlighting the years of 2014, 2015 and 2016 for (a) Nav and (b) BB. Nav1 (28 April – 2 May/2014), Nav2 (23 – 26 September/2014) and Nav3 (9 and 14 May/2016). 30

Figure 2.4. Water level data from the period between 2011 to 2016 (boxplots) highlighting the years of 2014, 2015 and 2016 for (a) Nav and (b) BB. Different axis y was used due to distinct magnitudes. Nav1 (28 April – 2 May/2014), Nav2 (23 – 26 September/2014) and Nav3 (9 and 14 May/2016). 31

Figure 2.5. Water flow data from the period between 2011 to 2016 (boxplots) highlighting the years of 2014, 2015 and 2016 for (a) Nav and (b) BB. Nav1 (28 April – 2 May/2014), Nav2 (23 – 26 September/2014) and Nav3 (9 and 14 May/2016). 32

Figure 3.1. Relationship between water quality and optical parameters considering data from all field campaigns. (a) TSS versus Chl-*a*, (b) $a_\phi(443)$ versus Chl-*a*, (c) $a_{NAP}(443)$ versus TSS, (d) $a_{CDOM}(443)$ versus TSS and (e) $a_{CDOM}(443)$ versus Chl-*a*. 41

Figure 3.2. Ternary plot depicting the absorption coefficient budget of both Nav and BB reservoirs at three wavelengths: (a) 443 nm, (b) 560 nm and (c) 665 nm. 42

Figure 3.3. Variability of $a_{CDOM}$by field trip. (a) Nav1, (b) Nav2, (c) Nav3, (d) BB1, (e) BB2 and (f) the average value of $a_{CDOM}(\lambda)$ for each field trip. Different y axes were applied for Nav and BB due to magnitude discrepancies. 43

Figure 3.4. Variability of $a_\phi$by field trip. (a) Nav1, (b) Nav2, (c) Nav3, (d) BB1, (e) BB2 and (f) the average value of $a_\phi(\lambda)$ for each field trip. Different y axes were applied for Nav and BB due to magnitude discrepancies. 44

Figure 3.5. Variability of $a_{NAP}(\lambda)$ in all field trips (a) Nav1, (b) Nav2, (c) Nav3, (d) BB1, (e) BB2 and (f) the average value of $a_{NAP}(\lambda)$ for each field trip. 45

Figure 3.6. Variability of $a_p(\lambda)$ in all field trips. (a) Nav1, (b) Nav2, (c) Nav3, (d) BB1, (e) BB2 and (f) the average value of $a_p(\lambda)$ for each field trip. Different y axles were applied for Nav and BB due to magnitude discrepancies. 46

Figure 3.7. (a) Variation of $a_\phi(\lambda)/a_\phi(443)$ ratio as a function of wavelength considering the average values of BB and Nav and the mass-specific absorption of phytoplankton, $a_\phi{}^*(\lambda)$, for all field campaigns (b) Nav1, (c) Nav2, (d) Nav3, (e) BB1 and (f) BB2. 49

Figure 3.8. (a) Variation of $a_{NAP}(\lambda)/a_{NAP}(443)$ ratio as a function of wavelength considering the averages values of BB and Nav and (b) the relationship between $S_{NAP}$and OSS (mg l^{-1}) from BB. 51

Figure 4.1. Reciprocal remote sensing reflectance (R_{rs}^{-1}) data from the (a) first, (b) second and (c) third field trips. Pure water absorption (a_w) (red line) is shown for reference. 63

Figure 4.2. Ternary plots displaying the relative contribution of CDOM, phytoplankton and detritus to the total absorption at different wavelengths, (a) 443 nm, (b) 560 nm, (c) 665 nm and (d) the relative contribution of water, particulate and CDOM to absorption at 709 nm. 64

Figure 4.3. Relationship between estimated and measured $at(\lambda)$ using existing QAAs: (a) QAA_{Lv5}, (b) QAA_{Lv6} and (c) QAA_{M14}. The colored circles represents the band centers of OLCI sensor. 66

Figure 4.4. Scatter plot between measured and estimated (a) $a_t(\lambda)$, (b) $a_{CDM}(\lambda)$ and (c) $a_\phi(\lambda)$ at OLCI spectral bands. 68

Figure 4.5. Taylor diagrams for $a_t(\lambda)$ at (a) 443 nm, (c) 560 nm, (e) 665 nm. Target diagrams for $a_t(\lambda)$ at (b) 443 nm, (d) 560 nm and (f) 665 nm. Color symbols indicate the following: QAA_{Lv5} (grey dot), QAA_{Lv6} (yellow dot), QAA_{M14} (blue dot) and the QAA_{OMR} (green dot), reference observation (red dot). The black circle in the Target diagrams (M_0) corresponds to a normalized total RMSD of 1.0, so all points between this circle and the origin are positively correlated. 70

Figure 4.6. Taylor diagrams for $a_{CDM}(\lambda)$ at (a) 443 nm, (c) 560 nm, (e) 665 nm. Target diagrams for $a_{CDM}(\lambda)$ at (b) 443 nm, (d) 560 nm and (f) 665 nm. Symbols indicate the following: QAA_{Lv5} (grey dot), QAA_{Lv6} (yellow dot), QAA_{M14} (blue dot) and the QAA_{OMR} (green dot), reference observation (red dot). The black circle in the Target diagrams (M_0) corresponds to a normalized total RMSD of 1.0. 73

Figure 4.7. Taylor diagrams for $a_\phi(\lambda)$ at (a) 443 nm, (c) 560 nm, (e) 665 nm. Target diagrams also for $a_\phi(\lambda)$ at (b) 443 nm, (d) 560 nm and (f) 665 nm. Symbols indicate the following: QAA_{Lv5} (grey dot), QAA_{Lv6} (yellow dot), QAA_{M14} (blue dot) and the QAA_{OMR} (green dot), reference observation (red dot). 76

Figure 4.8. Validation result showing the scatter plot between measured and estimated (a) $a_t(\lambda)$, (b) $a_{CDM}(\lambda)$, (c) $a_\phi(\lambda)$ and the comparison of spectral shape of average measured and estimated (d) $a_t(\lambda)$, (e) $a_{CDM}(\lambda)$ and (f) $a_\phi(\lambda)$. 77

Figure 4.9. Graphic depicting the (a) rainfall, (b) runoff, (c) water level and (d) discharge variability along the period between October 2013 and August 2016. The green diamonds represent $a_t(443)$ retrieved based on QAA_{OMR} from the three field trips carried out in Nav during April/2014, September/2014 and May/2016. Rainfall data was acquired in NASA's GIOVANNI database based on TRMM data with 0.25° of spatial resolution (http://giovanni.sci.gsfc.nasa.gov/giovanni/). Runoff data was also acquired through NASA's GIOVANNI database. Water level as well as discharge were downloaded from the Water National Agency of Brazil through the website (http://sar.ana.gov.br/).. 80

Figure 4.10. Relationship between optical properties and water quality parameters: (a) $a_t(443)$ versus TSS; (b) $a_{CDM}(443)$ versus TSS; (c) $a_\phi(443)$ versus TSS; (d) $a_t(443)$ versus Chl-*a*; (e) $a_{CDM}(443)$ versus Chl-*a* and (f) $a_\phi(443)$ versus Chl-*a*. 82

Figure 5.1. Scatter plots in log-scale between measured and estimated $a_t(\lambda)$, $a_{CDM}(\lambda)$ and $a_\phi(\lambda)$ at OLCI spectral bands. 89

Figure 5.2. Spectral shape acquired through (a) QAA_{BBHR} and (b) Nav in situ a_ϕ acquired from laboratory analysis. The continuous red line stands for the average spectral a_ϕ from Nav in situ data. 90

Figure 5.3. Scatter plots in log-scale between measured and estimated $a_t(\lambda)$, $a_{CDM}(\lambda)$ and $a_\phi(\lambda)$ at OLCI spectral bands. 91

Figure 5.4. Spectral shape acquired through (a) QAA_{OMR} and (b) in situ $a\phi$ from BB acquired from laboratory analysis. The continuous red line stands for the average spectral $a\phi$ from BB in situ data. 93

Figure 6.1. Schematic diagram showing the (a) viewing angle (θ_v) of the sensors to avoid specular scattering (Mobley, 1999) (b) Geometry of the sensor relative to the sun used for radiometric

measurements, represented by zenith (θ_s), azimuthal (ϕ) and nadir (n) angles, (c) sensors collecting total upwelling radiance $L_t(\lambda)$, the incident sky radiance $L_s(\lambda)$ and the downwelling irradiance $E_d(\lambda)$, (d) sensors collecting upwelling radiance $L_u(\lambda)$, upwelling irradiance $E_u(\lambda)$ and the downwelling irradiance $E_d(\lambda)$. 99

Figure 6.2. Cumulative percentage of TSM concentration and the respective frequency of the calibration dataset from BB (a) and Nav (b) reservoirs. 104

Figure 6.3. Relationship between TSM (mg l^{-1}) and Chl-a (mg m^{-3}) in (a) BB and (b) Nav. 106

Figure 6.4. Ternary graphs depicting the absorption budget at three wavelengths in the visible region (a) blue – 443 nm, (b) green – 555 nm and (c) red – 645 nm. 107

Figure 6.5. $R_{rs}(\lambda)_{field}$ spectra representing different TSM concentrations overlapped with MODIS Terra spectral response function for bands at (A) 469 nm, (B) 555 nm and (D) 645 nm. 108

Figure 6.6. Correlation between the original 500 m MODIS B3 and the downscaled 250 m MODIS B3 for (a) May and (b) October, 2014. 109

Figure 6.7. Spatio-temporal distribution of TSM over the main body of Nav based on MODIS 8-day composite images for months of May and October from 2000 to 2015. 114

Figure 6.8. Spatio-temporal distribution of TSM over the main body of BB based on MODIS 8-day composite images for the months of May and October from 2000 to 2015. The blank region represent the locations where the model extrapolated the TSM values over 150 m l^{-1} 115

Figure 6.9. TSM variability during the (a) beginning of the dry season and (b) end of the dry season in Nav; (c) beginning of the dry season and (d) end of the dry season in BB at different locations along the reservoir. SBS: Santa Barbara Stream, BR: Bonito River, PR: Piracicaba River, TR: Tietê River, TZ1: Tranzition Zone 1, TZ2: Transition Zone 2. (e) TSM (mg l^{-1}) concentration from field campaigns carried out in Tietê River (Barra Bonita – BB, Bariri – B, Ibitinga – I, Promissão – P, Nova Avanhandava – Nav) except for Três Irmãos (TI) reservoir in 2000 (CAVENAGHI et al., 2003) (solid lines); including all reservoirs along the Tietê River during the years 2001 and 2002 (ZANATA, 2005) (dotted lines) and in the lower Tietê basin during 2008 and 2009 (dashed lines) (SANTOS, 2010). 118

LIST OF TABLES

Table 3.1. Descriptive statistics of water quality and optical parameters. The notations Min-Max, Aver, SD, CV and n stand for minimum-maximum, average, standard deviation, coefficient of determination and number of samples. 39

Table 4.1. QAA steps comparing the version 5 from Lee et al. (2002) and the QAA_{OMR} proposed in this study. 58

Table 4.2. Descriptive statistic of the water quality variables used for calibration and validation. SD: standard deviation, CV: coefficient of variation and n is the number of samples. 61

Table 4.3. Comparative band-specific errors related to the re-parametrization of $a_t(\lambda)$ based on MAPE (%) and RSMD (m^{-1}) metrics. 68

Table 4.4. Comparative band-specific errors related to the re-parameterization of $a_{CDM}(\lambda)$ based on MAPE (%) and RSMD (m^{-1}) metrics. 72

Table 4.5. Comparative band-specific errors related to the re-parametrization of $a_\phi(\lambda)$ based on MAPE (%) and RSMD (m^{-1}) metrics. 75

Table 5.1 QAA steps comparing the QAA_{BBHR} from Watanabe et al. (2016) and the QAA_{OMR} proposed in the last chapter. 87

Table 5.2. Comparative band-specific errors related to the IOPs retrieved by QAA_{BBHR} based on MAPE (%), RSMD (m^{-1}) and bias (m^{-1}) metrics. 89

Table 5.3. Comparative band-specific errors related to the IOPs retrieved by QAA_{OMR} based on MAPE (%), RSMD (m^{-1}) and bias (m^{-1}) metrics. 92

Table 6.1. TSM empirical models: model fit, TSM concentration range (mg l^{-1}), and geographic location. 102

Table 6.2. Descriptive statistics of environmental dataset in both reservoirs. 105

Table 6.3. Calibration results of the models using the single and two band indexes. Models with R^2 below 0.50 were not displayed here. 110

LIST OF ABBREVIATIONS AND ACRONYMS

ρTOA	Reflectance at the top of atmosphere
ζ	$a_\phi(412)/a_\phi(443)$
ξ	$a_{CDM}(412)/a_{CDM}(443)$
η	Spectral power for backscattering coefficient
λ_0	Reference wavelength
$\delta^{13}C$	Delta thirteen carbon
σ*	Normalized standard deviation
a_p	Total particulate absorption coefficient
a *or* a_t	Total absorption coefficient
a_w	Absorption coefficient of pure water
a_{NAP}	Absorption coefficient of non-algal particle
a_d	Absorption coefficient of detritus
a_{CDOM}	Absorption coefficient of colored dissolved organic matter
a_{CDM}	Absorption coefficient of CDOM and detritus
a_ϕ	Absorption coefficient of phytoplankton
a_{t-w}	Total absorption budget without the water fraction
a_ϕ^*	Specific absorption coefficient of phytoplankton
a_ϕ^+	Normalized spectral absorption of phytoplankton
b_b	Backscattering coefficient
b_{bp}	Particulate backscattering coefficient
b_{bw}	Pure water backscattering coefficient
B*	Normalized bias
CDOM	Colored dissolved organic matter
Chl-*a*	Chlorophyll-*a*
E_u	Upwelling irradiance
E_d	Downwelling irradiance
IOP	Inherent optical properties
ISS	Inorganic suspended solids
L_u	Upwelling radiance
$E_d(0^+)$	Downwelling irradiance incident onto the water surface
L_{sky}	Incident sky radiance
L_t	Total upwelling radiance
LULC	Land use and land cover
l	Path length
MAPE	Mean absolute percentage error
MODIS	Moderate Resolution Imaging Spectroradiometer
NAP	Non-algal particle
NDWI	Normalized Difference Water Index
OSC	Optically significant components
OLCI	Ocean and Land Colour Instrument
OSS	Organic suspended solids
OD	Optical density
OD_{sample}	Optical density of the sample
$OD_{reference}$	Optical density of the reference
QAA	Quasi-analytical algorithm
R	Irradiance reflectance

R_{rs}	Remote sensing reflectance
r_{rs}	Subsurface remote sensing reflectance
$R_{rs_{sat}}$	Water surface remote sensing reflectance
$R_{rs_{sim}}$	Simulated bands from MODIS/Terra
$R_{rs_{field}}$	*In situ* remote sensing reflectance
R_{rs}^{-1}	Reciprocal remote sensing reflectance
RMSD	Total root mean square difference
RMSE	Total root mean square error
S_{CDM}	Spectral slope of colored detrital matter absorption coefficient
S_{CDOM}	Spectral slope of colored dissolved organic matter
S_{NAP}	Spectral slope of non-algal particle
SIOP	Mass-specific inherent optical properties
SRF	Spectral response function
TSS	Total suspended sediment or solids
TSM	Total suspended matter
u	Ratio of backscattering coefficient to the sum of backscattering and absorption coefficients
*u*RMSD*	Normalized unbiased RMSD

CONTENTS

CHAPTER 1: INTRODUCTION 19
1.1 Background 19
1.2 Motivation 20
1.3 Hypothesis 22
1.4 Objectives 23
1.5 Outline of the Thesis 23
CHAPTER 2: STUDY AREA AND FIELD CAMPAIGNS 24
2.1 General characteristics 24
2.2 Strategy for sampling design 26
2.3 Field campaigns 29
2.4 Field data acquisition 32
CHAPTER 3: ABSORPTION PROPERTIES OF TWO OPTICALLY DIFFERENT RESERVOIRS SITUATED ALONG THE CASCADE SYSTEM OF TIETÊ RIVER 34
3.1 Introduction 34
3.2 Data and Methods 36
3.2.1 Water quality parameters 36
3.2.2 Inherent optical properties 37
3.3 Results 38
3.3.1 General characteristics of water quality parameters and optical properties 38
3.3.2 Absorption coefficient budget 41
3.3.3 CDOM absorption 42
3.3.4 Phytoplankton absorption 43
3.3.5 NAP absorption 44
3.3.6 Particle absorption 45
3.4. Discussion 46
3.5 Conclusion 51
CHAPTER 4: RETRIEVAL OF INHERENT OPTICAL PROPERTIES FROM OLIGO-TO-MESOTROPHIC INLAND WATER USING THE QUASI-ANALYTICAL ALGORITHM 53
4.1 Introduction 53
4.2 Data and methods 55
4.2.1 Water quality parameters 55
4.2.2 *In-Situ* Radiometric Data 56
4.2.3 *In Situ* Inherent Optical Properties 57

4.2.4 QAA General Context 58
4.2.5 Re-parametrization /Validation and Accuracy Assessment 59
4.3 Results and Discussion 61
4.3.1 Biogeochemical characterization 61
4.3.2 Bio-optical characterization 62
4.3.3 OSC relative contribution 63
4.3.4 Performance of existing QAA 65
4.3.5 Re-parametrization of QAA to derive a_t 66
4.3.6 Re-parametrization of QAA to derive a_{CDM} 70
4.3.7 Re-parametrization of QAA to derive a_ϕ 73
4.3.8 Model Validation 76
4.3.9 Linking IOPs variability to physical and meteorological variation 78
4.3.10 Factors influencing optical changes in the reservoir 81
4.3.11 Implications of QAA_{OMR} for water resource management 83
4.4 Conclusion 83
CHAPTER 5: EVALUATION OF QAA_{OMR} AND QAA_{BBHR} PERFORMANCES IN DERIVING THE IOPS IN BOTH BB AND NAV RESERVOIRS 85
5.1 Introduction 85
5.2 Data and Methods 86
5.3 Results and Discussion 88
5.3.1 Use of QAA_{BBHR} in Nav's dataset 88
5.4.2 Use of QAA_{OMR} in BB's dataset 91
5.4. Conclusion 93
CHAPTER 6: LONG-TERM MONITORING OF TOTAL SUSPENDED MATTER IN TROPICAL RESERVOIRS WITHIN A CASCADE SYSTEM WITH WIDELY DIFFERING OPTICAL PROPERTIES 95
6.1 Introduction 95
6.2 Data and Methods 98
6.2.1 Field data 98
6.2.2 Remote sensing reflectance (R_{rs}) 98
6.2.3 Inherent Optical Properties (IOPs) 100
6.2.4 Satellite Data and Processing 101
6.2.5 Bio-optical model calibration and validation 102
6.3 Results 103
6.3.1 Long-term spatio-temporal monitoring 104
6.3.2 Water quality characterization 104

6.3.3 Bio-optical properties description 106
6.3.4 Downscaling MODIS image procedure 108
6.3.5 TSM algorithm calibration and validation 109
6.3.6 TSM spatio-temporal variability 113
6.3.7 Factors affecting optical changes in the reservoirs 119
6.4 Conclusion 120
CHAPTER 7: CONCLUSION AND FUTURE RECOMMENDATIONS 122
7.1 Conclusion 122
7.2 Future Recommendations 124
REFERENCES 126

CHAPTER 1: INTRODUCTION

1.1 Background

The reservoirs of the Tietê River placed in the State of São Paulo, are exposed by a series of pollution sources such as sugar cane plantation, pastures and urban centers from which a large amount of pollutants reaches the aquatic system. On the one hand, the construction of these reservoirs supports the agriculture and industrial development of the region; on the other hand, it generates a series of negative impacts including intensive deforestation, eutrophication due to high loads of nutrients and suspended sediment from various activities, sedimentation and contamination of water bodies (BARBOSA et al. 1999).

According to Fracácio et al. (2002), all the reservoirs of the Tietê River were classified as eutrophic for the parameter chlorophyll-a (Chl-*a*); for total phosphorus (TP), the reservoirs of Barra Bonita (BB), Bariri (B) and Ibitinga (Ib) were considered mesotrophic; and the Promissão (Pr) and Nova Avanhandava (Nav), oligotrophic. Differences in the mass of water composition between BB e Nav were reported and the first reservoir was attested to be more polluted than Nav. BB also has the highest concentration of suspended solids, thus higher turbidity when compared to Nav (CAVENAGHI et al. 2003). These results clearly show the existence of a trophic gradient between the cascade reservoirs.

Although some studies have shown that the cascade reservoirs have a trophic and spectral gradient (WACHHOLZ et al., 2009; PEREIRA FILHO et al. 2009), just recently studies have investigated the cascade system effects on optical properties (ALCÂNTARA et al., 2016, RODRIGUES et al., 2016a). In terms of water resource management, the traditional methods for water monitoring are time consuming, expensive and demands *in situ* collection. Besides, these techniques present low spatial and temporal representativeness, therefore, the optical properties of the in-water constituents (Chl-*a*, non-algal-particle – NAP, total suspended sediment – TSS, colored dissolved organic matter – CDOM) and here known as optical significant components (OSCs), can be used in bio-optical models in order to estimate the concentrations of the OSCs and support the water resource management considering large areas and short time mapping.

1.2 Motivation

Environments such as reservoirs designed in cascade system cause water quality modifications from the upstream to downstream reducing the turbidity and increasing the transparency of water (BARBOSA et al. 1999). The longitudinal variability is not the only factor influencing the water quality dynamic, but the watershed controls several mechanisms of reservoirs functioning. Watersheds subjected to extensive use by human activities can produce high loads of nutrients, suspended matter or even toxic substances to the reservoir (JORGENSEN et al., 2012).

Built to attend single or more specific purpose, the reservoirs have multiple uses and therefore, demands for complex strategies of management. The desired phases for management systems include the integration of geographic information system and remote sensing in order to provide a rapid or a large-scale comprehension of reservoirs (TUNDISI and MATSUMURA-TUNDISI, 2011). Remote sensing is also important for offering spatial and temporal views of water quality surface parameters, which is limited from in situ collections. Its applicability becomes useful when the water degradation is caused by OSC, such as the green algae pigments as Chl-*a*, TSS, CDOM and NAP, thus producing detectable effects by optical remote sensing instruments (GIARDINO et al., 2010).

The spectral region where these components can be detected is limited to a narrow range of optical wavelengths, in general, restricted between 400 to 850 nm (DEKKER, 1993). In inland waters, NAP and CDOM absorb at shorter wavelengths showing an exponential decay toward longer wavelengths, while Chl-*a* presents absorption peaks in the blue and red wavelengths (ROESLER et al., 1989; BRICAUD et al., 1981). However, in waters with low phytoplankton concentration the absorption peak at the blue region is not detected (WU et al., 2011), nevertheless, significant contributions of Chl-*a* lead to the enhancement of the absorption peak at ~675 nm allowing its detection on the remote sensing reflectance (R_{rs}) signal in very productive inland waters (DOXARAN et al., 2006).

Waters dominated by sediment, especially NAP and pure water showed satisfactory results with the empirical relationships $R_{rs}(850)/R_{rs}(550)$ and $R_{rs}(850)/R_{rs}(650)$ for TSS retrieval in Gironde estuary (DOXARAN et al., 2006). In waters comprised by mineral suspended sediment (MSS), the red-to-green ratio showed to be applicable, however, with increasing influence of phytoplankton and CDOM this relationship was found to break down, assuming the limited potential of the model (BINDING et al., 2003). In the case of CDOM absorption estimation, D'Sa and Miller (2003) showed that the ratio between two visible bands

$R_{rs}(510)/R_{rs}(555)$ was suitable for the turbid waters of Mississippi River, while Doxaran et al. (2006) found the ratio $R_{rs}(400)/R_{rs}(700)$ more appropriate for Tamar estuary. For Chl-*a* retrieval, Dall'Olmo et al. (2003, 2005) showed that a three-band model based on NIR-Red wavelengths produce more accurate values in turbid waters, however, they also noticed that both Chl-*a* fluorescence and Chl-*a* mass-specific absorption coefficient (a^*_{Chla}) variability can introduce more uncertainties in the estimative.

In other words, the knowledge about the optical water properties can improve the formulation of models for OSC concentration retrieval, however, algorithms based on empirical assumptions often fail when applied to other study sites (RITCHIE et al., 2003). Besides, these models are also limited for a specific range of OSC concentration. Kumar et al. (2016) for example, found a simple correlation between MODIS $R_{rs}(645\ nm)$ and TSS concentration in Chilika Lagoon, India. Their model showed to be limited to the range between 6.5 and 200 mg l^{-1}, with increasing error in very low TSS (< 6.54 mg l^{-1}). Ogashawara et al. (2013) evaluated the influence of Chl-*a* absorption on the performance of several empirical algorithms using data from environments with very low and very high cyanobacteria. As result, they verified a decrease of model's sensitivity in high phycocyanin concentration environments. Chen et al. (2015) studied a wide range of TSS (58 – 577.2 mg l^{-1}) in estuary and coastal waters using an improved model based on the log-ratio ($R_{rs}(NIR)/R_{rs}(Red)$), however, they had to consider a constraint based on TSS concentration below and above 31 mg l^{-1}.

In general, the empirical methods work well for turbid inland waters, however, in oligotrophic environments the performance decrease considerably using the same band combination. Gons et al. (2008) for example, showed that a red-to-NIR band Ch-*a* algorithm proved to be applicable for eutrophic to hypereutrophic waters, however the accuracy dropped considerably for oligotrophic waters. They also reported that remote sensing of Chl-*a* is limited in low concentration range and not the contrary. The alternative for low concentrations would be to use the blue-to-green band ratio (GONS and AUER, 2004; GONS et al., 2008).

Aiming to address the empirical issue, semi-analytical approaches use the IOP and apparent optical properties (AOP) to model the reflectance and vice versa. These properties are then used in analytical methods to retrieve the water constituents. The main limitation regards the insufficient knowledge about the IOPs used in the equations (MOREL and GORDON, 1980; DEKKER, 1993). The example of a more robust model is the quasi-analytical algorithm (QAA) developed to derive the absorption and backscattering coefficients in open ocean and coastal waters (LEE et al., 2002). After that, several initiatives were carried out aiming to fit this model

to productive inland waters (LE et al., 2009a; YANG et al., 2013, MISHRA et al., 2014; WATANABE et al., 2016a). A version based on CDOM dominated waters was also developed (OGASHAWARA et al., 2016), however, a model adapted to inorganic matter dominated water was not addresses yet. A semi-analytical algorithm using the QAA was successfully applied for retrieving the water clarity based on new theoretical model to interpret the Secchi disk depth, Z_{SD} (LEE et al., 2015). For validation, the authors used data covering oceanic, coastal and inland waters (lake) and as result they got an average absolute difference of ~18%, highlighting the accomplishment of a model using a wide range of data.

As previously mentioned, the comprehension about the bio-optical properties of different environments helps to indicate the suitable approach for water quality parameters estimation. Many efforts have shown the success of empirical approaches in deriving the water optical properties in very turbid inland waters, however, when data from two widely trophic state (oligo to eutrophic) reservoirs is supposed to be mixed, we expect the models to perform poorly, indicating the limitation of a single approach in retrieving the OSCs. Up to now, incipient initiatives showed the influence of cascade system in the optical properties, which means that a lot of efforts still need to be done.

1.3 Hypothesis

In a cascading arrangement where the water flows with different composition through the system, the bio-optical modeling can be challenging. As we learned from the literature such systems range from hyper-to-oligotrophic, from organic-to-inorganic dominated waters, and consequently the development of an algorithm to map the water optical properties needs to deal with such contrast. Moreover, the literature showed that empirical models are constrained by the local optical properties and the range of OSC concentration, while semi-analytical approaches tend to fail where the phytoplankton is not the dominant component and where some empirical steps are calibrated using synthetic data. Thus, our hypothesis bases on the fact that due to the organic and inorganic nature of both BB and Nav reservoirs, the empirical approach won't be able to map the OSC accurately using a single model, however, recalibrating the empirical steps using in situ data, the quasi-analytical algorithm will increase the retrieval of water optical properties and therefore will be able to map operationally the water quality from remotely sensed images in a cascade system.

1.4 Objectives

According to the thesis hypothesis, we aimed to investigate the water optical properties of both BB and Nav in order to evaluate the performance of a single model built for retrieving the inherent optical properties as well as total suspended sediment concentration of both reservoirs. For this, specific objectives were designed:

- Characterize the absorption properties in both BB and Nav reservoirs;
- Re-parameterize the QAA algorithm based on OLCI/Sentinel-3 bands using *in situ* data from Nav; validate the algorithm using an independent dataset collected from the same area in a different season;
- Assess the performance of a single QAA version (QAA_{BBHR} from Watanabe et al. 2016 and QAA_{OMR} proposed here) highlighting the improvements and fragilities from each version supposing to choose a single approach for mapping the absorption properties in the entire cascade;
- Assess the performance of empirical models for retrieving TSS concentration in both BB and Nav using single or separate models.

1.5 Outline of the Thesis

This thesis is organized in 7 chapters. Chapter 1 introduces the theme, highlighting the problem of the research followed by the questions we intend to answer and the objectives we expect to achieve. Chapter 2 describes the study areas focusing on their physical and environmental characteristics; description of the method designed to sampling definition and the field trips. Chapter 3 describes the IOPs of both reservoirs and their relationships with optical water parameters. In Chapter 4, a parametrization of QAA_{OMR} was carried out using data from Nav and validate it with an independent dataset collected in a different season. Chapter 5 compares and evaluates the performance of both QAA_{OMR} and QAA_{BBHR} in retrieving the IOPs using data from BB and Nav, respectively. In Chapter 6 empirical models were formulated aiming to retrieve TSS in both reservoirs. Lastly, Chapter 7 pointed out the main findings of the research and it makes some recommendations for future works.

CHAPTER 2: STUDY AREA AND FIELD CAMPAIGNS

2.1 General characteristics

The reservoirs of Barra Bonita (BB) and Nova Avanhandava (Nav) (Figure 2.1) are situated in the middle and lower portion of the Tietê River, São Paulo State, respectively. BB (22°31′10″S, 48°32′3″W) is a storage system and began its operation in 1963 flooding an area of 310 km^2, with a dam length of 480 m, 90.3 days of residence time, being formed from the damming of Tietê and Piracicaba Rivers. The regional climate transits between tropical and subtropical, and the annual seasons are not well marked. According to the Koppen classification, the climate is mesothermal type - CWA, with a dry winter and a hot summer (PRADO, 2004). Pastures and sugar cane monoculture predominantly comprised the land cover.

Figure 2.1. Graphic representation of the study area emphasizing (a) Brazil's territory, (b) Tietê River located at São Paulo State and the location of the reservoirs from upstream to downstream: Barra Bonita, Bariri, Ibitinga, Promissão, Nova Avanhandava and Três Irmãos, (c) sampling location of Nav and (d) BB.

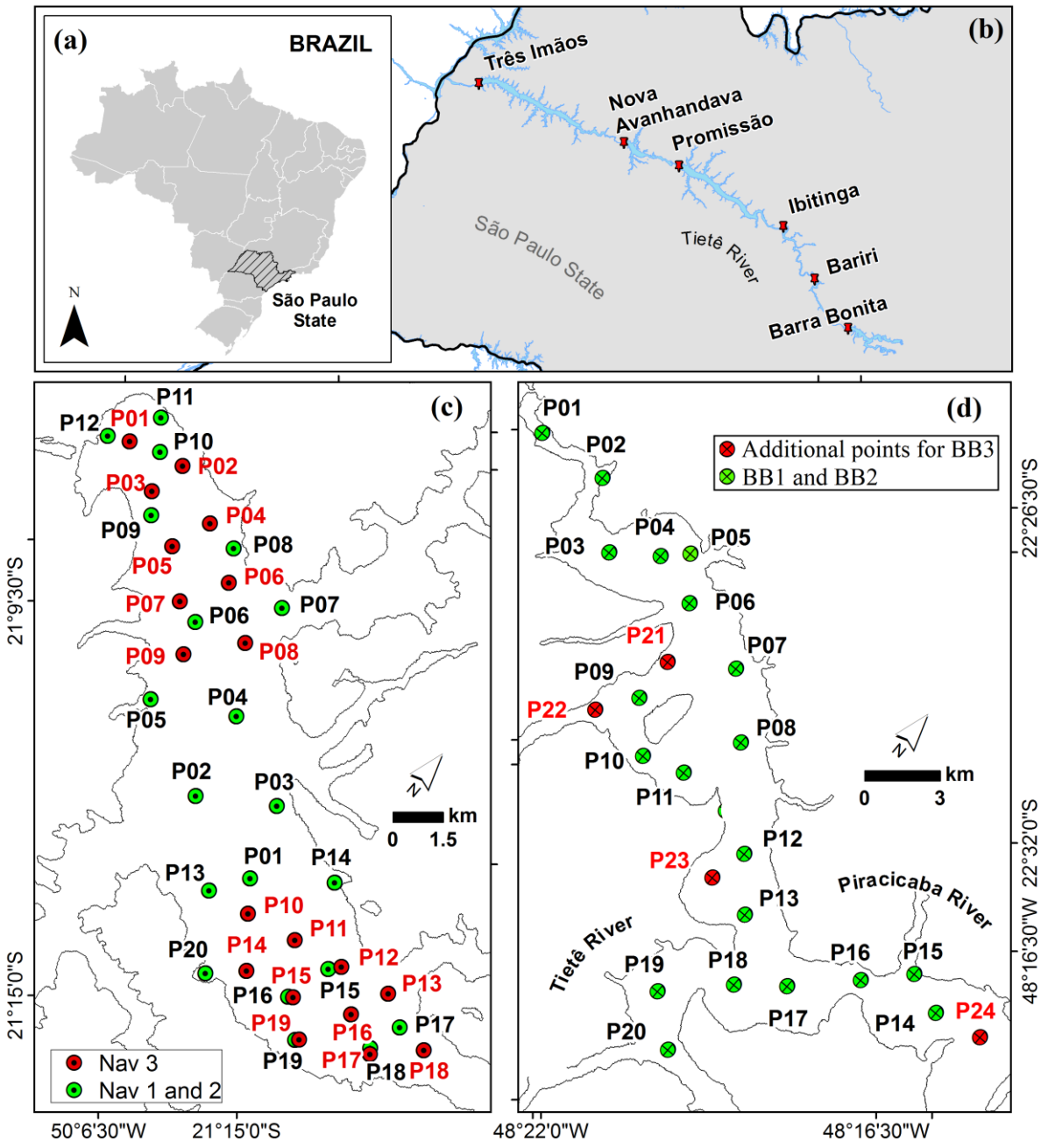

On the other hand, Nav (21°7′1″S, 50°12′6″W) is a run-of-river reservoir and was created in 1982, flooding an area of 210 km² (at its maximum quota), with a dam length of 2,038 m and mean residence time of the water around 46 days (TORLONI, et al., 1993). The reservoir is part of a region whose influence of Continental Tropical and Polar Antarctic air masses are marked. The first mass is hot and dry and occurs mainly in the summer (24 and 30°

C), while the second is cold and damp, and, despite being-active all year, its occurrence is more intense in winter, causing a decrease of temperature (22 to 14° C) (CBH-BT, 1999).

BB reservoir is an ecosystem characterized as polymictic and eutrophic, with high loads of nutrients, whose contribution leads to the development of blooms of cyanobacteria during the summer, and Bacillariophyceae during the winter (DELLAMANO-OLIVEIRA et al. 2007). The Piracicaba and Tietê Rivers, which along their courses are subject to the carrying of organic and inorganic origin waste, arising from agricultural, urban and industrial activities, affecting water quality. Nav is an oligo-to-mesotrophic reservoir with the upper layer of the water column well oxygenated and pH ranging from slightly acid to alkaline (6.47 – 8.2), conductivity relatively high (83 – 150 µS cm^{-1}) and low concentrations of nutrients (Total N: 0.05 – 0.23 µg l^{-1} and Total P: 18.02 – 32.33 µg l^{-1}) (RODGHER et al. 2005; SMITH et al. 2014). The high transparency of the water often leads to the growth of submerged macrophytes (e.g. *Egeria sp.* – *Elodea*) (SMITH et al. 2014), although, during sample collections we avoided those areas. The catchment basin surrounding the reservoir receives input from non-point source of pollution such as sugar cane and citric plantation (orange and lemon) and cattle breeding.

There is evidence that the downstream reservoirs of Tietê River have improved water quality to those further upstream providing an enhancement of chemical constitution of water limiting the development of floating vegetation representative of a eutrophic environment (BARBOSA et al., 1999; CAVENAGHI et al. 2003). The cascade system generates significant modifications along the river changing aspects such as heterogeneity, connectivity and the coarse / fine particulate organic material. Moreover, this type of system influences the water quality, the composition and structure of phytoplankton community, and increases the eutrophication process in the upstream reservoirs (BARBOSA et al., 1999).

2.2 Strategy for sampling design

Based on the sampling design, a random stratified sampling method was used to determine the location for collecting water and optical data in BB and Nav (RODRIGUES et al., 2016b). Therefore, statistical and computational procedures were established aiming to provide parameters that subsidize the sampling design definition (Figure 2.2). For this purpose, the Operational Land Imager (OLI)/Landsat-8 imagery referring to an annual cycle was acquired at the USGS – U.S. Geological Survey website <http://earthexplorer.usgs.gov/> and the criterion of less cloud cover and absence of glint effect, visually detected, was applied.

The images hosted at the USGS website are geometrically corrected and available for users in the orthorectified level (L1T) in which the reference data are terrain control points and altitude based on digital elevation model (DEM), such as the SRTM (Shuttle Radar Topography Mission) (USGS, 2014). This procedure assures the overlapping between images with geometric error below one pixel providing the high matching considering different periods. The methodological approach is displayed in Figure 2.2.

Figure 2.2. Flowchart showing the methodological scheme for sampling stations definition. ρTOA represents the value of reflectance at the top of atmosphere (TOA), SD stands for the standard deviation, NDWI is the Normalized Difference Water Index, and PCA is the Principal Component Analysis. The box 1 refers to the multispectral images; box 2 stands for the reservoir's delimitation and box 3, stratified sampling.

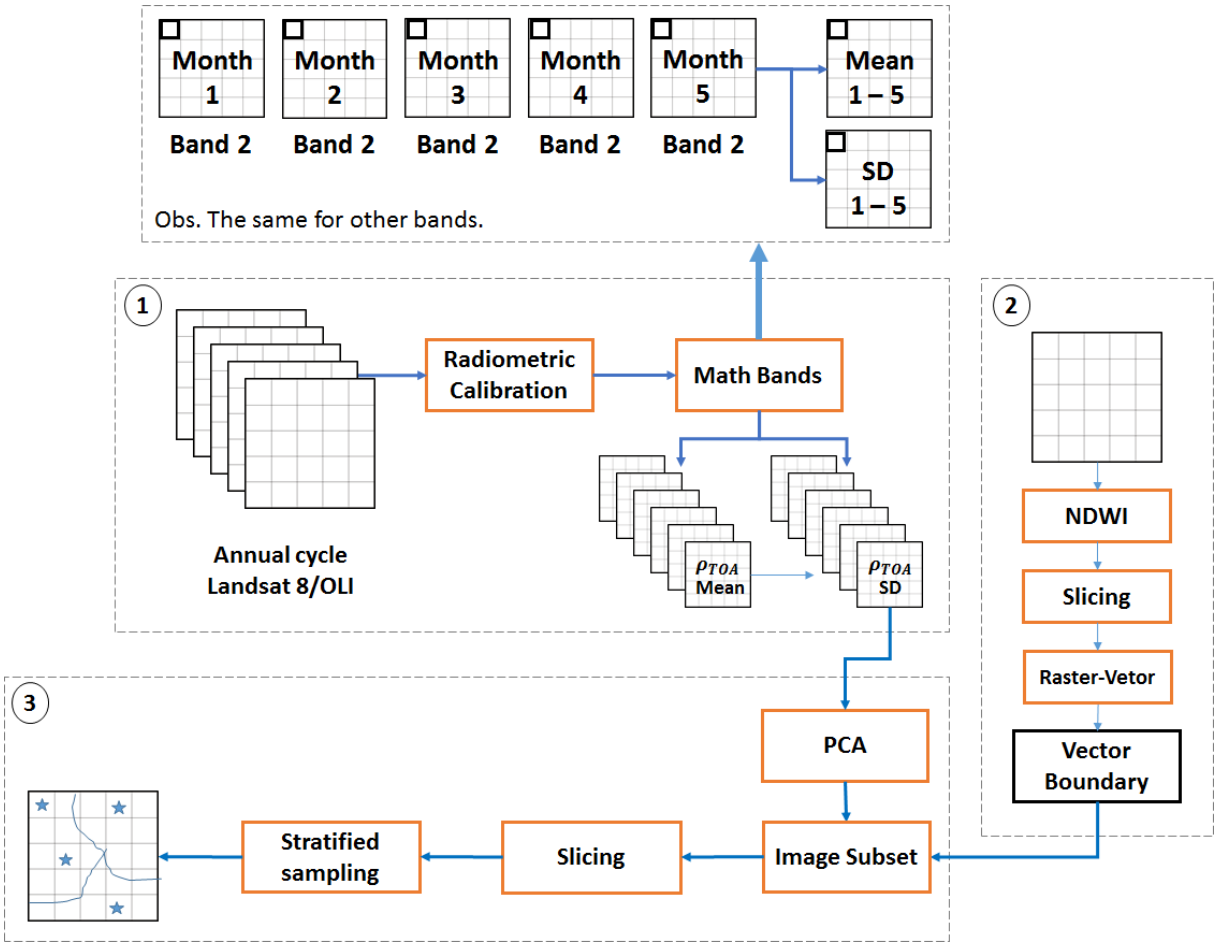

A set of images available for a year was radiometrically calibrated. In this process, the digital numbers (DN) of each pixel are rescaled for radiance or reflectance at the top of the atmosphere (TOA), ρTOA, using gain and offset parameters provided by the metadata of the image (USGS, 2013). This procedure removes the effects caused by the difference of

illumination geometry (COLLETT et al., 1998). Studies carried out in aquatic systems showed that TOA products yielded similar or better results from those atmospherically corrected data (OLMANSON et al., 2011, KUTSER, 2012).

In view of the hydrological dynamics and other anthropic or natural interventions that the reservoirs undergo over time, it is important to consider the variations in the chemical and biological characteristics of the water body, with the input of nutrients from agricultural activities around the reservoir, and still insertion of organic and inorganic substances carried longitudinally along the entire cascade system. Therefore, two statistical metrics were considered to analyze the variations: mean and standard deviation (SD). After the radiometric correction process, a set of images referring to one year (2013 - 2014), each consisting of 6 spectral bands (bands 2 to 7), were submitted to the calculation of the mean and subsequent standard deviation. Bands corresponding to the same wavelength were compressed and then the mean and standard deviation for the studied months were calculated, with each pixel of the final image having the mean value of spectral ρTOA, as well as standard deviation.

For delimitation of the boundary of each reservoir a set of processes were established, such as the selection of a reference image, application of the NDWI, slice, conversion raster-vector e finally, the creation of the mask. The image of reference was based on the season with low rainfall. In this case, the image from July/2013 was chosen. It is worth mentioning that Nav does not present a notable variation in water level due to its operational system, on the contrary, BB varies seasonally. Aiming to separate water from other targets, NDWI from McFeeters (1996) was applied as follows:

$$NDWI = \frac{Grenn - NIR}{Green + NIR} \tag{2.1}$$

where Green and NIR are the bands 3 and 5 from OLI/Landsat-8, respectively. This ratio aims to maximize the water reflectance in the visible spectral region and minimize it in the infrared.

There are modifications of this index, such as the MNDWI proposed by Xu (2006) who used a ratio between the green and middle infrared (MIR) bands aiming to enhanced the features of water in regions which the contamination by other targets are evident like noises related to built-up land, soil and vegetation overestimating the water targets. However, we kept the Equation 2.1, since the method employed here predicts the use of a buffer in order to avoid the borders with other targets but water. The separation of water from the other targets was obtained by slicing between values representative of each target. Thus, pixels with values assigned with

water were allocated in a class while the others in another class, resulting in two classes: water and non-water.

For stratified sampling, the SD images were transformed in Principal Component Analysis (PCA) in a Geographic Information System (GIS) environment and then sliced according to intervals empirically defined. The selected image for this step was based on the component with higher variability from the set of 6 SD bands. The slice step allowed the creation of stratus for further sampling points definition. A buffer with 70 m was created for each reservoir to prevent the edges formed by land. Using the tool Hawth's Tools developed by Hawthorne Beyer (http://www.spatialecology.com/) and compatible to a GIS environment, the random stratified sampling was possible to be carried out. Initially, more than a required number of samples were created in order to remove the non-spatialized stations. The minimal distance of 1 km between samples was established to prevent clusters. As result, 20 samples were acquired for each field campaign except for the third campaign in BB that included 4 samples (totalizing 24 samples) and in Nav 20 samples in different locations were added for the first and second field trips and 19 for the third field trip.

2.3 Field campaigns

The water quality parameters, as well as their spatial distribution are seasonal dependent, therefore, we considered at least two periods of the year for water and optical data collection. The water samples were collected in six field campaigns (Figure 1). For Nav, the field trips occurred during austral autumn (Nav1: 28 April – 2 May/2014 and Nav2: 23 – 26 September/2014) and austral spring (Nav3: 9 and 14 May/2016). For BB, the field trips were carried out in austral autumn (BB1: 5 – 9 May/2014) and austral spring (BB2: 13 – 16 October/2014 and BB3: 13 – 15 September/2015). Both seasons are known for intermediate precipitation amounts between summer (wet period) and winter (dry period). Data collections were avoided in the summer due to high rainfall rates making difficult to obtain cloud free satellite images.

As depicted in Figure 2.3, the rainfall data in BB and Nav showed distinct values. In Nav, for example, the month of January and February from 2011 to 2016 showed the highest averages values of 197.24 and 196.92 mm, respectively. BB, in turn, presented 222.59 and 209.16 mm in January and February, respectively. These values were expected because they occurred in the wet period (summer). The year of 2014 showed the lowest values for the respective months presenting 130.75 and 141.81 mm in Nav and 168.51 and 146.24 mm in BB,

respectively. The lowest average values were observed in July and August corresponding to the dry period (winter). Nav showed in July and August averages of 42.51 and 12.79 mm, respectively, whilst BB presented averages of 72.85 and 46.29 mm. In 2014, the lowest rainfall in Nav were observed in June (24.00 mm) and August (6.80 mm) while in BB, the lowest ones were seen in July (40.26 mm) and August (38.83 mm). The months chosen for the field works varied below and above the mean measures (2011 – 2016), but in the austral summer of 2013/2014, the values were below the average and this happened due to an extreme event of drought classified as exceptionally dry (COELHO et al., 2015). The authors also described the 2014/2015 summer as atypical and dry, however, in lower magnitude as the 2013/2014 summer.

The months of April/May of 2014 represented the period of the first data collection in Nav and the rainfall data showed that in both months the values (98.41 and 69.00 mm, respectively) were below the average between 2011 and 2016 (99.67 and 95.05 mm). The month of September/2014 related to the second field collection presented value (141.40 mm) above the average (86.14 mm) and the same happened to the third field trip (May/2016) which showed a value of 197.49 mm above the average (95.05 mm).

Figure 2.3. Rainfall data from the period between 2011 to 2016 (boxplots) highlighting the years of 2014, 2015 and 2016 for (a) Nav and (b) BB. Nav1 (28 April – 2 May/2014), Nav2 (23 – 26 September/2014) and Nav3 (9 and 14 May/2016).

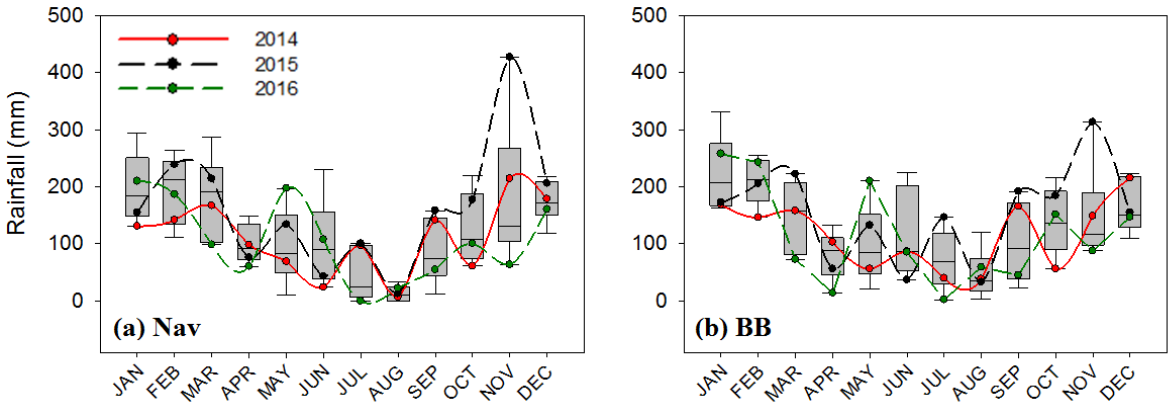

Source: NASA/GIOVANNI (https://giovanni.gsfc.nasa.gov/giovanni/).

The first field trip of BB carried out in May/2014 presented a value of 56.31 mm, below the average of 98.54 mm. The second field trip that occurred in October/2014, also exhibited a value (56.19 mm) below the average (164.14 mm). On the other hand, the third field trip (September/2015) displayed a value (192.08 mm) above the average (101.35 mm). The rainfall variability and the special event of dry in the austral summer (2013/2014) implied in severe

impacts in water availability for public consumption, hydropower generation and agriculture (COELHO et al., 2015).

Data of water level also showed the impact of the dry summer in 2014. A slight variability between 2011 to 2016 was observed in Nav (Figure 2.4), with an average interval of 357.60 ± 0.30 to 357.77 ± 0.32 m from January to December. The year of 2014 displayed the lowest water level except in January that showed a value of 357.56 m. The water level fluctuated between 0.13 m in 2011 to 0.69 m in 2015, in 2014 the amplitude was 0.50 m. Nav is a run-of-river reservoir, therefore, the water level variation with low amplitude is expected (PERBICHE-NEVES et al., 2013).

Figure 2.4. Water level data from the period between 2011 to 2016 (boxplots) highlighting the years of 2014, 2015 and 2016 for (a) Nav and (b) BB. Different axis y was used due to distinct magnitudes. Nav1 (28 April – 2 May/2014), Nav2 (23 – 26 September/2014) and Nav3 (9 and 14 May/2016).

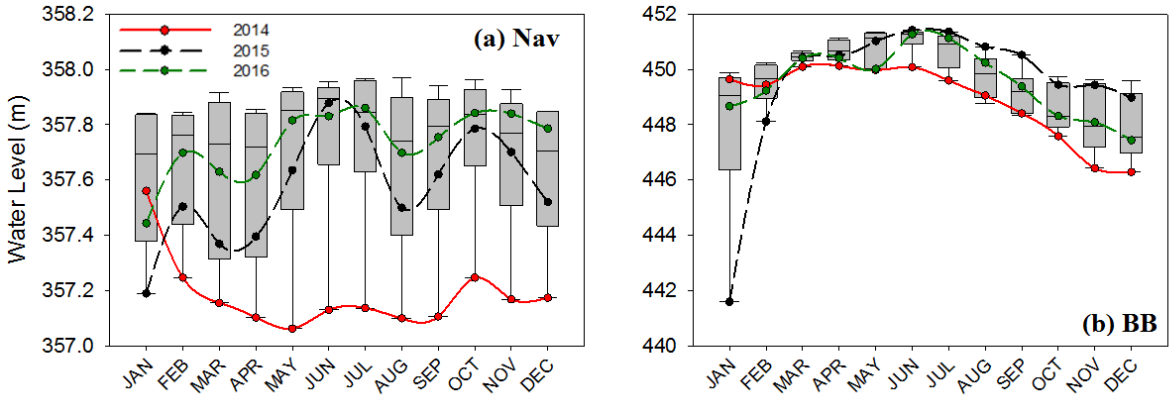

Source: National Water Agency – ANA (http://sar.ana.gov.br/MedicaoSIN)

The water level in BB (Figure 2.4b) varied from an average of 447.85 ± 1.21 m in December and 451.10 ± 0.51 m in June. The year of 2014 was also the one with water level excepted for the months of January and February that was lower in 2015. The amplitude ranged between 2.11 m in 2013 to 9.84 m in 2015. 2014 presented an amplitude of 3.85 along the year. The storage or accumulation reservoir of BB generates a higher variation in water level than the run-of-river system (PERBICHE-NEVES et al., 2013).

The water flow (Figure 2.5) also showed to vary as a function of the dry event in 2014, showing the lowest values in almost the entire year, except for January of 2015. Regarding the magnitude, Nav and BB presented significant differences, the variability in Nav, for instance, ranged from 232.09 m^3/s in October to 683.34 m^3/s in December, while in BB, the range was

between 113.00 m^3/s in October and 361.50 m^3/s in December. The water flow was considerably reduced in BB aiming to keep the water retained in the system during the dry events, on the other hand, in Nav, the regulation of water flow, theoretically, is not necessary due to the absence of storage area, so the water flows naturally according to the river regime (EGRÉ and MILEWSKI, 2002). In addition, the regulation of Nav showed to be influenced by BB because of the variation in phase observed at Figure 2.5, highlighting the co-oscillation between them.

Figure 2.5. Water flow data from the period between 2011 to 2016 (boxplots) highlighting the years of 2014, 2015 and 2016 for (a) Nav and (b) BB. Nav1 (28 April – 2 May/2014), Nav2 (23 – 26 September/2014) and Nav3 (9 and 14 May/2016).

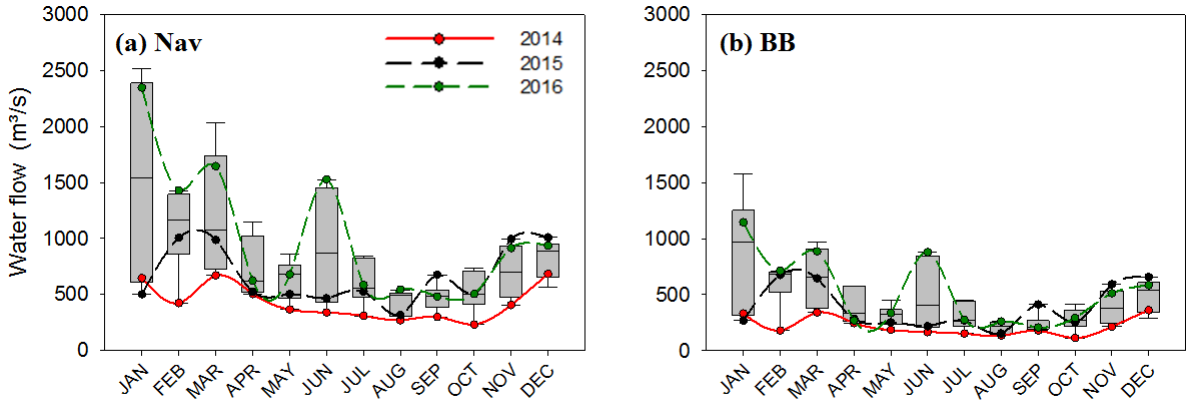

Source: National Water Agency – ANA (http://sar.ana.gov.br/MedicaoSIN)

2.4 Field data acquisition

For this study both water quality and optical data were acquired for each sampling station. The amount of water collected for BB and Nav was established according to the total particulate matter capable to be filter without saturate it. Therefore, a total of 5L of water was collected for both reservoirs, however, for each TSS and Chl-*a* concentrations 250 – 500 mL were filtered considering one filter/replica in BB and 750 – 1000 mL were used for Nav. The water samples were stored in polyethylene containers and refrigerated for laboratory analysis. Water transparency was measured by a Secchi disk (30 cm diameter), turbidity by a portable turbidimeter, model Hanna HI 93414, and dissolved oxygen by a portable meter, model Hanna HI 9146-04.

The *in situ* spectroradiometric measurements are very important for bio-optical characterization and information extraction from remote sensing data, as they act as a bridge

between optical measurements in laboratory and measures taken at the orbital or airborne level. This kind of measure permits the elimination of some undesirable effects such as atmospheric influence and the scale effect. Thus, radiometric measurements were carried out through RAMSES-ARC (radiance sensors) and RAMSES-ACC (irradiance sensors) spectroradiometers. The RAMSES instruments provide simultaneous measurements of upwelling (E_u) and downwelling (E_d) irradiance and upwelling radiance (L_u) of the water column as well as measurements of downwelling irradiance incident onto the water surface ($E_d(0^+)$), incident sky radiance (L_{sky}) and total upwelling radiance (L_t) above the surface of the water.

The determination of the total particulate absorption coefficient (a_p = NAP + phytoplankton) was accomplished by the use of an integrating sphere module present in the double-beam Shimadzu UV-2600 UV-Vis spectrophotometer, with spectral sampling from 280 nm to 800 nm and spectral sampling of 1 nm. The pure water absorption coefficient is a constant obtained by Pope and Fry (1997).

CHAPTER 3: ABSORPTION PROPERTIES OF TWO OPTICALLY DIFFERENT RESERVOIRS SITUATED ALONG THE CASCADE SYSTEM OF TIETÊ RIVER

3.1 Introduction

Optical properties of water are the basis of watercolor retrieval algorithms. Variations of these properties can change the model parameters, optimal spectral bands and the accuracy of retrieval algorithms. In order to improve the performance of bio-optical models (semi-analytical approaches), a better understanding about the variability in the absorption (*a*, units in m^{-1}) and backscattering (b_b, units in m^{-1}) coefficients is crucial. These coefficients influence the magnitude and the spectral distribution of the water-leaving reflectance.

The $a(\lambda)$ denotes the contribution of all components present in the aquatic system and is commonly represented into four additive elements, including the pure water (a_w), NAP (a_{NAP}), CDOM (a_{CDOM}) and phytoplankton (a_ϕ), all dependent on wavelength (BABIN et al., 2003; BINDING et al., 2008). In case of pure water, the absorption starts to increase from green to near-infrared (NIR) wavelengths (SMITH and BAKER, 1981). CDOM can remove the blue light in the first layer of the water and exhibit an exponential decrease with increasing wavelength; however, the shape is not equal for all waters (DEKKER, 1993). In order to describe the spectral CDOM absorption, Bricaud et al. (1981) came up with the following model:

$$a_{CDOM}(\lambda) = a_{CDOM}(\lambda_0)e^{-S_{CDOM}(\lambda-\lambda_0)} \quad (3.1)$$

where λ_0 is a reference wavelength, $a_{CDOM}(\lambda_0)$ is the absorption estimate at a reference wavelength, and S_{CDOM} is the spectral slope of the $a_{CDOM}(\lambda)$. The former provides insights about the characteristics of CDOM in terms of chemistry, source and diagenesis (HELMS et al., 2008) and is also a proxy for CDOM composition such as the ratio of fulvic to humic acids and molecular weight (SHANMUGAM et al., 2011). Besides, it is strongly dependent on the wavelength interval chosen for analysis (ROESLER et al., 1989; LOISELLE et al., 2009). The NAP also presents an exponential decrease from short to longer wavelengths and is represented by the spectral slope, S_{NAP}, which is related to the fraction of organic and inorganic matter (BABIN et al., 2003). Meanwhile, phytoplankton presents two distinct absorption features at 443 and 675 nm. Its composition is clearly defined by the water quality and its abundance is essentially determined by the underwater light and nutrient loading (DEKKER, 1993).

The characterization of IOP in ocean and coastal waters have been massively studied in the last four decades, therefore, the comprehension about the relationship between in-water constituents and optical properties are well known (MOREL and MARITORENA, 2001; BABIN et al., 2003). In open ocean, for example, the influence of terrigenous matter is negligible and is assumed that only phytoplankton domain the optical properties as well as the pure water (MOREL and BRICAUD, 1986). In contrast, the inland waters are considered complex environments due to the increased number of color-producing agents and the high variability in their concentrations, limiting the use of empirical oceanic algorithms for Chl-*a* retrieval, for example (BUKATA, 2005). More robust models such as the semi-analytical and analytical approaches require the knowledge about the mass-specific inherent optical properties (SIOPs), like those used by Lee et al. (2002) with the QAA and the Garver-Siegel-Maritorena algorithm (GARVER and SIEGEL, 1997; MARITORENA et al., 2002). The SIOPs are retrieved by normalizing the absorption coefficient of a certain OSC and the respective concentration. The mass-specific phytoplankton absorption (a_{ϕ}^{*}), for example, is related to phytoplankton cell size, accessory pigments and package effect (BRICAUD et al., 1995; BABIN et al., 2003).

Registers of the (S)IOPs in inland waters are available for specific regions around the world such as in Babin et al. (2003) who studied the coastal waters around Europe; Binding et al. (2008) produced a data set of absorption coefficients in Lake Erie; Perkins et al. (2009) documented the spectral features, magnitudes and variability of the IOPs in Finger Lakes of New York; Le et al. (2009b) investigated the variations of absorption and total specific absorption coefficient of phytoplankton in Lake Taihu, China; Campbell et al. (2011) described the SIOPs of three sub-tropical and tropical waters reservoirs in Australia; Wu et al. (2011) estimated the absorption and backscattering coefficients in Poyang Lake, China and analyzed their relations to the main water constituents; Matthews and Bernard (2013) presented the absorption properties of phytoplankton, CDOM and NAP for three small optically-diverse South African inland waters; Ylöstalo et al. (2014) characterized variations of different absorption components between different lake types and seasons in various lakes in the boreal region, in turn, Riddick et al. (2015) showed the spatial variability of absorption coefficients over a biogeochemical gradient in Lake Balaton, Hungary.

Many efforts have been done from the last decade regarding the studies of (S)IOPs in inland waters, however, much more is expected to be done in order to cover a variety of environments and provide subsides to understand how these properties influence the

parameterization of bio-optical models aiming to assist the remote-sensed-based monitoring of water quality. Environments such as reservoirs designed in a cascade system, for example, causes limnological modifications from the upstream to downstream reducing the turbidity and increasing water clarity (BARBOSA et al., 1999). The (S)IOPs can be somehow modulated by biogeochemical filtration from the first to the last reservoirs. The current study aims to characterize two optically different reservoirs situated along the cascade system of Tietê River, whose influence are dictated by the watershed dynamic, in order to improve the knowledge about bio-optical properties of a system covering two distinct trophic states (oligo to hypereutrophic) and to raise the main sources of spatial variability in the IOPs.

3.2 Data and Methods

For this study, data from all the field trips were used. The campaigns of BB were named as BB1, BB2 and BB3 standing for the sequence of field campaigns realization. For Nav, the campaigns were identified as Nav1, Nav2 and Nav3. The number of samples used for this chapter is displayed in Table 3.1.

3.2.1 Water quality parameters

To determine the TSS concentration we applied the method described by APHA (1998). The water volume was filtered on the same day of collection through pre-ashed and pre-weighed Whatmam fiberglass GF/F filter with a nominal porosity of 0.7 μm and then stored at the refrigerator until analysis. The filters were dried in 100° C oven for 12h, and then weighted in an analytical balance. To retrieve the inorganic suspended sediment (ISS), the filter dried and weighed in the last step was subjected to a muffle furnace for 75 min at 550° C and weighted again. As result, we determined the TSS, ISS and to estimate the organic suspended sediment (OSS), the last weighted filter was subtracted to the original filter weight after first drying.

The analysis to determine the Chl-*a* concentration was based on Golterman et al. (1978). The specified volume of water was filtered under low vacuum pressure through a Whatman fiberglass GF/F filter with a porosity of 0.7 μm, and then frozen for laboratory analysis for no longer than 1 week. The chlorophyll was extracted by maceration in 90% acetone, then stored in 20 mL tubes and centrifuged. Afterward, one sample was placed in 1 cm quartz cuvette and to represent the reference a volume of acetone was placed in another cuvette. The readings were made in a spectrophotometer at 663 nm indicating the maximum absorption of chlorophyll in

acetone and at 750 nm characterizing the absorption by chlorophyll and pheophytin. After this reading, 0.1N hydrochloric acid was added to the sample in order to remove magnesium from the chlorophyll and convert it into pheophytin and another reading was taken.

3.2.2 Inherent optical properties

To estimate the CDOM absorption coefficient, $a_{CDOM}(\lambda)$, a volume of water was filtered through a fiberglass Whatman GF/F with porosity of 0.7 μm, and then re-filtered under low vacuum pressure using a nylon membrane filter with porosity of 0.2 μm. The readings were performed using Shimadzu UV-2600 UV-VIS spectrophotometer (SHIMADZU, Japan) in absorbance mode, and the samples were placed in 10 cm quartz cuvettes. For each set of measurements, we performed a reference reading containing Milli-Q water, and for each read sample (OD_{sample}), the reference absorbance value was subtracted (OD_{ref}). The measured optical densities (OD_{sample}) were converted to absorption coefficient by multiplying by 2.303 and dividing by the path length (l = 0.1 m for a 10 cm cuvette). Therefore, the $a_{CDOM}(\lambda)$ was estimated following the equation (TILSTONE et al., 2002):

$$a_{CDOM}(\lambda) = 2.303\frac{OD_{sample}}{l} = 2.303\frac{OD_{sample}}{0.1} \quad (m^{-1}) \tag{3.2}$$

The $a_{CDOM}(\lambda)$ follows an exponential function decreasing from the visible to longer wavelengths. The data adopted to fit to the nonlinear regression ranged from 350 and 500 nm (BABIN et al., 2003). Twardowski et al. (2004) highlighted the main issues related to the spectral variability found in the results of many studies and attribute to the spectral range used in the adjustment. The S_{CDOM} can be used to understand the composition of CDOM (GREEN and BLOUGH, 1994, TWARDOWSKI et al., 2004). Absorption measures may contain errors related to the scattering of small particles or colloids that can cross the filters, leading some researchers to use equations to correct these effects (BRICAUD et al., 1981, GREEN and BLOUGH, 1994, BABIN et al., 2003). In order to turn the results comparable, the procedure described by Babin et al. (2003) were adopted in this study.

For particulate absorption coefficients, water samples were filtered at low vacuum pressure using a 47 mm diameter fiberglass Whatman GF/F filter. The filters were wrapped in aluminum foil and frozen until laboratory analysis. A white filter wetted with ultrapure water was used as reference and the filter containing the particulate was placed on the integrating

sphere module presented in the double-beam Shimadzu UV-2600 UV-VIS spectrophotometer (SHIMADZU, Japan) with spectral sampling ranging from 280 – 800 nm, to measure their optical density (OD). The T-R (Transmittance-Reflectance) method described by Tassan and Ferrari (1995, 1998) was employed to derive the total particulate absorption coefficient (a_p). The particulate filter was submitted to depigmentation by oxidation in 10% sodium hypochlorite (NaClO), ensuring free phytoplankton influence to obtain a_{NAP}. The a_ϕ was retrieved by subtracting the a_{NAP} from the a_p.

$$a_\phi(\lambda) = a_p(\lambda) - a_{NAP}(\lambda) \quad (3.3)$$

The $a_\phi^*(\lambda)$ was obtained by normalizing the absorption due to phytoplankton by the Chl-*a* concentration. Babin et al. (2003) highlight that a_ϕ includes absorption related to all pigments, incorporating phaeopigment associated with other particles other than living phytoplankton. The a_{NAP} can be adjusted by Roesler et al. (1989):

$$a_{NAP}(\lambda) = a_{NAP}(\lambda_0)e^{-S(\lambda-\lambda_0)} \quad (3.4)$$

The fit of the model was carried out between 350 and 800 nm, excluding the interval between 400 – 480 and 620 – 710 nm related to the absorption of some type of pigment interval that may have remained after depigmentation (BABIN et al., 2003).

3.3 Results

3.3.1 General characteristics of water quality parameters and optical properties

The water quality parameters as well as the optical properties were all analyzed in terms of field trips (Table 3.1). Thus, the average turbidity between BB1 and BB2 was statistically different (p-value < 0.05) and the same happened between BB2 and BB3. On the other hand, data from BB1 and BB3 were not statistically different (p-value > 0.05). The same result was also observed for Chl-*a* and TSS concentrations. The increase of Chl-*a* concentration in October of 2014 was due to the drought effect leading to flow reduction and longer retention time (WATANABE et al., 2016b). High values of Chl-*a* for BB revealed the eutrophication status of the water, mainly in the winter (LUZIA, 2004). In Nav, the average turbidity from Nav1 and

Nav2 was not considered statistically different (*p*-value > 0.05), however, the average Chl-*a* concentration from all three field trips was statistically different. The average TSS from Nav1 and Nav2 was not different, but this was not true when data from Nav2 was compared to Nav3 and Nav1 with Nav3. Assessing both reservoirs, we clearly observe that BB is more turbid due to high contribution of phytoplankton mainly in the BB2 that achieved a Chl-*a* value of 797.80 μg l^{-1} close to the dam. On the contrary, Nav presented low concentrations of Chl-*a*, where the average did not exceed 9.0 μg l^{-1} for Nav1 and Nav2 but reached 26.4 μg l^{-1} in Nav3, where the samples were concentrated at the upstream region of the reservoir. The variation of water quality parameters was strictly related to rainfall condition as well as the location of each reservoir in the cascade system. The analysis of individual reservoirs cannot provide the necessary information about the water quality dynamic, because this kind of structure cause discontinuity in the physical and biological features (BARBOSA et al., 1999).

Table 3.1. Descriptive statistics of water quality and optical parameters. The notations Min-Max, Aver, SD, CV and *n* stand for minimum-maximum, average, standard deviation, coefficient of determination and number of samples. Blank spaces represent lack of data.

		Nav1	**Nav2**	**Nav3**	**BB1**	**BB2**	**BB3**
Chl-*a*	Min–Max	2.5–12.6	4.5–20.5	15.8–38.6	17.8–279.9	263.2 – 797.8	62.8–245.7
(μg l^{-1})	Aver ± SD	6.2±2.5	9.0±4.1	26.4±6.7	120.4±68.5	428.7±154.5	127.1±51.3
	CV (%)	40.0	45.5	25.3	56.9	36	40.4
	n	20	19	10	20	20	24
TSS	Min–Max	0.1–2.6	0.5–2.8	1.9–5.3	3.6–16.3	10.8–44.0	1.6–8.4
(mg l^{-1})	Aver ± SD	1.0±0.6	1.0±0.6	3.1±1.0	7.2±3.9	22.0±7.0	5.6±1.8
	CV (%)	61.7	56.2	32.4	44.1	32.1	32.0
	n	17	19	10	20	20	24
OSS	Min–Max	-	-	-	2.8–14.7	10.2–30.4	-
(mg l^{-1})	Aver ± SD	-	-	-	6.1±2.6	18.2±3.5	-
	CV (%)	-	-	-	41.9	19.3	-
	n	-	-	-	20	19	-
Turbidity	Min–Max	1.0–2.5	1.0–2.6	-	1.7–12.5	11.6–33.2	3.1–6.8
(NTU)	Aver ± SD	1.7±0.4	1.7±0.4	-	5.8±2.4	18.6±5.3	4.2±0.8
	CV (%)	25.4	22.9	-	45.8	28.3	20.3
	n	20	19	-	20	20	24
SDD	Min–Max	2.3–4.8	2.5–4.7	1.9–3.8	0.8–2.3	0.4–0.8	1.0–1.6
(m)	Aver ± SD	3.2±0.6	3.4±0.6	3.0±0.6	1.5±0.4	0.6±0.1	1.3±0.2
	CV (%)	20.0	17.6	21.0	28.2	17.2	16.6
	n	20	19	18	20	20	24
Depth	Min–Max	5.3–30.0	-	7.4–32.9	10.0–30.0	8.0–18.5	9.6–26.0
(m)	Aver ± SD	18.0±8.3	-	22.9–6.8	15.4±4.1	13.0±2.7	16.3±3.7
	CV (%)	46.2	-	29.8	26.5	21.0	22.5
	n	20	-	18	19	20	24
$a_\phi(443)$	Min–Max	0.1–0.4	0.1–0.4	0.1–0.6	0.3–2.4	-	-
(m^{-1})	Aver ± SD	0.2±0.1	0.2±0.1	0.3±0.1	1.1±0.6	-	-
	CV (%)	39.1	40.8	43.5	52.1	-	-
	n	20	20	19	20	-	-
	Min–Max	0.1–0.5	0.1–0.7	0.4–0.8	0.3–0.8	-	-

$a_{NAP}(443)$ (m^{-1})	Aver ± SD	0.3±0.1	0.3±0.1	0.6±0.1	0.5±0.1	-	-
	CV (%)	25.8	52.0	19.6	25.4	-	-
	n	20	20	19	20	-	-
$a_{CDOM}(443)$ (m^{-1})	Min–Max	0.2–0.3	0.2–0.5	0.06–0.09	0.6–1.1	-	-
	Aver ± SD	0.3±0.0	0.3±0.1	0.08±0.01	0.7±0.1	-	-
	CV (%)	8.5	17.0	8.9	14.2	-	-
	n	20	19	19	20	-	-

Water quality properties such as TSS and Chl-*a* as well as the IOPs at 443 nm were plotted against each other aiming to provide the main constitution of both reservoirs. No significant linear relationship (*p*-value > 0.05) was observed between TSS and Chl-*a* (Figure 3.1a) for Nav considering a log scale (Nav1: R = 0.44; Nav2: R = -0.18; Nav3: R = 0.42), which means that Nav is not dominated by phytoplankton. However, for BB, there is a significant relationship for all three field trips (BB1: R = 0.75, *p*-value < 0.001; BB2: R = 0.60, *p*-value < 0.05; BB3: R = 0.74, *p*-value < 0.001) showing that phytoplankton was the main contributor of TSS. $a_{\phi}(443)$ and Chl-*a* concentration (Figure 3.1b) did not show significant relationship (*p*-value > 0.05) for Nav1 (R = 0.42) and Nav2 (R = -0.22) on the other hand, for Nav3, we observed a strong linear relationship (R = 0.81, *p*-value < 0.05). For BB, the correlation was statistically significant for both BB1 (R = 0.92, *p*-value < 0.001) and BB2 (R = 0.52, *p*-value < 0.05). As reported by Le et al. (2015), the strong correlation between $a_{\phi}(443)$ and Chl-*a* is associated with high loads of nutrients in the aquatic system increasing phytoplankton production. According to Luzia (2004), the limiting nutrient that controls the growth of aquatic plants in majority of fresh waters is the inorganic form of phosphorus.

Considering the relationship between $a_{NAP}(443)$ and TSS (Figure 3.1c) for Nav, it was difficult to notice any relationship (Nav1: R = 0.27; Nav2: R = -0.11; Nav3: R = 0.33, *p*-value > 0.05). For BB, the non-correlation was also observed for both field trips (BB1: R = -0.05; BB2: R = -0.37, *p*-value > 0.05). Now considering the relationship between $a_{CDOM}(443)$ and Chl-*a* (Figure 3.1d) for Nav, again, no correlation was observed in any of the three campaigns (Nav1: R = 0.14; Nav2: R = 0.15; Nav3: R = 0.17, *p*-value > 0.05), while for BB1 the relationship was significant (R = 0.77, *p*-value < 0.001) and weak for BB2 (R = 0.25, *p*-value > 0.05). Regarding the relationship between $a_{CDOM}(443)$ and TSS (Figure 3.1e), Nav did not show any statistical correlation (Nav1: R = -0.06; Nav2: R = -0.18; Nav3: R = 0.14, *p*-value > 0.05) whilst BB1 showed to be moderately (R = 0.53, *p*-value < 0.05) and weakly correlated for BB2 (R = 0.19, *p*-value > 0.05). The non-correlation combined with the low Chl-*a* in Nav can indicate that TSS and CDOM were possibly originated from land-based sources and not from phytoplankton degradation.

Figure 3.1. Relationship between water quality and optical parameters considering data from all field campaigns. (a) TSS versus Chl-*a*, (b) $a_{\phi}(443)$ versus Chl-*a*, (c) $a_{NAP}(443)$ versus TSS, (d) $a_{CDOM}(443)$ versus TSS and (e) $a_{CDOM}(443)$ versus Chl-*a*.

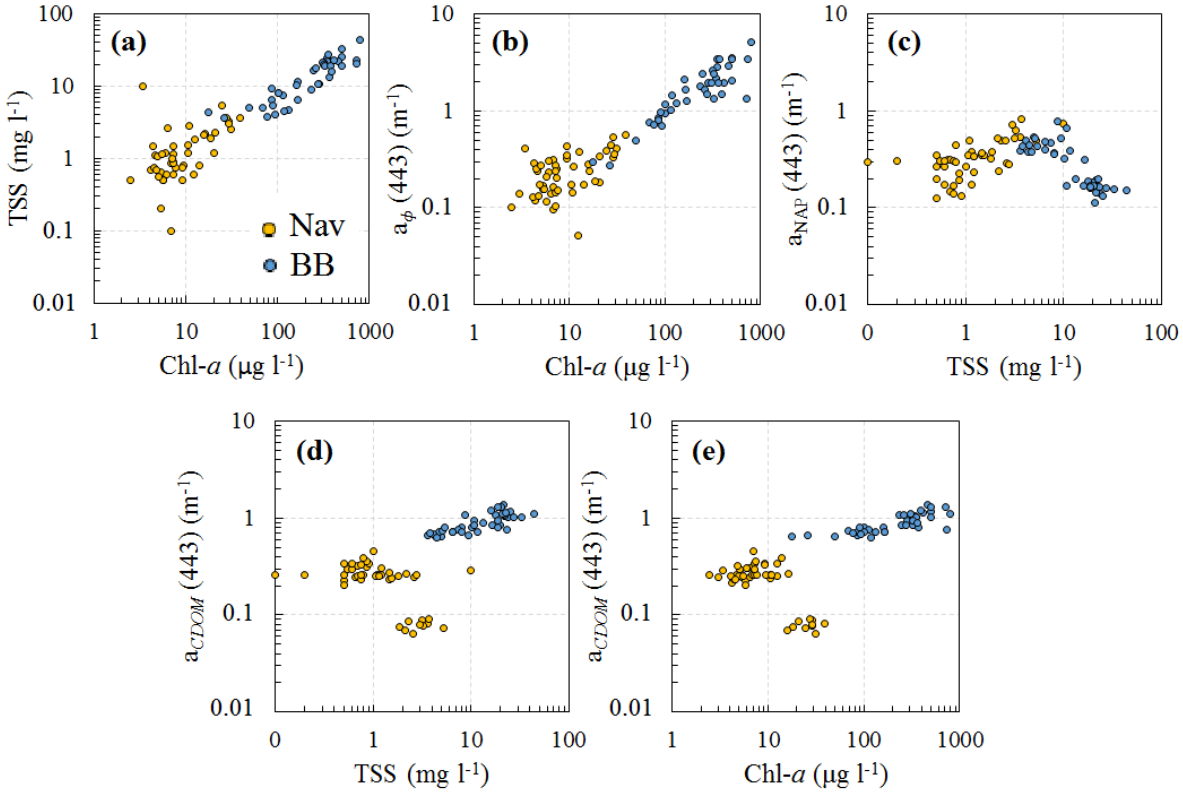

3.3.2 Absorption coefficient budget

The relative contribution of phytoplankton, CDOM and NAP relative to the total absorption without the water fraction (a_{t-w}) can be seen in Figure 3.2. The wavelengths chosen for analysis (443, 560 and 665 nm) characterize the light interaction with dissolved organic matter and particulate matter (BABIN et al., 2003; LE et al., 2013). The ternary plots show the contribution and representativeness of certain OSC in the water and can be used to assist the estimation of these components using proper algorithms (MISHRA et al., 2014; RIDDICK et al., 2015). Figure 3.2(a) shows that at 443 nm, Nav1 was dominated by a_{NAP} with 43.24 ± 6.52 %, Nav2 by a_{CDOM} with 37.89 ± 9.22 %, Nav3 by a_{NAP} 62.17 ± 9.39 %. At 560 nm (Figure 3.2b), Nav1, Nav2 and Nav3 were all dominated by a_{NAP} with 48.57 ± 7.42 %, 46.87 ± 10.11 % and 72.14 ± 13.70 %, respectively. At 665 nm (Figure 3.2c), all three field trips were dominated by a_{ϕ} (Nav1: 55.00 ± 8.95 %, Nav2: 39.72 ± 12.06 % and Nav3: 65.16 ± 12.39 %).

As expected, the most dominant OSC in the absorption budget considering both field trips and wavelengths in BB was the phytoplankton. At 443 nm (Figure 3.2a), BB 1 and BB 2

were dominated by a_ϕ with a percentage of 45.72 ± 12.71 % and 72.38 ± 9.36 %. At 560 nm (Figure 3.2b), the a_ϕ of BB 1 and BB 2 presented a percentage of 41.98 ± 13.43 % and 63.33 ± 13.75 %, respectively while at 665 nm (Figure 3.2c), the contribution was over 80% (BB 1 = 85.38 ± 6.80 % and BB 2: 87.90 ± 6.38 %).

Figure 3.2. Ternary plot depicting the absorption coefficient budget of both Nav and BB reservoirs at three wavelengths: (a) 443 nm, (b) 560 nm and (c) 665 nm.

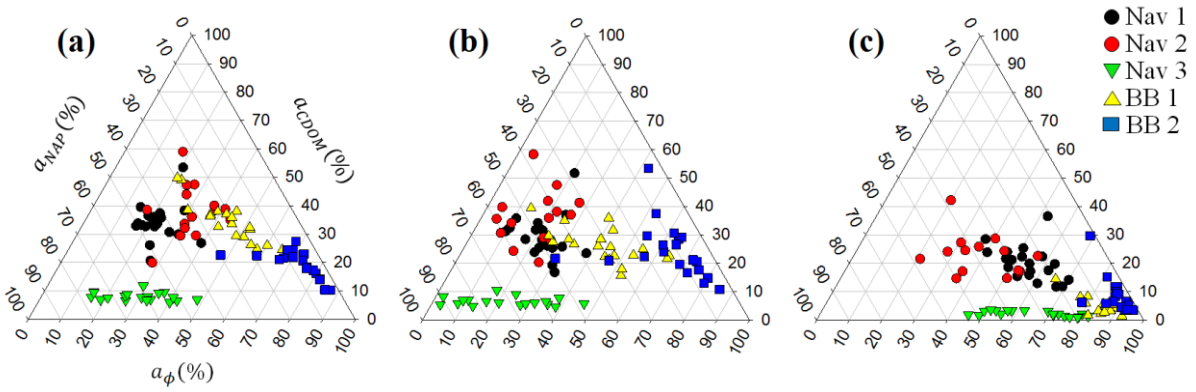

3.3.3 CDOM absorption

The a_{CDOM} spectra approached to zero close to 700 nm and showed an exponential decrease pattern from shorter to higher wavelengths (BRICAUD et al., 1981) with values at 443 nm ranging between 0.06 to 0.45 m^{-1} in Nav and between 0.62 to 2.34 m^{-1} in BB (Figure 3.3). The magnitude differs from one reservoir to another as well as from one season to another. Values from BB are like those found by Matthews and Bernard (2013), who stated an interval between 0.63 to 4.13 m^{-1} in three South African reservoirs. Wu et al. (2011) found values ranging between 0.33 to 1.01 m^{-1} in Poyang Lake, China, considered a suspended inorganic matter dominated water with low Chl-*a* concentration (1.47 – 24.65 µg l^{-1}) while Campbell et al. (2011) reported an interval of 0.36 and 1.59 m^{-1} in three Australian reservoirs. Zhang et al. (2007) observed in Lake Taihu values ranging between 0.27 to 2.36 m^{-1}. Binding et al. (2008) reported values at 440 nm ranging between 0.08 to 0.75 m^{-1} in Lake Erie (Canada/USA) that was close to that found in Nav. The mean value for the spectral slope of CDOM (S_{CDOM}) was 0.018 nm^{-1} for BB1 and 0.016 nm^{-1} for BB2, whilst for Nav1 the mean S_{CDOM} was 0.020 nm^{-1} and 0.018 nm^{-1} for Nav2 and Nav3. Riddick et al. (2015) also found a mean S_{CDOM} of 0.018 nm^{-1} in Kis-Balaton (wetland system) and 0.020 nm^{-1} in the Lake Balaton (freshwater lake in central Europe). On the other hand, Babin et al. (2003) reported a narrow range around 0.0176

nm^{-1} in coastal waters around Europe. The authors highlighted that diverse protocols to retrieve S_{CDOM} can make it difficult to compare values from different regions.

Figure 3.3. Variability of a_{CDOM} by field trip. (a) Nav1, (b) Nav2, (c) Nav3, (d) BB1, (e) BB2 and (f) the average value of $a_{CDOM}(\lambda)$ for each field trip. Different y axes were applied for Nav and BB due to magnitude discrepancies.

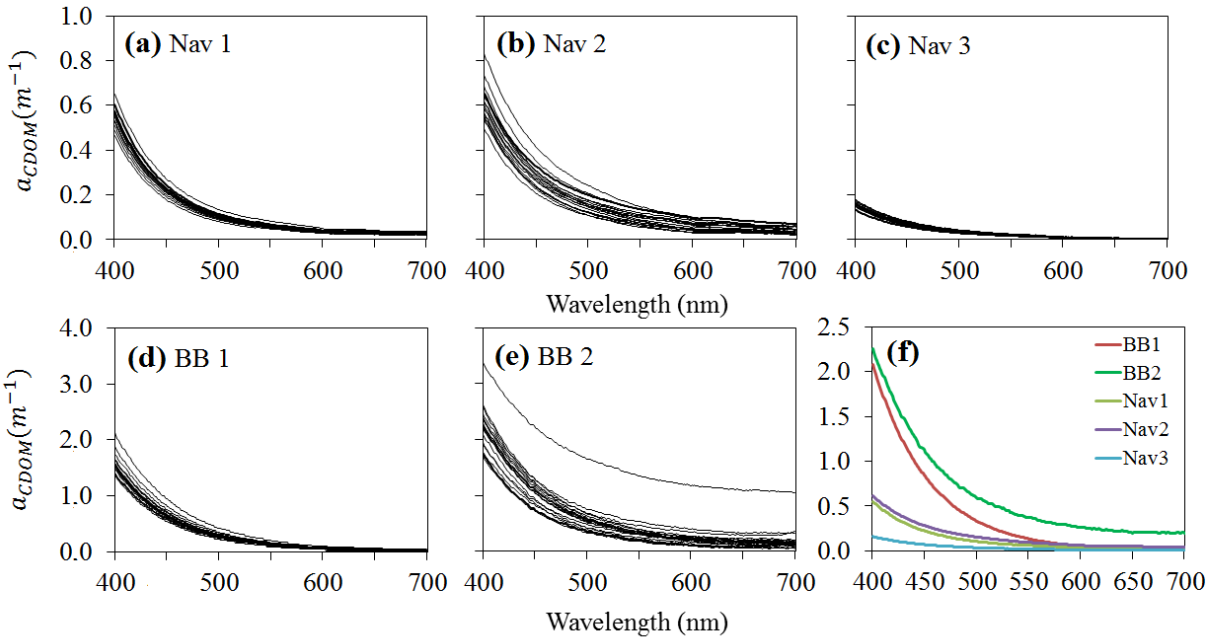

3.3.4 Phytoplankton absorption

Figure 3.4 depicts the a_{ϕ} spectra between 400 to 700 nm. The magnitude and shape are different when we compare both reservoirs and this can be due to the diversity of trophic states and phytoplankton assemblages (MATTHEWS and BERNARD, 2013). The peaks at the blue and red regions are consistent with the typical diagnostic features of phytoplankton absorption (WU et al., 2011). At 440 nm, accessory pigments and Chl-*a* contribute with high absorption, while at 675 nm, Chl-*a* plus phaeophytin are primarily responsible for high absorption (SATHYENDRANATH et al., 1987; LE et al., 2009b). Other pigments such as carotenoids absorb from 460 to 490 nm, however, this feature is not prominent in Nav neither BB.

The absolute intervals of absorption at 443 nm are 0.05 – 0.57 m^{-1} for Nav and 0.27 – 10.34 m^{-1} for BB. Roesler et al. (1989) found values at 400 nm between 0.03 to 0.58 m^{-1} in inland marine waters in the USA, which was very close to that found in Nav. High values were reported in many turbid inland waters with characteristics close to that presented in BB (WU et

al., 2011, MATTHEWS and BERNARD, 2013, MISHRA et al., 2014). a_ϕ at 443 nm exhibited an increased trend from the first to the second field campaigns, and the same happened for Nav considering the first to the third field trips.

Mean $a_\phi(620)$ ranged from 0.33 to 1.47 m^{-1} in BB and 0.04 to 0.10 m^{-1} in Nav. Chl-*a* concentration showed a strong relationship with $a_\phi(620)$ and BB1 (R^2 = 0.80, $p < 0.001$, not presented here) but no correlation was found with BB2 (R^2 = 0.11, $p > 0.05$) as well as with Nav considering all three field trips ($p > 0.05$). The pigment phycocyanin, when present, can be detected through the a_ϕ spectrum especially at 620 nm. This pigment is a marker for cyanobacteria in eutrophic inland waters (SIMIS et al., 2005). Figure 3.1(b) showed the non-relationship between $a_\phi(443)$ and Chl-*a* in Nav, suggesting that Chl-*a* was not the only pigment affecting a_ϕ, but other accessory pigments, such as carotenoid (WU et al., 2011).

Figure 3.4. Variability of a_ϕ by field trip. (a) Nav1, (b) Nav2, (c) Nav3, (d) BB1, (e) BB2 and (f) the average value of $a_\phi(\lambda)$ for each field trip. Different y axes were applied for Nav and BB due to magnitude discrepancies.

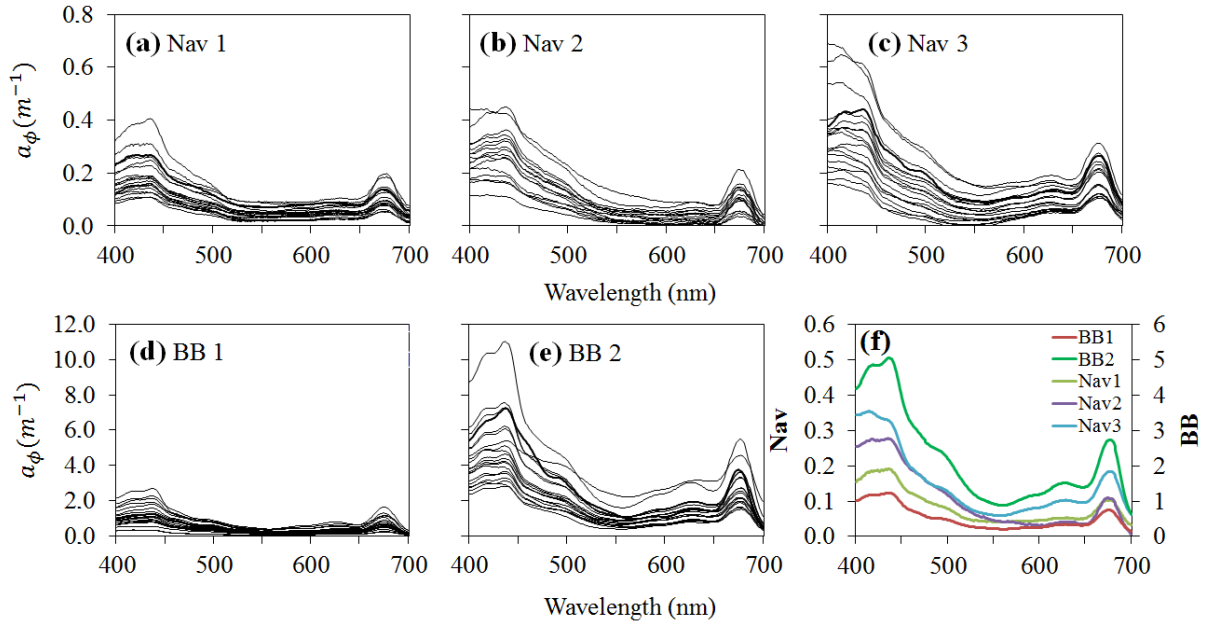

3.3.5 NAP absorption

The spectral shape of a_{NAP} (Figure 3.5) is quite similar of a_{CDOM} with an exponential decrease from 400 to 700 nm. Visually, the seasonal pattern between field campaigns and reservoirs did not show remarkable changes as reported previously. Taking into account the data from Nav, we observed that at 443 nm the values varied from 0.13 to 0.82 m^{-1} with averages varying from 0.33 m^{-1} in Nav1, 0.27 m^{-1} in Nav2 and 0.61 m^{-1} in Nav3, showing that $a_{NAP}(443)$

increased in Nav3. Sample 5 from Nav2 stood out from the dataset because of the presence of sand dredging activity in that region leading to sediment resuspension. Meanwhile, BB showed a range of 0.23 to 1.67 m^{-1} with averages varying from 0.45 m^{-1} in BB1 and 0.47 m^{-1} in BB2. Samples 17 to 20 placed at Tietê River and confluence of Tietê and Piracicaba Rivers presented the highest values for $a_{NAP}(443)$. These regions receive high loads of sediment from the metropolitan region of São Paulo. The mean slope (S_{NAP}) of BB1 and BB2 was 0.007 and 0.008 nm^{-1}, respectively, ranging between 0.006 to 0.01 nm^{-1} while for Nav the mean values were 0.009, 0.006 and 0.007 nm^{-1}, respectively, ranging between 0.003 to 0.011 nm^{-1}.

Figure 3.5. Variability of $a_{NAP}(\lambda)$ in all field trips (a) Nav1, (b) Nav2, (c) Nav3, (d) BB1, (e) BB2 and (f) the average value of $a_{NAP}(\lambda)$ for each field trip.

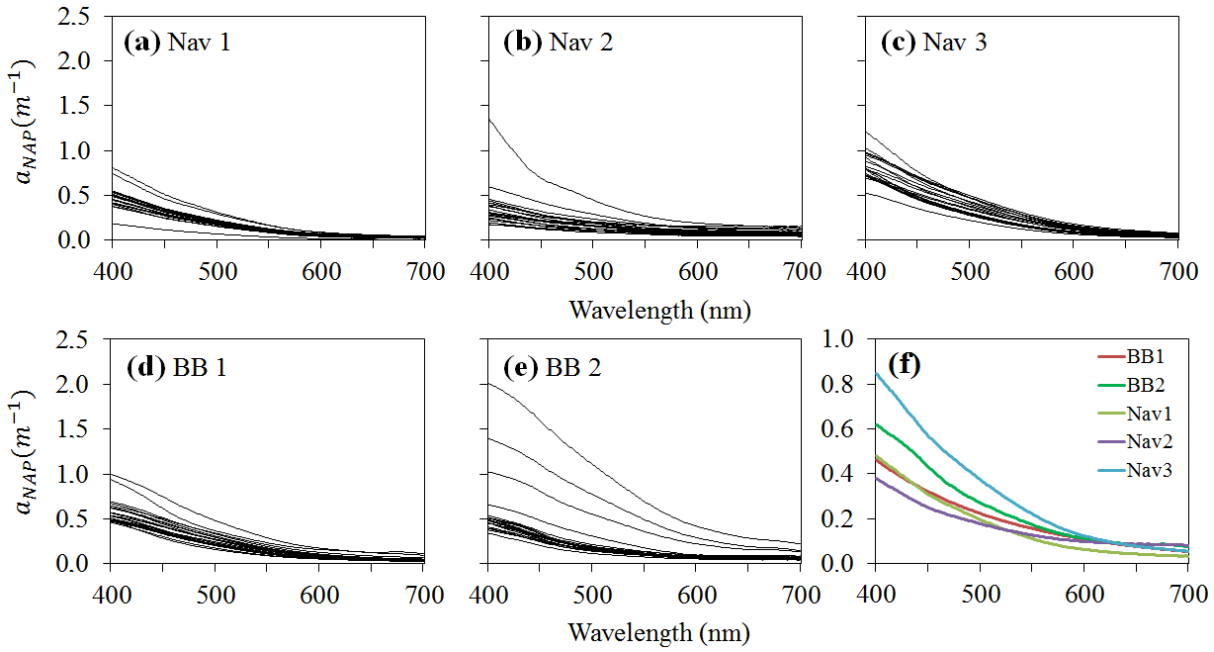

3.3.6 Particle absorption

The Figure 3.6 displays the spectral behavior of a_p from 400 to 700 nm. It shows the contribution of phytoplankton and non-algal particle. Besides the magnitude, the shapes of a_p from BB and Nav are clearly different, showing a smooth feature between 400 to 450 nm in Nav and a marked feature in BB. These are due to the high contribution of NAP and CDOM at this wavelength range, as also supported by Figure 3.1. On the contrary, BB was highly affected by photosynthetic pigments at the blue and red regions. The pattern from Nav was also observed by Meler et al. (2016) in Gulf of Gdánsk during winter and in river mouths, Baltic Sea during

all seasons except summer. Wu et al. (2011) did not observe any feature at the blue and red regions due to high loads of inorganic sediment, which masked the phytoplankton contribution along the spectra.

Figure 3.6. Variability of $a_p(\lambda)$ in all field trips. (a) Nav1, (b) Nav2, (c) Nav3, (d) BB1, (e) BB2 and (f) the average value of $a_p(\lambda)$ for each field trip. Different y axles were applied for Nav and BB due to magnitude discrepancies.

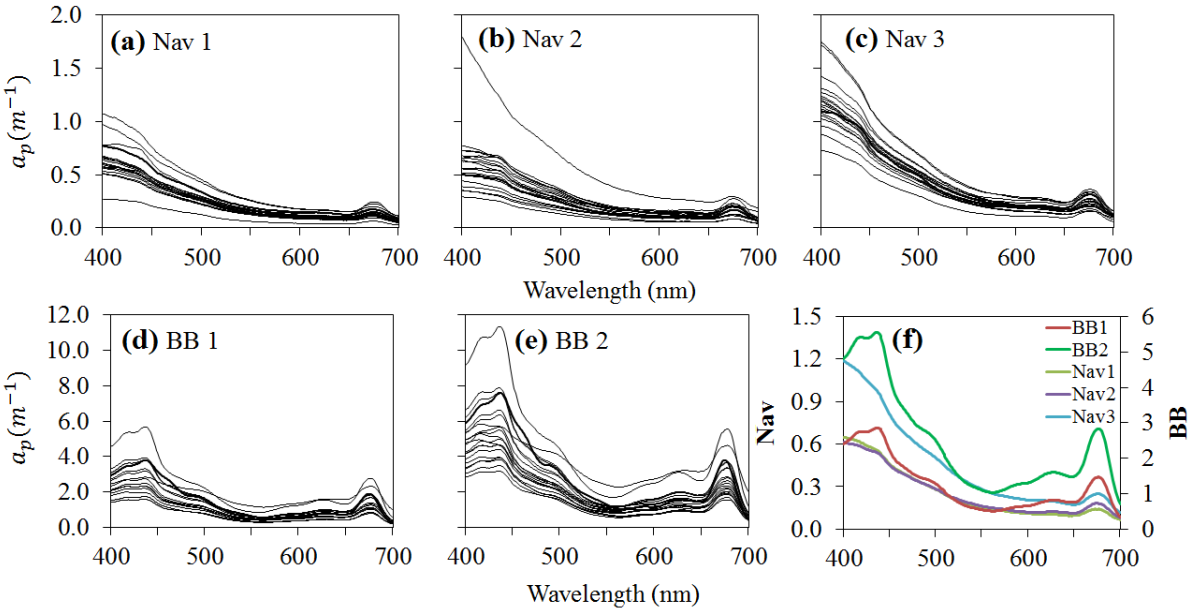

3.4. Discussion

As reported in many studies, BB as the first reservoir of the cascade system receives high loads of sediments coming from the metropolitan region of São Paulo and also from the Piracicaba River basin therefore, it acts as a great accumulator of nutrients (BARBOSA et al., 1999, LUZIA, 2004, SMITH et al., 2014). The following reservoirs, on the other hand, start to receive less nutrients decreasing the trophic state of these water bodies, such as Nav. The implication of different sources of contaminant of the reservoirs characterizes the in-water constituents. In case of BB, the ternary plot (Figure 3.2) showed that phytoplankton was the constituent that dominated the water content in the visible spectrum and therefore, the water optical properties. At 443 nm, the phytoplankton contribution ranged between 20.71 to 87.14%. On the other hand, Nav was dominated by both NAP and CDOM considering all three field trips. Nav1 was dominated by NAP (25.87 – 52.25%), Nav2 by CDOM (19.90 – 58.88%) and Nav3 also by NAP (44.85 – 76.76%). Riddick et al. (2015) showed a phytoplankton variation

of 20 to 70% in Lake Balaton, whilst in coastal and sea waters, the contributions of NAP and CDOM, respectively, were dominant (BABIN et al., 2003; NAIK et al., 2013). A particularity was highlighted by Ylostalo et al. (2014) who found high CDOM contribution in Borel lakes (48 – 99% at 442 nm), which most of these lakes present low productivity and high organic matter coming from the catchment basin. In Brazil, Ogashawara et al. (2016) also reported the dominance of CDOM in the a_{t-w} at 443 nm in both Funil and Itumbiara reservoirs. CDOM can be originated by autochthones or allochthones sources and in sea waters this OSC co-varies with phytoplankton biomass (BRICAUD et al., 1981), on the other hand, in inland waters the organic matter is mainly regulated by terrigenous inputs (Kirk 1994). These findings showed that inland waters present high variability in terms of optical properties and this can be reflected in bio-optical modeling.

The dominance of phytoplankton in BB can be due to high loads of nutrients mainly phosphorus that increases the primary production (here represented by Chl-*a* as phytoplankton biomass proxy). Inputs of phosphorus in the water is result of industry, domestic and agriculture activities, including sediment liberation (CALIJURI et al., 2002). High loads of this nutrient were reported in BB during summer (LUZIA, 2004, SMITH et al., 2014). It was observed that Chl-*a* was highly correlated ($0.60 < R < 0.75$) with TSS in all three BB field trips, assuming that the sediment produced in the aquatic system was represented mainly by phytoplankton. Zhang et al. (2009a) showed the influence of seasonal and temporal cycle into Chl-*a* concentration. They observed a significant positive correlation with TSS during spring, summer and autumn and related this to the frequent algal blooms in Lake Taihu, China. Algal blooms were also observed during BB2 campaign and the presence of cyanobacteria was also noticed (Figure 3.4e). Sotero-Santos et al. (2006) pointed relevant conditions to grant cyanobacteria to bloom almost year-round in BB and they were: water column stability, low N:P ratio, moderate to high nutrient levels, mild or no winds and low turbulence.

On the contrary, Nav showed the dominance of NAP in the absorption budget corroborated to the non-correlation between Chl-*a* and TSS (Figure 3.1a). Reservoirs work as an effective trap for phosphorus and the concentration can decline from 80 to 90% during the transition of water through a reservoir (STRASKRABA, 1994). This finding was described by Luzia (2004), who registered a decrease of 93% of phosphorus from BB to Três Irmãos, the last reservoir of the cascade system of Tietê River. Thus, the reduction of the limiting nutrient lead also to reduction of primary production in downstream reservoirs such as Nav, which presented very low Chl-*a* concentration. However, studying the upstream portion of Nav in Tietê River

to be exact, Cicerelli (2013) found the presence of phycocyanin (7.12 ± 10.05 µg l^{-1}) and high Chl-*a* concentration (47.54 ± 34.21 µg l^{-1}) in the summer with maximum Chl-*a* of 150.96 µg l^{-1}. The author attributed this outcome to the combination of high temperature, rainfall and low wind speeds leading to the increase of turbidity, decrease of dissolved oxygen possibly related to the decomposition of organic matter. This means that rainfall provide optimal meteorological conditions for bloom formation during summer and many sources of nutrients can induce the algal blooms such as animal waste, agriculture and fertilizer runoff from the watershed (AHN et al., 2002; ANDERSON et al., 2002).

The IOPs as well as the OSCs parameters showed seasonal and local variability considering both BB and Nav reservoirs. A decrease of organic matter from BB to Nav was reflected in $a_{CDOM}(443)$ values and the correlation between $a_{CDOM}(443)$ and Chl-*a* in BB1 (Figure 3.1d) suggest that the source of CDOM was originated from the decomposition of algal and aquatic vegetation within the reservoir. The low correlation observed in BB2 even with high concentrations of Chl-*a* can be explained by the delay between algal bloom and Chl-*a* degradation that starts to occur after the spring bloom promoting the increase of CDOM absorption. This situation was reported by Sasaki et al. (2005), who studied Funka Bay in Japan and observed a time lag between the beginning of increasing both CDOM absorption and Chl-*a* concentration relationship. Zhang et al. (2009c) observed that phytoplankton can be an important CDOM producer in eutrophic waters and its degradation can release nutrients in a very rapid way being remineralized as nutrient input to the next phytoplankton bloom.

Differently, Nav did not show any correlation between both variables, strongly suggesting the allochthonous source of CDOM. The average $a_{CDOM}(443)$ in BB ranging between 0.62 to 2.34 m^{-1} was coherent with values from turbid inland waters such as Lake Taihu, very known about its high productivity. Meanwhile, Nav showed values comparable to those from Lake Erie ($a_{CDOM}(440)$ ranging from 0.08 to 0.75), also with low Chl-*a* concentration and no correlation between $a_{CDOM}(440)$ and Chl-*a*. In addition, the S_{CDOM} from both reservoirs agreed with those mentioned in the literature for coastal and inland waters. Nav showed a variation of 0.016 to 0.023 nm^{-1} with a mean of 0.019 nm^{-1} whilst BB ranged between 0.014 to 0.019 nm^{-1} with a mean of 0.018 nm^{-1}. High S_{CDOM} values (0.011 – 0.025 nm^{-1}) were reported by Babin et al. (2003), who studied a variety of European waters, and Binding et al. (2008), who verified a range between 0.013 to 0.020 nm^{-1} in Lake Erie. S_{CDOM} can be an indicative of CDOM molecular weight and low S_{CDOM} implies high molecular weight and less-

altered CDOM, on the other hand, steeper slopes is related to low molecular weight and high degraded CDOM (TWARDOWSKI et al., 2004; BELZILE and GUO, 2006).

As previously described, the average $a_\phi(\lambda)$ performed for BB and Nav showed distinct features along the spectrum with high differences in magnitudes. The average $a_\phi(\lambda)$ normalized by $a_\phi(443)$ showed distinctions between data from both reservoirs (Figure 3.7a). As we can see at wavelengths toward the ultraviolet region, Nav3 stood out from the others indicating an increasing trend of absorption at this spectral region. We can see at Figure 3.6c that some curves presented an exponential trend at shorter wavelengths, masking the diagnostic feature of phytoplankton pigment at 443 nm. Binding et al. (2008) reported a portion of the particulate absorption that cannot be assigned to phytoplankton pigments, mineral sediments, or organic detritus but can be attributed to particle-bound dissolved organic matter. The authors also highlighted that this fraction can be retained during filtration and incorporated into phytoplankton absorption signal giving this exponential shape, besides, they affirmed that this situation is more predominant in mineral dominated waters even with moderate concentrations of dissolved organic matter. The shape of Nav3, BB1 and BB2 was quite similar from 450 to 700 nm and a feature between 550 to 650 nm was also enhanced in all three spectra being characteristic of phycobilipigments (phycocyanin) (MATTHEWS and BERNARD, 2013).

Figure 3.7. (a) Variation of $a_\phi(\lambda)/a_\phi(443)$ ratio as a function of wavelength considering the average values of BB and Nav and the mass-specific absorption of phytoplankton, $a^*_\phi(\lambda)$, for all field campaigns (b) Nav1, (c) Nav2, (d) Nav3, (e) BB1 and (f) BB2.

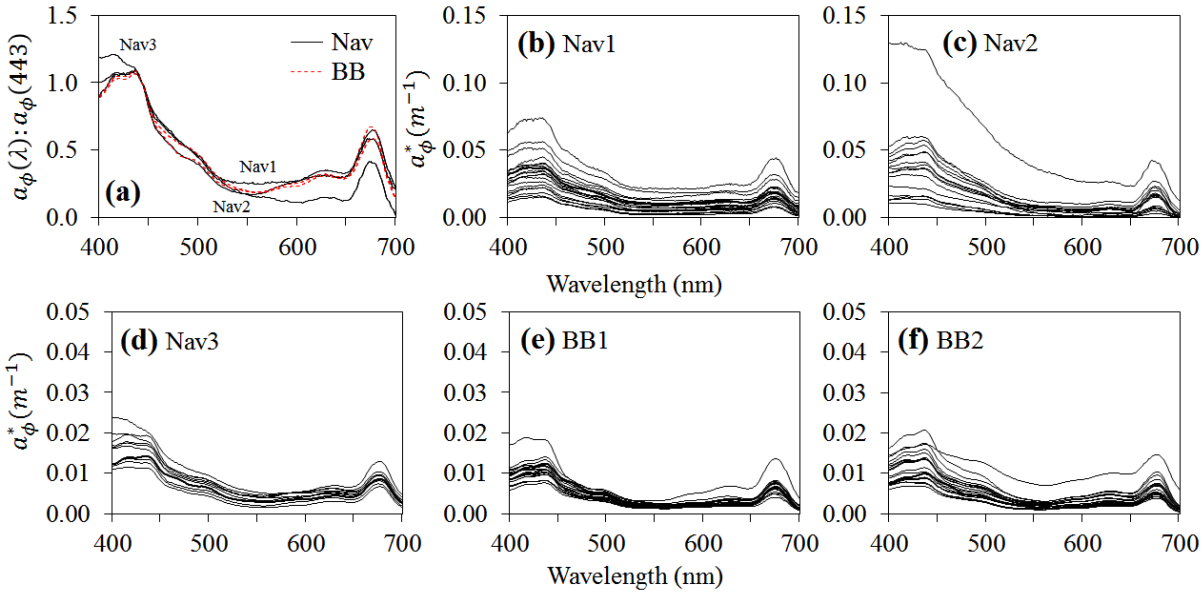

According to Bricaud et al. (1995) the $a_{\phi}^{*}(\lambda)$ values tend to decrease with increasing Chl-*a* concentrations probably due to package effect, which can be observed at Figure 3.7 (b-f) with Nav1 and Nav2 presenting a higher $a_{\phi}^{*}(\lambda)$ values for axis y in relation to Nav3, BB1 and BB2. The $a_{\phi}^{*}(443)$ and $a_{\phi}^{*}(675)$ are absorption features of Chl-*a* and the accessory pigment. The average of $a_{\phi}^{*}(675)$ values for Nav1, Nav2 and Nav3 were 0.018, 0.003 and 0.009 m^2 mg^{-1}, respectively whilst for BB1 and BB2, the values were 0.004 and 0.007 m^2 mg^{-1}. Matthews and Bernard (2013) highlighted that the mean value of $a_{\phi}^{*}(443)$ is affected by the trophic state of the water decreasing from oligotrophic to hypertrophic classes. In this case, the mean $a_{\phi}^{*}(443)$ values related to Nav1, Nav 2 and Nav3 were 0.032, 0.035 and 0.015 m^2 mg^{-1} and for BB1 and BB2 were 0.007 and 0.011 m^2 mg^{-1}, which agreed with the previous authors.

Nav produced an average S_{NAP} of 0.007 ± 0.002 nm^{-1} and BB of 0.008 ± 0.001 nm^{-1}, which is close to the ones found in other reservoirs (0.0095 ± 0.0004 nm^{-1}, 0.0103 ± 0.0013 nm^{-1} and 0.0098 ± 0.0011 nm^{-1} [MATTHEWS and BERNARD, 2013] and the ranges 0.008 – 0.0088, 0.0123 – 0.0153 and 0.0086 – 0.0089 [CAMPBELL et al., 2011]) or Lake Erie (0.0077 – 0.017 nm^{-1} [BINDING et al., 2008]) and lakes in boreal region (0.0075 – 0.0128 nm^{-1} [YLOSTALO et al., 2014]) but below the values reported by Riddick et al. (2015) who found an average of 0.015 ± 0.004 nm^{-1} in Lake Balaton. Values from ocean were also higher than the ones found in Nav and BB (0.0094 ± 0.0018 nm^{-1} [BRICAUD et al., 2010] and 0.011 ± 0.0025 nm^{-1} [BRICAUD et al., 1998]) or even coastal waters (0.0123 ± 0.0013 nm^{-1} [BABIN et al., 2003]). This variability can be related to proportion of mineral and organic fraction that was suggested by Babin et al. (2003) after observe that a low S_{NAP} (average 0.0117 nm^{-1}) was assigned to waters with mineral particles whilst high S_{NAP} (average 0.0128 nm^{-1}) was linked to organic matter dominated water. However, Riddick et al. (2015) found the opposite relationship as well as Binding et al. (2008) and Ylostalo et al. (2014) who did not found any trend between S_{NAP} and organic content of TSS. According to Figure 3.8a, we can observe the small variability between Nav and BB slopes not showing a wide range of particle types, however, following the logic from Babin et al. (2003), BB depicted the highest values in comparison with Nav suggesting the organic matter dominating composition. To test this hypothesis and regarding the availability of OSS data from BB, Figure 3.8b depicted an increase trend between organic matter and S_{NAP}, agreeing with Babin et al. (2003).

Figure 3.8. (a) Variation of $a_{NAP}(\lambda)/a_{NAP}(443)$ ratio as a function of wavelength considering the averages values of BB and Nav and (b) the relationship between S_{NAP} and OSS (mg l^{-1}) from BB.

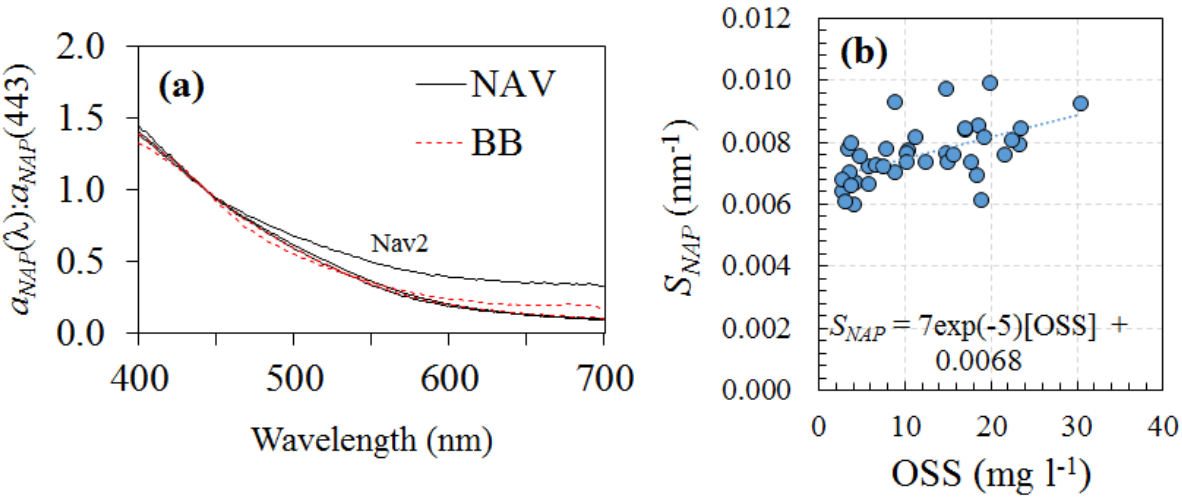

3.5 Conclusion

The OSCs collected between 2014 to 2016 showed considerable changes between BB and Nav, and according to the relationship between TSS and Chl-*a* we could have the first insight about the main component of both systems. BB was considered phytoplankton dominated water while Nav was inorganic matter dominated water. Which means that the water along the cascade tends to have low primary production. The same happened with the IOPs, with decreasing trend in absorption coefficient from BB to Nav, also reflecting the improvement of trophic state.

$a_{\phi}(443)$ was correlated to Chl-*a* in BB1, BB2 and in Nav3, which means that environmental conditions changed the water quality in Nav3. The main cause of this was attributed to meteorological forcing during the periods of collection and according to Figure 2.3, a drought condition was installed from 2013 to 2015, leading to the limitation of rainfall rate. After that, in 2016, the rainfall conditions were recovered increasing the availability of nutrients and consequently, the increase of primary production. A feature between 550 to 650 nm was also enhanced in BB1, BB2 and Nav3 spectra being characteristic of phycobilipigments (phycocyanin).

$a_{CDOM}(443)$ was correlated to Chl-*a* in BB1 showing that most of CDOM was originated from the decomposition of phytoplankton, differently from Nav that did not show any correlation between both variables, indicating an allochthonous source of CDOM. BB

presented $a_\phi(443)$ values in accordance with productive inland waters, nonetheless, Nav showed values included in the same range reported for inland marine waters, illustrating the optical variability between both reservoirs. The a_ϕ^* from Nav and BB corroborated with the assumption that at 443 nm the trophic state of the water decrease from oligotrophic to hypereutrophic.

The $a_{NAP}(\lambda)$ did not show seasonal pattern between field campaigns and reservoirs and the S_{NAP} depicted low variability between BB and Nav with a slight increase at BB data. The increase trend found with the relationship of S_{NAP} and OSS highlighted the domain of organic matter in BB as suggested by Babin et al. (2003). The $a_p(\lambda)$ enhanced the previous findings about both reservoirs, that is, BB was highly influenced by phytoplankton pigments along the visible spectrum while Nav showed only the feature at 675 nm represented by Chl-*a* absorption and high contribution of NAP at the blue region. The implication of different biogeochemical and optical properties in two reservoirs on the same river can make it difficult to use a single model in order to estimate the OSCs. For that reason, new approaches based on analytical models should be useful for retrieving the optical water quality.

CHAPTER 4: RETRIEVAL OF INHERENT OPTICAL PROPERTIES FROM OLIGO-TO-MESOTROPHIC INLAND WATER USING THE QUASI-ANALYTICAL ALGORITHM

4.1 Introduction

Inland waters, represented by rivers, lakes and reservoirs, play a key role in hydrological cycle providing different habitats and ecosystem services (BRÖNMARK and HANSSON, 2002). As many other ecosystems, inland waters have increasingly been under anthropogenic or developmental pressure from industry, agriculture and urban activities increasing nutrient loading and other organic and inorganic pollution (PALMER et al., 2015). Infusion of nutrients (N and P) from the land via runoff often leads to eutrophication increasing the primary production of phytoplankton and macrophytes (PAERL et al., 2011). In oligo-to-mesotrophic reservoirs, the submersed species of macrophytes, which are usually rooted, occupy the edges and often the slow-moving zones of rivers. They are dependent on the sediments and light availability for their optimal growth (WELCH AND LINDELL, 1992). The clarity of the water is affected by turbidity generated from sediments or other suspended particles, algae and the natural color of the water. Frequent spatio-temporal monitoring of the physical, chemical and biological processes is of great importance to lake and reservoir management, however, the Tietê reservoirs, as well as many other Brazilian water bodies, are being affected by anthropogenic activities such as agriculture and expansion of urban centers. They are still being managed using traditional methods of *in situ* data collection with spatio-temporal limitation. The monitoring follows specific goals by selecting strategic locations. Therefore, accurate remote sensing models and techniques can be a powerful tool to complement conventional approaches in reservoirs monitoring (PALMER et al., 2015).

Yacobi et al. (2011), Odermatt et al. (2012) and Palmer et al. (2015) highlighted the main scientific contributions and challenges regarding the study of complex waters using remote sensing. The variability within this type of water, in terms of concentrations as well as the SIOP of Chl-*a*, TSS and CDOM can be difficult to separate. On the other hand, in open ocean, the concentrations of NAP and CDOM are directly correlated with phytoplankton. This means that in certain wavelengths, such as at the blue and green, it is possible to retrieve Chl-*a* concentration in open ocean but is not appropriate for inland waters, because CDOM and NAP have strong overlapping absorption particularly in the blue spectral region. To address this issue, many efforts have been made to understand the bio-optical properties of inland waters in order to retrieve the OSCs by using an inversion model based on empirical and analytical

approaches (MOREL, 1980; CARDER et al., 1999). In general, the inversion models first derive the IOPs using *in situ* measured AOP and then retrieve the OSC concentration (SHANMUGAM et al., 2010).

The empirical approach do not use the IOPs to retrieve water quality parameters, but a statistical relationship between an AOP, such as the remote sensing reflectance (R_{rs}) or the irradiance reflectance (R), and a known OSC (GOULD et al., 2001; SATHYENDRANATH et al., 2001; RITCHIE et al., 2003). The method is often time and site limited and according to Ogashawara (2015), it does not relate to any physical principle. The semi-analytical and quasi-analytical (QAA) algorithms are based on radiative transfer theory and often include some empirical steps (CARDER et al., 1999; DEKKER et al., 2002; BRANDO et al., 2012; ODERMATT et al., 2012). Semi-analytical algorithm estimates the total absorption coefficient, $a_t(\lambda)$, by the sum of the absorption coefficient of phytoplankton, a_ϕ, absorption coefficient of CDOM, a_{CDOM}, and absorption coefficient of NAP, a_{NAP}, while QAA estimates a_t just using R_{rs}. The semi-analytical model also estimates the backscattering coefficient, $b_b(\lambda)$, by summing the backscattering of each in-water constituent except for CDOM while the QAA retrieves $b_b(\lambda)$ according to Gordon and Morel (1983).

The original QAA by Lee et al. (2002) was initially developed to retrieve absorption and backscattering properties in open ocean and coastal waters and later re-parametrized for turbid inland waters (LE et al., 2009a; YANG et al., 2013; MISHRA et al., 2014). The model follows several steps mixing empirical and analytical approaches (Table 4.1) to derive the IOPs using radiative transfer equations, considering the reference wavelength (λ_0) at 555 nm (LEE et al., 2002). At this wavelength, the contribution of total suspended matter is very high in turbid eutrophic waters which requires λ_0 to be shifted to longer wavelengths such as 710 nm (LE et al., 2009a), 754 nm (YANG et al., 2013) and 708 nm (MISHRA et al., 2013; MISHRA et al., 2014). Lee et al. (2002) also showed the performance of QAA using 640 nm as reference wavelength and noticed considerable improvement in high-absorption environments with $a_t(440)$ higher than 0.3 m^{-1}, however, Le et al. (2009a) emphasized the importance of more validation to improve the performance of this approach. In mesotrophic inland waters, Yacobi et al. (2011) highlighted that at wavelengths longer than 600 nm, a_w increases over other OSCs, which means that at shorter wavelengths the contribution of other OSC but water is dominant decreasing the performance of QAA in this type of water.

The performance of QAAs in inland waters have been tested by various researchers; however, the sites considered were all highly turbid and eutrophic inland waters. For instance,

Le et al. (2009a) studied the turbid Taihu Lake with Chl-*a* concentration ranging between 3.07 – 299.60 µg l^{-1}, while Yang et al. (2013) studied three turbid Asian lakes with Chl-*a* varying between 9,790 – 153,920 µg l^{-1} and Mishra et al. (2014) explored the performance of QAA in aquaculture ponds dominated by cyanobacteria with Chl-*a* ranging between 960 – 1,380 mg m^{-3} and a_ϕ accounting for 54% of $a_t(443)$. The main modification carried out by these studies besides shifting λ_0 to the near-infrared (NIR), was in the estimation of the spectral slope of particle backscattering (η). These findings opened a new frontier of QAA application based on re-parameterizations for inland waters, however, still, there is a lack of research related to oligo-to-mesotrophic environments with Chl-*a* ranging between low to moderate and a_t not being dominated by phytoplankton but CDOM and NAP.

In order to understand the bio-optical properties of a non-productive tropical reservoir, this work aimed to re-parametrize and validate the QAA based on the band architecture of OLCI (Ocean and Land Colour Instrument) sensor onboard Sentinel-3 (launched in February 16, 2016). The specific objectives were: i) to identify a λ_0 where a_w is dominant; ii) to parameterize the empirical steps used in a_t derivation, such as the $a_t(\lambda_0)$ and η; iii) to calibrate ζ and ξ associated with a_ϕ and a_{CDOM}, respectively, and iv) to replace the original steps associated with a_ϕ estimation for oligo-to-mesotrophic waters and propose an alternative method in order to avoid negative predictions.

4.2 Data and methods

From all samples collected in the field, a total of 51 were used in this study for calibration (Nav 1: 1, 2, 3, 4, 6, 7, 8, 9, 10, 11, 12, 13, 14, 15, 16, 18, 19, 20), validation (Nav 2: 1, 2, 3, 4, 5, 6, 10, 12, 13, 15, 16, 18, 19, 20) and temporal comparison (Nav 3: 1, 2, 3, 4, 5, 6, 7, 8, 9, 10, 11, 12, 13, 14, 15, 16, 17, 18, 19) (see Figure 2.1 for sampling stations location).

4.2.1 Water quality parameters

Water samples were collected just below the air-water interface and then filtered on the same day of collection under vacuum pressure through a pre-ashed and pre-weighed Whatman fiberglass GF/F filter with a porosity of 0.7 µm, and then frozen (-25°C) for further TSS laboratory analysis. Chl-*a* was extracted with 90% acetone solution and analyzed spectrophotometrically (GOLTERMAN et al., 1978). The TSS concentration was determined by applying the method described by APHA (1998), in which the filters were dried in the oven

at 100° C for 12h, and then weighed using an analytical scale. To retrieve the ISS, the dried was subjected to a muffle furnace for 75 min at 550° C and weighed again. At the end, the TSS and inorganic fraction were determined and to estimate the OSS the last weighted filter was subtracted from the original filter weight after first drying.

4.2.2 *In-Situ* Radiometric Data

The R_{rs} spectra were estimated from radiometric measurements taken between 10 a.m. to 2 p.m. This procedure was carried out in order to maintain consistent acquisition geometry based on the time window of light availability (MOBLEY, 1999). At each sample station, below and above water readings were acquired using hyperspectral radiometers RAMSES TriOS® (TriOS, Germany) operating in the spectral range between 400 and 900 nm. The radiance sensor was equipped with a 7º field-of-view and the irradiance sensor with a cosine collector. Before being used, the radiometric quantities such as the total upwelling radiance ($L_t(\lambda)$; W m^{-2}sr^{-1}nm^{-1}), incident sky radiance ($L_s(\lambda)$; W m^{-2}sr^{-1}nm^{-1}) and downwelling irradiance incident onto the water surface ($E_d(\lambda)$; W m^{-2}nm^{-1}) were subjected to a linear interpolation to transform the original spectral resolution of ~ 3.3 nm to 1 nm. This procedure was designed to homogenize RAMSES measurements between the sensors, since they have different wavelength values.

The sampling rate was around 15 s per sample resulting in 16 readings at each sampling location. From these measurements, a median value was retrieved to represent the spectrum of that location. The acquisition geometry followed the protocol described by Mueller (2000) and Mobley (1999). Care was taken to avoid the effects of specular reflectance and boat shading the instruments were positioned on a steel frame and the L_t sensor was set with a viewing angle of 40º from nadir and an azimuth of 135º (oriented from the sun), and the L_s sensor was set with the same angles, 40º from zenith and 135º azimuth. $R_{rs}(\text{sr}^{-1})$ spectra were calculated from the radiometric profiles in accordance with Mobley (1999):

$$R_{rs}(\lambda) = \frac{L_t(\lambda) - \rho L_s(\lambda)}{E_d(\lambda)} \tag{4.1}$$

where ρ is the proportionality factor that considers the wind speed and sky radiance distribution. ρ was chosen as 0.028 since the average wind speed did not exceed 5 m s^{-1} during data collection and the geometry of acquisition was kept the same as Mobley (1999).

In situ R_{rs} is the main input data for QAA to retrieve OSC concentration. However, for broader applicability of a model, it is necessary to match the hyperspectral data with satellite data by using the spectral response functions of the sensor of choice. In this study, Ocean and Land Colour Instrument (OLCI - Sentinel-3 satellite) bands spectral response functions was convolved with *in situ* R_{rs} data to derive the band-weighted reflectance data (GORDON, 1995):

$$R_{rs}^{OLCI}(\lambda_k) = \frac{\int_{\lambda_i}^{\lambda_j} S(\lambda) R_{rs}(\lambda)}{\int_{\lambda_i}^{\lambda_j} S(\lambda)} \quad (4.2)$$

where R_{rs}^{OLCI} is the *in situ* R_{rs} matching the band width of OLCI sensor in Sentinel-3A satellite; λ_i and λ_j are the lower and upper limit of the band λ_k. *S*(λ) is the spectral response function of the *i*th spectral band of OLCI (PELLOQUIN and NIEKE, 2012).

4.2.3 *In Situ* Inherent Optical Properties

Water samples were filtered through a 0.7 μm porosity GF/F fiberglass that was stored flat under freezing condition. The determination of the total particulate (algal and non-algal) absorption (a_p) was performed by an integrating sphere module presented in the double-beam Shimadzu UV-2600 UV-Vis spectrophotometer (SHIMADZU, Japan), with spectral sampling from 280 nm to 800 nm. A white filter, wetted with ultrapure water was used as reference. The filter containing the particulate was positioned in the integrating sphere to measure their optical density (*OD*). The T-R (Transmittance-Reflectance) filter-pad technique presented by Tassan and Ferrari (1995, 2002) was employed to obtain a_p. To acquire the phytoplankton (a_ϕ) and detritus (a_d) absorption coefficients, the filter underwent pigmentation bleaching with 10% sodium hypochlorite (NaClO), ensuring that the samples do not contain any pigment interference. Using empirical relationships described by Tassan and Ferrari (1995, 2002), the respective coefficients were determined, and a_ϕ was obtained by the difference between the *OD* of the total particulate and detritus fractions.

To estimate the CDOM absorption coefficient (a_{CDOM}), water samples were filtered through a fiberglass Whatman GF/F with 0.7 μm pores, and then re-filtered under low vacuum pressure using a Whatman nylon membrane filter with 0.2 μm pores. The readings were performed using the absorbance mode, and the samples were placed in a 10 cm quartz cuvette. For each set of measurements, a reference reading was performed containing Milli-Q water,

and for each read sample (OD_{sample}), the reference absorbance value ($OD_{reference}$) was subtracted. The OD_{sample} was converted to absorption coefficient according to the equation (3.2):

A baseline correction was performed by subtracting the average value between 700 and 750 nm from all the spectrum values (BABIN et al., 2003). This procedure was used because CDOM absorption is negligible at this range and the temperature and salinity have a slight effect on water absorption (GREEN and BLOUGH, 1994). Due to the similarities in the absorption spectrum and the difficulty in separating a_{CDOM} and a_d fractions from their total absorption coefficient, many studies have treated both components as a single measure, such as the a_{CDM} comprised of the sum of a_{CDOM} and a_d (LEE et al., 1994; SHANMUGAM et al., 2011; ZHU et al., 2011). The spectral slope of a_{CDM} (S_{CDM}) is a constant obtained by the exponential fit within the 400 – 700 nm wavelength range (MISHRA et al., 2014).

4.2.4 QAA General Context

Following the first step from QAA, $a_t(\lambda)$ was retrieved based on several parameters described in Table 4.1. The success in determining $a_t(\lambda)$ is of great importance in estimations of $b_b(\lambda)$ and the OSC absorption coefficients (CDM and phytoplankton). The partitioning of $a_t(\lambda)$ into $a_{CDM}(\lambda)$ followed the same flow proposed by Lee et al. (2002), however, to derive $a_\phi(\lambda)$ an alternative step (see section "Re-parametrization of QAA to derive a_ϕ") was needed, to avoid negative values due to low $a_\phi(\lambda)$ signal in Nav.

Three existing models were used to test their performances using Nav's dataset convoluted to OLCI bands: the models proposed by Lee et al. (2009, 2014) referred to as QAA_{Lv5} and QAA_{Lv6} for versions 5 (λ_0 = 560 nm) and 6 (λ_0 = 665 nm) available at the International Ocean Colour Coordinating Group (IOCCG) website (URL: http://www.ioccg.org/groups/software.html). The third model was based on Mishra et al. (2014) referred to as QAA_{M14} (λ_0 = 709 nm). The performance of the new re-parametrized model developed in this study (QAA_{OMR}), was also compared with the three existing models.

Table 4.1. QAA steps comparing the version 5 from Lee et al. (2002) and the QAA_{OMR} proposed in this study.

QAA_{Lv5}	**QAA_{OMR}**
$r_{rs}(\lambda) = R_{rs}(\lambda)/(0.52 + 1.7R_{rs}(\lambda))$	
$u(\lambda) = \frac{-0.0895 + \sqrt{(g_0)^2 + 4g_1 * r_{rs}(\lambda)}}{2 * g_1}; g_0 = 0.089, g_1 = 0.125$	

$\chi = \log\left(\frac{r_{rs}(443) + r_{rs}(490)}{r_{rs}(\lambda_0) + 5\frac{(r_{rs}(667))^2}{r_{rs}(490)}}\right)$	$\chi = \log\left(\frac{r_{rs}(443) + r_{rs}(665)}{r_{rs}(\lambda_0) + 5\frac{(r_{rs}(681))^2}{r_{rs}(443)}}\right)$
$a_t(\lambda_0) = a_w(\lambda_0) + 10^{-1.146-1.366\chi-0.469\chi^2}$ where $\lambda_0 = 550;\ 555; 560$	$a_t(\lambda_0) = a_w(\lambda_0) + 10^{-1.148+2.814\chi-5.813\chi^2}$ where $\lambda_0 = 709$
$\eta = 2 \times \left(1 - 1.2 \times \exp\left(-0.9 \times \frac{r_{rs}443}{r_{rs}(\lambda_0)}\right)\right)$	$\eta = 2 \times \left(1 - 1.2 \times \exp\left(-0.9 \times \frac{r_{rs}665}{r_{rs}754}\right)\right)$
$\zeta = 0.74 + \left(\frac{0.2}{0.8 + r_{rs}443/r_{rs}\lambda_0}\right)$	$\zeta = 0.5 + \left(\frac{0.2}{0.8 + r_{rs}443/r_{rs}\lambda_0}\right)$
$\xi = \exp[S \times (443 - 412)]$	$\xi = \exp[S \times (443 - 412)]$
$S_{CDM} = 0.015 + \left(\frac{0.002}{0.6 + (r_{rs}443/r_{rs}\lambda_0)}\right)$	$S_{CDM} = 0.0095 + \left(\frac{0.002}{0.6 + (r_{rs}490/r_{rs}\lambda_0)}\right)$
$a_{CDM}(443) = \frac{[a_t(412) - \zeta a_t(443)] - [a_w(412) - \zeta a_w(443)]}{\xi - \zeta}$	$a_{CDM}(443) = \frac{[a_t(412) - \zeta a_t(443)] - [a_w(412) - \zeta a_w(412)]}{\xi - \zeta}$
$a_{CDM}(\lambda) = a_{CDM}(443)e^{-S_{CDM}(\lambda-443)}$	$a_{CDM}(\lambda) = a_{CDM}(443)e^{-S_{CDM}(\lambda-443)}$
—	$a_\phi(443) = \frac{[\xi a_t(443) - a_t(412)] - [\xi a_w(412) - a_w(412)]}{\xi - \zeta}$
	$a_\phi(\lambda) = a_{ph}(443) \times a_\phi^+(\lambda)$
$a_\phi(\lambda) = a_t(\lambda) - a_{CDM}(\lambda) - a_w(\lambda)$	where $a_\phi^+(\lambda) = a_\phi(\lambda)/\frac{\int a_x(\lambda)d\lambda}{\lambda_{max}-\lambda_{min}}$

4.2.5 Re-parametrization /Validation and Accuracy Assessment

The three QAA versions described in the previous section were tested using Nav's dataset. For this step, water samples collected in the first field trip were analyzed in laboratory by filter-pad technique to retrieve a_t, a_{CDM} and a_ϕ including $a_w(\lambda)$ from Pope and Fry (1997) combined to obtain $a_t(\lambda)$. The re-parametrization steps in QAA_{OMR} primarily involved modifying the intermediary steps such as computation of χ, $a_t(\lambda_0)$ and η for a_t estimation (see Table 4.1). After that, the decomposition of a_t into a_{CDM} and a_ϕ was also evaluated by comparing with *in situ* measures. In order to validate the newly parametrized model related to oligo-to-mesotrophic waters, the samples collected in the second field trip were used.

The statistical indicators used for validation were the total root mean square difference (RMSD), *bias*, the mean absolute percentage error (MAPE) and to provide a broader statistical overview of the error, the normalized *bias* (*B**), normalized standard deviation (σ*), linear correlation (*R*) and normalized unbiased RMSD (*uRMSD**) were also applied. The term normalized stands for all statistical metrics divided by the standard deviation of the reference and here named as σ_{meas}, while the term unbiased, emphasize that the measure removes any information about the potential *bias*. σ* and *R* represent the magnitude of data dispersion and

shape patterns. To obtain the ideal situation, magnitude and shape may consider that $\sigma^* = R = 1$, which leads to the minimum *uRMSD**.

A different perspective about the contribution of the error was achieved using the Taylor and Target graphics (TAYLOR, 2001; JOLLIFF et al., 2009). In the polar coordinate diagram (Taylor graphic), the radial (along-axis) distance from the origin is related to σ^* and the angular position corresponds to *R*. The distance between the reference and the modeled points are proportional to *uRMSD**. The observation is the reference point, which is indicated by the polar coordinates (1.0, 1.0) when we consider that the metrics are normalized. The target diagram considers the Cartesian plane (*uRMSD*, B**) where *uRMSD** > 0 means that the model standard deviation is larger than the reference, whilst *uRMSD** < 0 indicates the contrary. *B* >0* signifies positive *bias* while *B* < 0* negative. The quantities may be normalized to remove the units. The Taylor graphic can be displayed in 90° or as presented here in 180° covering negative correlations. Values of σ^* higher than 2.0 were not depicted while *B** and *uRMSD** higher than 3 and/or less than -3 were also disregarded in the Target diagrams. This condition was used to avoid presenting huge error models.

The error indices are defined according to Equations (4.3) to (4.8):

$$RMSD = \sqrt{\frac{1}{n}\sum_{i=1}^{n}\left(x_{est,i} - x_{meas,i}\right)^2} \tag{4.3}$$

$$MAPE = \frac{100\%}{n}\sum_{i=1}^{n}\left|\frac{x_{est,i} - x_{meas,i}}{x_{meas,i}}\right| \tag{4.4}$$

$$B^* = \left(\frac{\bar{x}_{est} - \bar{x}_{meas}}{\sigma_{meas}}\right) \tag{4.5}$$

$$\sigma^* = \frac{\sigma_{est}}{\sigma_{meas}} \tag{4.6}$$

$$R = \frac{\frac{1}{n}\sum_{i=1}^{n}(x_{est,i} - \bar{x}_{est})(x_{meas,i} - \bar{x}_{meas})}{\sigma_{meas}\sigma_{est}} \tag{4.7}$$

$$uRMSD^* = sign(\sigma_{est} - \sigma_{meas})\sqrt{1 + \sigma^{*2} - 2\sigma^* R} \tag{4.8}$$

where *n* is the number of samples, $x_{est,i}$ and $x_{meas,i}$ are represent the estimated and measured values, respectively. $\bar{x}_{est}$ and $\bar{x}_{meas}$ represent the average of estimated and measured values, respectively. σ_{meas} and σ_{est} are the standard deviation of the measured and the estimated values, respectively.

4.3 Results and Discussion

4.3.1 Biogeochemical characterization

Samples collected during the first field trip showed very low concentrations of Chl-*a* (average of 5.95 µg l^{-1}) and TSS (average of 0.63 mg l^{-1}) and average Secchi Disk Depth of 3.22 m (Table 4.2). The OSC concentration in the samples collected during the second field trip showed a modest increase with Chl-*a* (average of 7.94 µg l^{-1}) and TSS (average of 1.58 mg l^{-1}) and average Secchi Disk Depth of 3.14 m. *In situ* collected $a_t(443)$ represented non-productive waters with values ranging between 0.72 – 1.52 m^{-1} from the first field trip and 0.58 – 1.45 m^{-1} from the second field trip. Lee et al. (2002) recommended their open ocean version of QAA to be applied for datasets where $a_t(443)$ is less than 0.3 m^{-1} and in NAV the $a_t(443)$ was higher than this threshold, therefore a poor performance was expected from the native QAA approach.

Table 4.2. Descriptive statistic of the water quality variables used for calibration and validation. SD: standard deviation, CV: coefficient of variation and n is the number of samples.

	Average	**SD**	**Minimum**	**Maximum**	***CV (%)***	***n***
Nav1: April – May 2014						
$a_t(443)$ (m^{-1})	1.18	0.16	0.72	1.52	13.56	18
$a_\phi(443)$ (m^{-1})	0.31	0.08	0.19	0.50	25.81	18
$a_\phi(560)$ (m^{-1})	0.08	0.03	0.04	0.14	37.50	18
$a_\phi(665)$ (m^{-1})	0.15	0.04	0.09	0.24	26.67	18
$a_{NAP}(443)$ (m^{-1})	0.62	0.11	0.25	0.76	17.74	18
$a_{CDM}(443)$ (m^{-1})	0.87	0.12	0.51	1.02	13.79	18
TSS (mg l^{-1})	0.63	0.54	0.10	2.15	85.71	15
Chl-*a* (µg l^{-1})	5.95	2.11	2.46	10.65	35.46	18
Chl-*a* : TSS (µg/mg)	12.27	15.97	2.47	68.26	130.14	15
Depth (m)	17.81	8.64	5.30	30.00	48.51	18
Secchi Depth (m)	3.22	0.62	2.29	4.80	19.25	18
Turbidity (NTU)	1.60	0.41	1.01	2.47	25.35	18
Nav2: September 2014						
$a_t(443)$ (m^{-1})	0.88	0.20	0.58	1.45	22.73	14
$a_\phi(443)$ (m^{-1})	0.27	0.09	0.10	0.43	33.33	14
$a_\phi(560)$ (m^{-1})	0.04	0.03	0.01	0.12	75.00	14
$a_\phi(665)$ (m^{-1})	0.09	0.03	0.02	0.16	33.33	14
$a_{NAP}(443)$ (m^{-1})	0.28	0.15	0.13	0.75	53.57	14
$a_{CDM}(443)$ (m^{-1})	0.60	0.16	0.43	1.04	26.67	14
TSS (mg l^{-1})	1.58	2.37	0.50	10.00	150.00	14

Chl-*a* (µg l^{-1})	7.94	3.45	3.41	16.38	43.45	14
Chl-*a* : TSS (µg/mg)	9.15	4.75	0.34	18.57	51.95	14
Depth (m)	21.56	5.27	12.00	28.00	24.44	14
Secchi Depth (m)	3.14	0.86	0.90	4.65	27.39	14
Turbidity (NTU)	2.44	2.46	1.01	11.17	100.97	14
Nav3: May 2016						
$a_t(443)$ (m^{-1})	0.99	0.18	0.65	1.37	17.84	19
$a_\phi(443)$ (m^{-1})	0.30	0.13	0.11	0.57	43.47	19
$a_\phi(560)$ (m^{-1})	0.06	0.05	0.00	0.15	76.24	19
$a_\phi(665)$ (m^{-1})	0.15	0.06	0.09	0.26	38.57	19
$a_{NAP}(443)$ (m^{-1})	0.61	0.12	0.38	0.82	19.65	19
$a_{CDM}(443)$ (m^{-1})	0.68	0.12	0.45	0.91	17.68	19
TSS (mg l^{-1})	3.08	1.00	1.87	5.30	32.35	10
Chl-*a* (µg l^{-1})	26.36	6.66	38.59	15.84	25.28	10
Chl-*a* : TSS (µg/mg)	8.93	2.07	4.64	12.21	23.14	10
Depth (m)						-
Secchi Depth (m)	2.97	0.63	1.91	3.80	21.03	19
Turbidity (NTU)						-

The low turbidity caused by the low Chl-*a* and TSS concentrations provided more transparency to the water column and hence high Secchi Depth measures. The water transparency is negatively correlated with rainfall and according to Table 4.2 the Secchi Depth range changed from 2.29 – 4.80 m during the beginning of the dry season to 0.90 – 4.65 m at the end of the dry season (RIBEIRO FILHO et al., 2011). Smith et al. (2014) highlighted that the high concentrations of suspended matter during rainy season in Nav can be attributed to the runoff effect. Slight differences in limnological parameters from one field trip to another was observed and as stated by Smith et al. (2014), factors such as water level fluctuation and seasonality are of great importance for the changes in geochemical dynamics of the reservoir. The relationship (not shown here) between Chl-*a* and TSS concentrations during the first (R^2 = 0.12, $p > 0.05$, $n = 18$) and second ($R^2 = 0.07$, $p > 0.05$, $n = 14$) field campaigns indicated the non-productive property of Nav, which was mostly dominated by inorganic matter.

4.3.2 Bio-optical characterization

The reciprocal of remote sensing reflectance (R_{rs}^{-1}, Figure 4.1) is considered a proxy for absorption (GORDON et al., 1975) by corresponding OSCs in the water body. The main features in the R_{rs} spectra acquired during both field trips were related to dissolved and particulate matter absorption at shorter wavelengths. At longer wavelengths such as at ~560 nm

the low magnitude was due to the weak absorption by pigments and scattering from phytoplankton cells (ROESLER et al., 1989; GITELSON, 1992; CHENG et al., 2013). Strong absorption from 600 nm onwards followed a shape similar to a_w (red line) inferring that beyond 600 nm the contribution of others OSCs was minor in both datasets. In addition, the red absorption features were also related to Chl-*a* at 675 nm (GITELSON, 1992).

Figure 4.1. Reciprocal remote sensing reflectance (R_{rs}^{-1}) data from the (a) first, (b) second and (c) third field trips. Pure water absorption (a_w) (red line) is shown for reference.

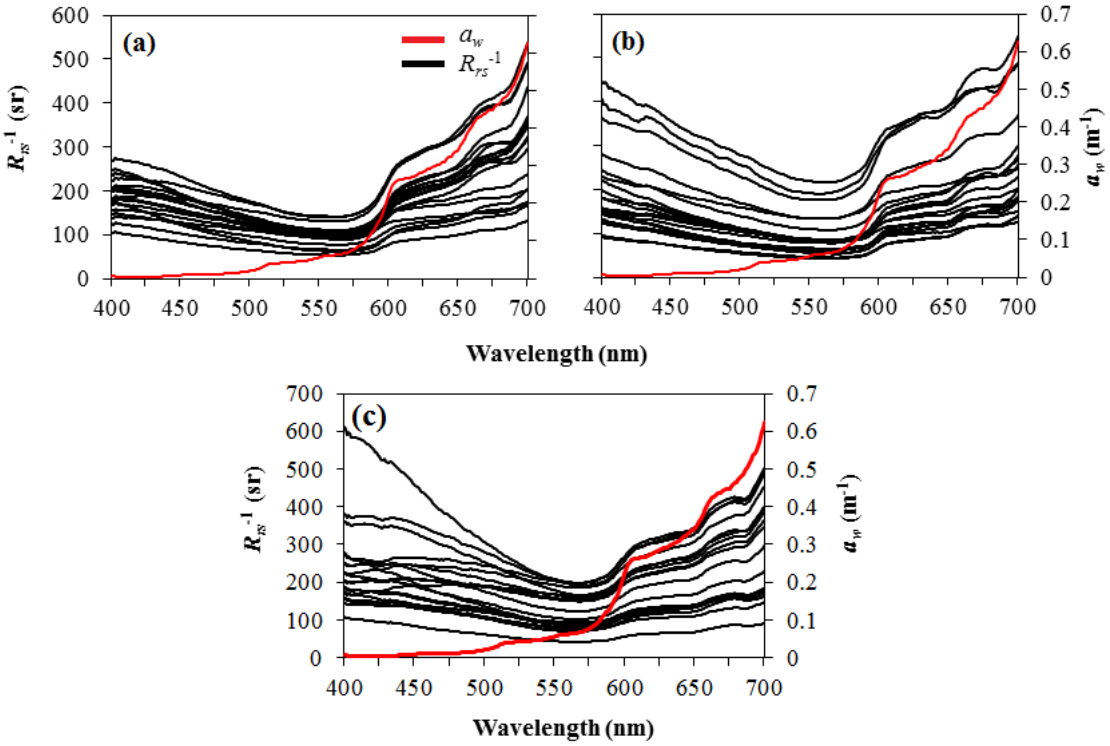

The blue spectral region in Nav's dataset did not present any prominent feature of absorption related to phytoplankton pigments, on the contrary, it remained flat up to 560 nm. The same pattern was also noticed in another oligo-to-mesotrophic reservoir in Brazil (OGASHAWARA et al., 2014). This feature was documented by Doxaran et al. (2002) who reported the increase of R_{rs} between 550 and 850 nm with increasing TSS concentration.

4.3.3 OSC relative contribution

The relative contribution of phytoplankton, CDOM and detritus absorption to the total absorption budget without the water fraction (a_{t-w}) can be visualized in Figure 4.2. The wavelengths chosen for analysis (443, 560 and 665 nm) characterize the light interaction with

particulate and dissolved organic matter (LE et al., 2013; ZHANG et al., 2009b; LOOS, 2010). According to the ternary plots, the first set of field data were dominated by a_d, mainly in the blue (443 nm) and green (560 nm) wavelengths with 52.05 ± 6.37 % and 56.78 ± 8.80 % respectively. a_ϕ dominated in the red (655 nm) wavelength with 59.87 ± 8.34 % contribution towards a_{t-w}. The contribution of the OSCs was a little more balanced in the second field dataset. At 443 nm, the a_{CDOM} contributed with 37.22 ± 9.18 % while at 560 nm, the a_d accounted for 47.13 ± 10.44 % and a_ϕ for 40.17 ± 12.38 % at 665 nm. At 443 nm, the samples from the second fieldtrip were spread within the central zone of the ternary plot indicating that all three absorption coefficients co-varied somehow.

Figure 4.2. Ternary plots displaying the relative contribution of CDOM, phytoplankton and detritus to the total absorption at different wavelengths, (a) 443 nm, (b) 560 nm, (c) 665 nm and (d) the relative contribution of water, particulate and CDOM to absorption at 709 nm.

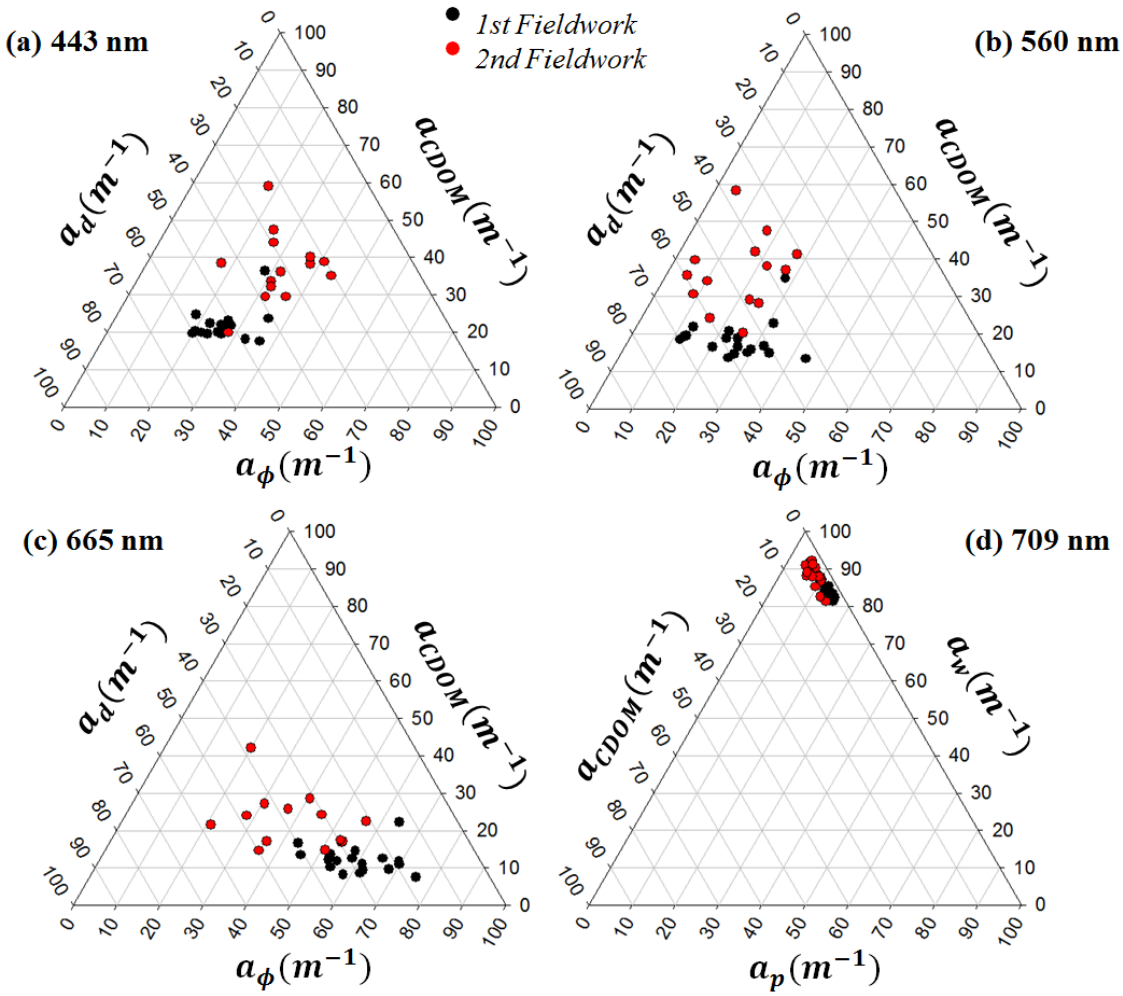

As expected, the ternary plot showed the predominance of a_ϕ at 665 nm to (a_{t-w}) from both datasets with a slight dominance in the first field dataset. a_d dominated the absorption at 560 nm and at 443 nm the absorption was mainly governed by a_d in the first and a_{CDOM} in the second dataset. Since the QAA approach combines the absorption by CDOM and detritus, it can be considered that IOPs data in Nav were dominated by a_{CDM} in the blue-green region and a_ϕ had a moderate contribution in the red region. The QAA_{Lv5} was developed using case-1 waters where a_t at 440 nm was less than 0.3 m^{-1}, while QAA_{M14}, was developed using data from very turbid productive waters, where the average $a_t(443)$ was 19.9 m^{-1} and 13.5 m^{-1}, in July and April, respectively. According to Qin et al. (2007), the accuracy of QAA for ocean waters generally degrades rapidly with increasing CDOM and non-algal particle (NAP) concentrations. Li et al. (2016) used QAA with λ_0 shifted to longer wavelengths and found that if the average contribution of $a_{CDOM}(443)$ dominates the absorption budget, then QAA can achieve better result in turbid inland waters, however, the higher contribution of $a_p(443)$ leads to the poorer prediction results. The datasets used in previous QAAs did not fit the bio-optical properties of the current dataset with $a_t(443)$ ranging between 0.72 – 1.52 m^{-1}, which called for a re-parametrization.

4.3.4 Performance of existing QAA

The first step was to test the performance of the existing QAAs: QAA_{Lv5}, QAA_{Lv6}, and QAA_{M14}. We noticed that shifting the wavelength from 560 to 708 nm, the $a_t(\lambda)$ retrieval improved (Figure 4.3). QAA_{Lv5} and QAA_{Lv6} consistently underestimated a_t at all wavelength, while QAA_{M14} showed some improvement, particularly at longer wavelengths. The underestimation can be attributed to the inefficiency of the model at λ_0 (560 and 665 nm, respectively) and also due to the contribution of other OSCs such as suspended matter to the absorption budget. The ternary plot (Figure 4.2d) showed that a_w contributed approximately with 87 % to the absorption budget at 709 nm, which means that a_{CDOM}, a_d and a_ϕ together contributed with 13 % to a_t. QAA_{M14} showed more consistency when compared with measured a_t; however, since it was developed for a highly productive environment, the coefficients and band combinations were not suitable to describe the particularities of non-productive waters such as Nav. Therefore, the re-parametrization of the model was needed and initially based on QAA_{M14} using 709 nm as λ_0 and then followed the steps proposed by QAA_{Lv5}.

Figure 4.3. Relationship between estimated and measured $a_t(\lambda)$ using existing QAAs: (a) QAA_{Lv5}, (b) QAA_{Lv6} and (c) QAA_{M14}. The colored circles represents the band centers of OLCI sensor.

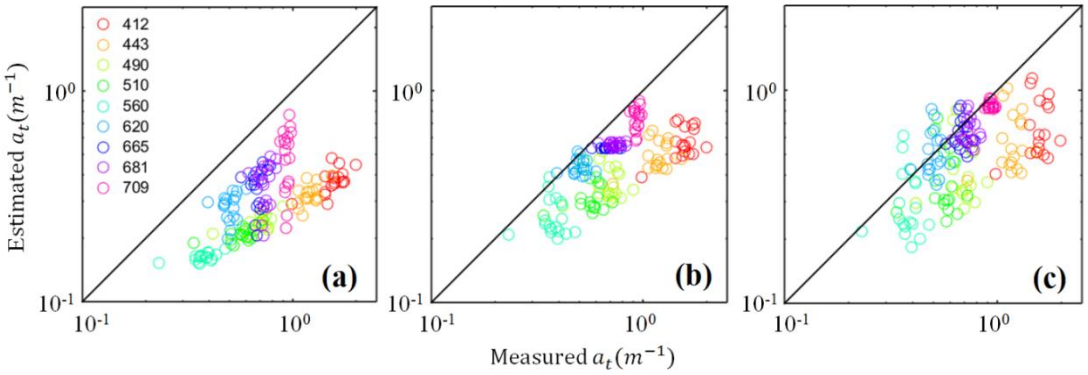

4.3.5 Re-parametrization of QAA to derive a_t

As discussed in previous sections (Figure 4.3), λ_0 plays a critical role in a_t retrieval and bands in NIR region should be considered for λ_0 selection even in an oligo-to-mesotrophic environment with very low Chl-*a* and TSS concentrations. In Nav, both OSCs did not co-vary among themselves which is different from case-1 waters and that could be the reason why QAA_{Lv5} or QAA_{Lv6} did not perform satisfactorily. The set of steps described by Lee et al. (2002) to derive a_t is comprised of empirical, semi-analytical and analytical approaches and was also modified to parametrize the current model. The absorption at 709 nm, $a_t(709)$, was chosen as λ_0 to derive χ in the empirical model which combines four bands associated with the OSCs contribution. To parametrize this variable, the relationship between $a_{t-w}(709)$ and OLCI bands was verified and the best combination was chosen based on the coefficient of determination (R^2) using bands at 443, 665 and 681 nm ($R^2 = 0.52$, $p < 0.001$) (Equation 4.9).

$$\chi = \log_{10}\left(\frac{r_{rs}443 + r_{rs}665}{r_{rs}(\lambda_0) + \left(0.05 \times \frac{r_{rs}681^2}{r_{rs}443}\right)}\right) \quad (4.9)$$

The band combination used to derive χ was same as Mishra et al. (2014). The band at 443 nm was used to highlight the contribution of CDOM and despite being the spectral region of Chl-*a* absorption as well (GITELSON, 1992). According to Mishra et al. (2014) these bands reflects differential contribution of OSCs typically present in inland waters to the total absorption budget, and therefore, the band combinations used in QAA_{M14} worked well for Nav.

The estimation of a_t is analytically related to $b_b(\lambda)$. Considering that $b_b(\lambda)$ is the sum of b_{bw} and b_{bp} and the value of b_{bw} is already known, the spectral dependency of $b_{bp}(\lambda)$ is widely expressed as Smith and Baker (1981) and Sathyendranath et al. (2001):

$$b_{bp}(\lambda) = b_{bp}(\lambda_0)\left(\frac{\lambda_0}{\lambda}\right)^{\eta} \tag{4.10}$$

$$b_b(\lambda) = b_{bp}(\lambda) + b_{bw}(\lambda) \tag{4.11}$$

where $b_{bw}(\lambda)$ is the pure water backscattering coefficient from Smith and Baker (1981), $b_{bp}(\lambda_0)$ is the particulate backscattering coefficient at the reference wavelength and can be estimated using Lee et al. (2002), η is the spectral power factor for particulate backscattering coefficient and can be empirically retrieved using r_{rs} band ratio sensitive to phytoplankton and CDOM absorption (CARDER et al., 1999). To model η, Lee et al. (2002) used an empirical band ratio between 440 and 550 nm, while Yang et al. (2013) used a semi-analytical model based on bands 750 and 780 nm from MERIS. The former authors observed that shifting the λ_0 to longer wavelengths is not enough to produce accurate IOPs, but improving η retrieval is also significant. Thus, the calibration of η was performed by comparing *in situ* a_t with derived a_t. Several band combinations were tested and the best result was achieved with the ratio of 665 over 754 nm as shown below:

$$\eta = 2 \times \left(1 - 1.2 \times \exp\left(-0.9 \times \frac{r_{rs}665}{r_{rs}754}\right)\right) \tag{4.12}$$

The values of η typically ranged from 0 to 2.2 and the higher values are associated mainly with oligotrophic waters (SATHYENDRANATH et al., 2001, LEE et al., 2002, ZAWADA et al., 2007). η ranged from 1.24 to 2.17 in Nav. Gordon and Morel (1983) concluded that η is higher when the backscattering is due to small particles and/or water. After b_b retrieval, the derivation of a_t followed the equation that relates the ratio of b_b to the sum of absorption and backscattering coefficients (u) as defined in Gordon et al. (1988) and expressed as:

$$a_t(\lambda) = \frac{[1 - u(\lambda)]b_b(\lambda)}{u(\lambda)} \tag{4.13}$$

After re-parametrization, the estimation accuracy of a_t improved significantly with a MAPE = 16.35% and RMSD = 0.15 m^{-1} (Figure 4.4a). The errors were considerably lower compared to existing QAAs such as QAA_{Lv5} (MAPE = 58.05% and RMSD = 0.51 m^{-1}), QAA_{Lv6} (MAPE = 35.59% and RMSD = 0.35 m^{-1}), and QAA_{M14} (MAPE = 30.98% and RMSD = 0.31 m^{-1}). The improvement was not consistent across all OLCI bands, particularly at 620 nm, which exhibited the second highest error among all tested versions (Table 4.3). However, this may not be a problem for oligo-to-mesotrophic waters where phycocyanin concentration is negligible. This could be an issue for waters dominated by cyanobacteria such as highly productive inland lakes and ponds.

Figure 4.4. Scatter plot between measured and estimated (a) $a_t(\lambda)$, (b) $a_{CDM}(\lambda)$ and (c) $a_\phi(\lambda)$ at OLCI spectral bands.

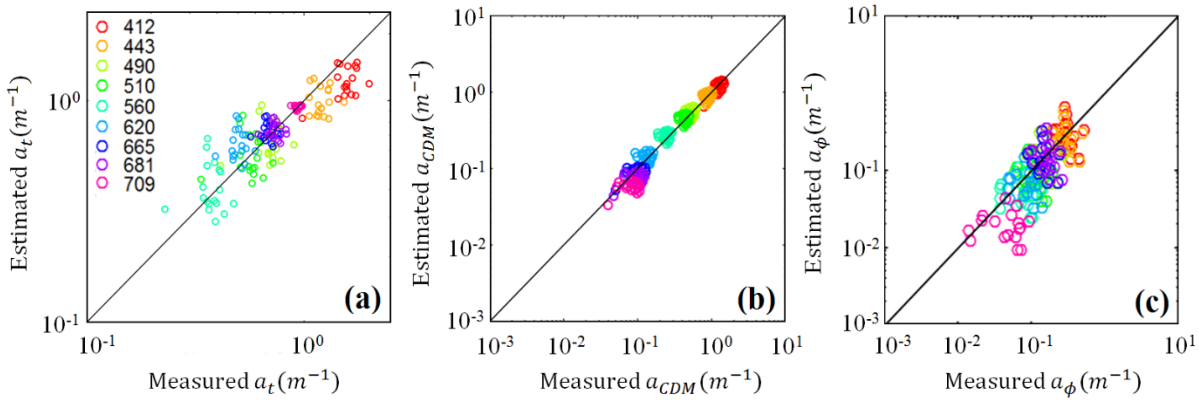

Table 4.3. Comparative band-specific errors related to the re-parametrization of $a_t(\lambda)$ based on MAPE (%) and RSMD (m^{-1}) metrics.

	QAA_{Lv5}		QAA_{Lv6}		QAA_{M14}		QAA_{OMR}	
Bands (nm)	**RMSD (m^{-1})**	**MAPE (%)**	**RMSD (m^{-1})**	**MAPE (%)**	**RMSD (m^{-1})**	**MAPE (%)**	**RMSD (m^{-1})**	**MAPE (%)**
412	1.21	75.88	1.01	63.01	0.93	56.21	0.35	19.74
443	0.87	72.52	0.71	57.55	0.64	49.64	0.23	16.02
490	0.47	65.93	0.35	46.66	0.32	41.04	0.14	16.78
510	0.37	62.96	0.26	41.76	0.24	38.12	0.13	19.02
560	0.22	56.39	0.14	31.83	0.15	32.99	0.12	24.33
620	0.23	43.32	0.08	13.35	0.13	20.92	0.17	29.05
665	0.34	48.56	0.16	21.48	0.13	15.30	0.09	11.17
681	0.38	50.26	0.19	24.31	0.14	15.55	0.07	8.29
709	0.46	46.63	0.21	20.39	0.09	9.04	0.03	2.70
Average	**0.51**	**58.05**	**0.35**	**35.59**	**0.31**	**30.98**	**0.15**	**16.35**

The Taylor diagram was used to understand how good model simulations were compared to observations. As shown in Figure 4.5a, the distance between the red data symbol

(reference) on the *x*-axis and each colored model symbol represents the *uRMSD**. For the four models, the *R* was very different, ranging between 0.09 (QAA_{M14}) to 0.63 (QAA_{Lv5}). Among all tested models at 443 nm, QAA_{Lv5} produced the lowest σ^* (0.26) which means that $a_t(443)$ derived using the model was far from the reference (1.00 – 0.26 = 0.74 units), and highest *R* (0.63) in comparison with the reference. As stated in Jolliff et al. (2009), for an *R* value of 0.63, the minimum *uRMSD** should occur where σ^* = 0.63, however, if the goal is to move *R* and σ^* closer to an ideal value of 1.0, then *uRMSD** is not a suitable validation metric. If we want to reduce the variability of both measured and estimated values, then $\sigma^* < 1.0$, thus, QAA_{Lv5} presented the best performance, however, if we intend to bring the model patterns to the ideal value of the reference, then QAA_{OMR} presented the best combination of *R* and σ^* (*R* = 0.54, σ^* = 0.96) as compared to the reference. In order to support the choice of the model, the target function was also used. At 443 nm (Figure 4.5b), QAA_{OMR} was the only model which showed the lowest *B** (-1.07) and all of them underestimated the variance of $a_t(443)$. QAA_{Lv5} retrieved the highest *B** (-5.43) emphasizing the bad performance of this model when compared to QAA_{OMR}. The other models did not appear because they presented *B** out of the range bounded by the interval of -3 and 3. Models positioned at the positive side of *uRMSD** means that $\sigma_{est} > \sigma_{meas}$.

At 560 nm (Figure 4.5c), QAA_{Lv5} was the only model that produced *R* > 0.50 and σ^* = 0.14, therefore the *uRMSD** was minimum relative to other studied models, however, *B** achieved again the highest value (-4.47) showing the underestimation pattern of this approach in retrieving $a_t(560)$. Both QAA_{Lv6} and QAA_{M14} also underestimated $a_t(560)$. QAA_{OMR} produced high value for σ^* (2.12) and low value for *R* (0.03) showing the high variability between measured and estimated values, however, *B** was the lowest (0.84) compared to other models (Figure 4.5d). Models not displayed in the Target graphic presented values outside the established range. Figure 4.5e showed that QAA_{OMR} was the only model that retrieved at least one error metric close to the reference (σ^* = 1.34) at 665 nm. According to Figure 4.5f, QAA_{OMR} overestimated $a_t(665)$ while QAA_{M14} (*B** = -1,32) showed underestimation as well as QAA_{Lv5} (*B** = -7.10) and QAA_{Lv6} (*B** = -3.18). Overall, the error analysis showed a significant improvement by the newly re-parametrized model mainly in the shorter and longer wavelengths (Table 4.3). The Taylor diagrams showed that the variability of $a_t(\lambda)$ estimated by the QAA_{Lv5} showed a closer variation of the reference data, however, the underestimation was reasonably high becoming unviable its use for $a_t(\lambda)$ retrieval.

Figure 4.5. Taylor diagrams for $a_t(\lambda)$ at (a) 443 nm, (c) 560 nm, (e) 665 nm. Target diagrams for $a_t(\lambda)$ at (b) 443 nm, (d) 560 nm and (f) 665 nm. Color symbols indicate the following: QAA_{Lv5} (grey dot), QAA_{Lv6} (yellow dot), QAA_{M14} (blue dot) and the QAA_{OMR} (green dot), reference observation (red dot). The black circle in the Target diagrams (M_0) corresponds to a normalized total RMSD of 1.0, so all points between this circle and the origin are positively correlated.

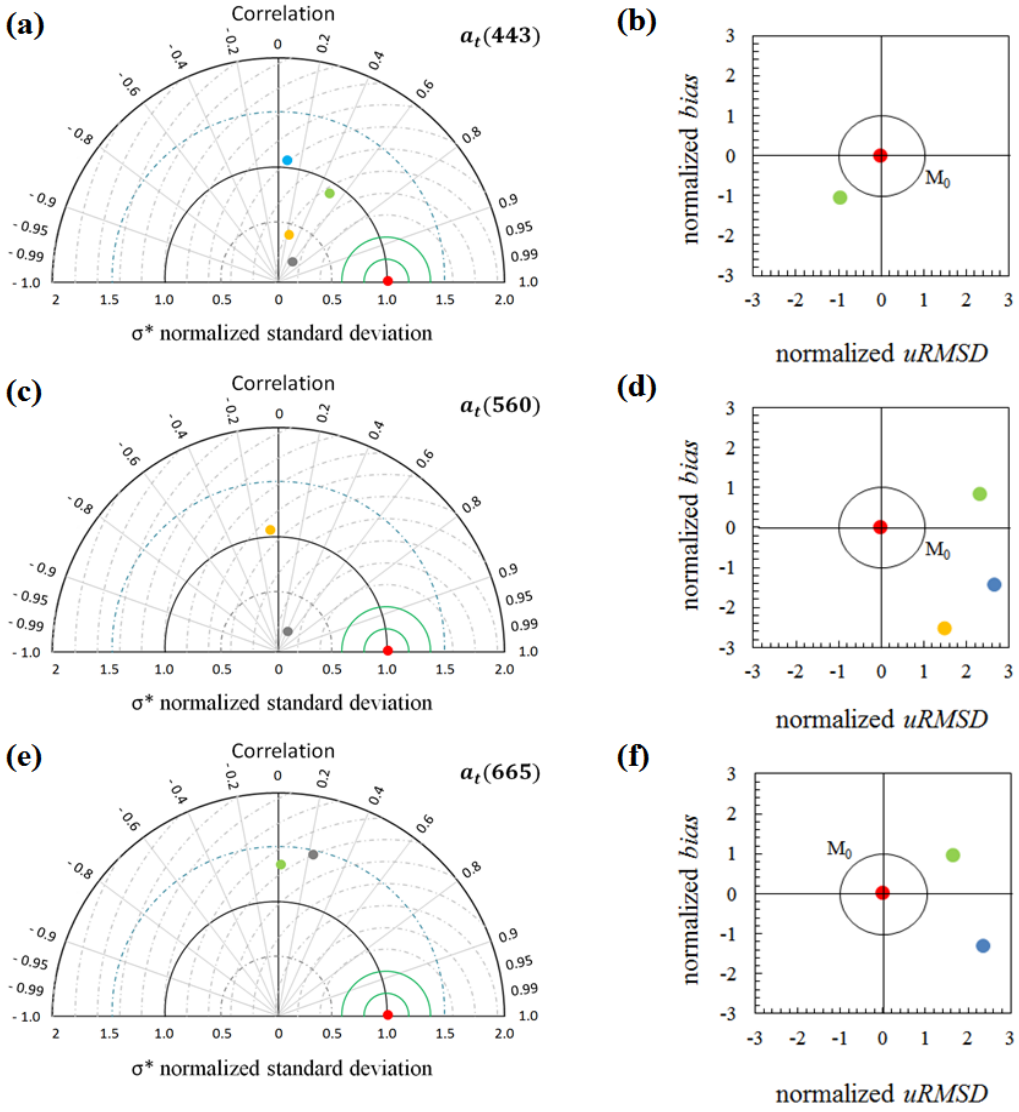

4.3.6 Re-parametrization of QAA to derive a_{CDM}

The re-parametrization involved improvements to derive CDM spectral slope (S_{CDM}) and the parameters ξ and ζ. ζ is related to Chl-*a* concentration or pigment absorption at a specific wavelength, but according to Lee et al. (2002), due to the lack of absolute measurements, ζ was empirically estimated using a blue-to-green band ratio of $r_{rs}(440)/r_{rs}(555)$ and successfully applied in case-1 waters (GORDON and MOREL, 1983, LEE et al.

1998). However, at this spectral region, the organic and inorganic suspended matters also affect the absorption budget (DOERFFER, 1994, CARDER et al., 1999). Yang et al. (2013) used another approach to estimate $a_\phi(443)$ independently of ξ and ζ with an assumption that the applicability of these empirical estimations was unclear for turbid waters. On the contrary, Mishra et al. (2014) maintained the original band ratio, but the coefficients used in ζestimation were changed. A new band ratio was proposed in this study by taking into account the local information and as recommended by Lee et al. (2002), this procedure is needed to improve the split-up of pigment and CDOM absorption fractions. After recalibration, the suitable band ratio between 443 and 709 nm ($r_{rs}(443)/r_{rs}(709)$) was applied to Nav dataset. Besides, the offset coefficient was also recalibrated by testing values ranging between 0.5 – 0.74 and followed the form:

$$\zeta = 0.5 + \left(\frac{0.2}{0.8 + r_{rs}443/r_{rs}\lambda_0}\right) \tag{4.14}$$

ξ approximated using a ratio, $a_{CDM}(410)/a_{CDM}(440)$, and S_{CDM} is associated with the water composition such as pigment, dissolved organic and detritus (CARDER et., 1989, CARDER et al., 1991, SHANMUGAM et al., 2011). In the Nav dataset, the spectral slope varied from 0.010 to 0.012 nm^{-1}, therefore, the original offset value from Mishra et al. (2014) was replaced with 0.0095 after a simple optimization using the *in situ* range. The new calibration for ξ is give below:

$$S_{CDM} = 0.0095 + \left(\frac{0.002}{0.6 + (r_{rs}490/r_{rs}\lambda_0)}\right) \tag{4.15}$$

$$\xi = \exp[S \times (443 - 412)] \tag{4.16}$$

The remaining steps proposed by Mishra et al. (2014) were used to derive a_{CDM} in the current model (Figure 4.4b). The average errors showed great improvement mainly at shorter wavelengths when compared to the previous versions (Table 4.4). The agreement between measured and estimated values showed an average MAPE of 18.87 % and the bands at 681 and 709 nm had the highest errors, 24.18 and 30.66 % respectively. Mishra et al. (2014) observed a similar trend of high error at longer wavelengths starting from 560 nm and highlighted that the magnitude of a_{CDM} at this region is small and therefore does not affect the overall performance to a large extent. Besides, the main spectral region associated to a_{CDOM} is situated in the blue

region. For instance, at 440 nm, a_{CDOM} is considered a proxy of its concentration and used in remote sensing inversion (LEE and HU, 2006, ZHU et al., 2011). a_{CDM} using QAA_{OMR} produced the least error at blue wavelengths, specifically at 443 nm.

Table 4.4. Comparative band-specific errors related to the re-parameterization of $a_{CDM}(\lambda)$ based on MAPE (%) and RSMD (m^{-1}) metrics.

	QAA_{Lv5}		QAA_{Lv6}		QAA_{M14}		QAA_{OMR}	
Bands (nm)	**RMSD (m^{-1})**	**MAPE (%)**	**RMSD (m^{-1})**	**MAPE (%)**	**RMSD (m^{-1})**	**MAPE (%)**	**RMSD (m^{-1})**	**MAPE (%)**
412	1.03	81.35	0.96	75.81	0.93	72.88	0.21	12.76
443	0.74	83.90	0.69	79.13	0.67	76.61	0.13	12.99
490	0.47	87.77	0.45	84.14	0.44	82.22	0.08	14.68
510	0.38	89.06	0.37	85.81	0.36	84.09	0.07	15.57
560	0.22	91.53	0.21	89.02	0.21	87.70	0.04	17.98
620	0.13	94.28	0.12	92.61	0.12	91.74	0.03	19.92
665	0.10	96.48	0.10	95.45	0.10	94.89	0.03	21.04
681	0.10	97.15	0.09	96.31	0.09	95.86	0.03	24.18
709	0.08	97.89	0.08	97.27	0.08	96.93	0.03	30.66
Average	**0.36**	**91.05**	**0.34**	**88.39**	**0.33**	**86.99**	**0.07**	**18.87**

Figure 4.6a, showed that both QAA_{Lv5} and QAA_{Lv6} presented low σ^* (0.21 and 0.31, respectively) and *R* very close to these values (0.28 and 0.34, respectively) which means that *uRMSD** was minimum in those models. On the other hand, QAA_{OMR} showed a σ^* = 1.16 and *R* = 0.54, which is closer to the reference value when compared to other models. The difference from all the models can be distinguished in the Target diagram (Figure 4.6b), and QAA_{OMR} is the only model displayed with *B** = -0.12, depicting the underestimation of $a_{CDM}(443)$, while the other models presented *B** between -6.28 and-5.73. The green data symbol is close to the black circle indicating a *uRMSD** close to 1. Figure 4.6c, showed again the good performance of QAA_{OMR} in retrieving $a_{CDM}(560)$. Overall the result was just like the previous one but now the parametrized model presented a *B** = 0.59, highlighting the overestimation pattern (Figure 4.6d). At 665 nm, the QAA_{OMR} again showed better combination of σ^*, *R* and *B** (Figure 4.6e, f). Information about the bias contributes to the sense of scale or magnitude to the model skill assessment process, therefore, is not suitable to use only Taylor diagram to evaluate the performance of a model.

Figure 4.6. Taylor diagrams for $a_{CDM}(\lambda)$ at (a) 443 nm, (c) 560 nm, (e) 665 nm. Target diagrams for $a_{CDM}(\lambda)$ at (b) 443 nm, (d) 560 nm and (f) 665 nm. Symbols indicate the following: QAA_{Lv5} (grey dot), QAA_{Lv6} (yellow dot), QAA_{M14} (blue dot) and the QAA_{OMR} (green dot), reference observation (red dot). The black circle in the Target diagrams (M_0) corresponds to a normalized total RMSD of 1.0.

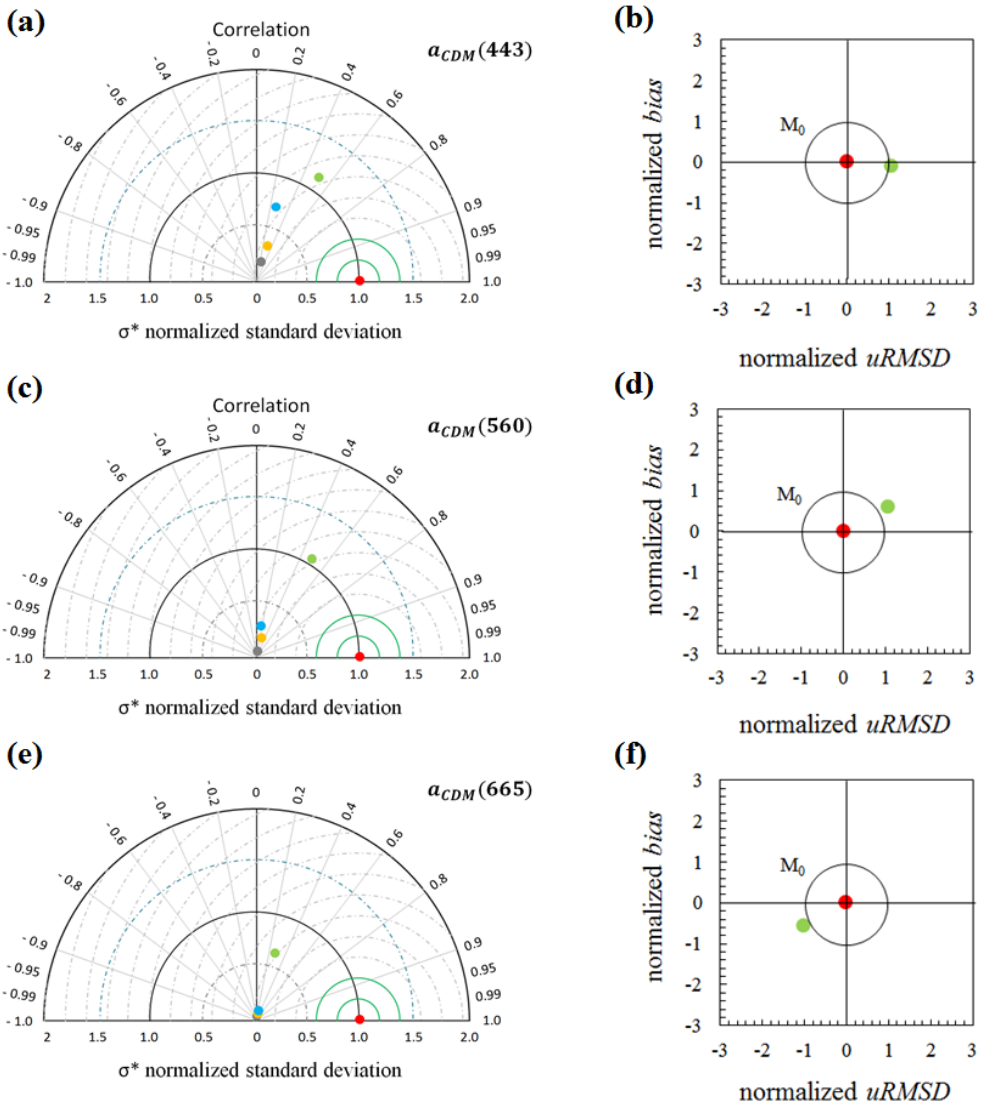

4.3.7 Re-parametrization of QAA to derive a_ϕ

In a_ϕ estimation (Table 4.5), QAA_{Lv5} and QAA_{Lv6} produced very high errors, mainly in long wavelengths and retrieved negative values, on the other hand, QAA_{M14} provided positive values but the errors were too high. To overcome these bad performances, a combined model based on Roesler et al. (1989) and Lee et al. (2010) was carried out. Ogashawara et al. (2016) first applied the approach using both references; however, our proposal did not use factors C_1 and C_2 employed to compute CDOM influence in the water column neither the band

combination used to derive $a_\phi(\lambda_0)$. $a_\phi(443)$ was calculated according to Lee et al. (2010) as a function of ξ and ξ, the parameters also used in $a_{CDM}(\lambda_0)$. The combination of wavelengths was slightly changed from the original as presented in Equation 4.17.

$$a_\phi(443) = \frac{[\xi a_t(443) - a_t(412)] - [\xi a_w(412) - a_w(412)]}{\xi - \zeta} \quad (4.17)$$

$a_\phi(\lambda)$ was then calculated by multiplying $a_\phi(443)$ by the normalized spectral absorption, $a_\phi^+(\lambda)$, described by Roesler et al. (1989) and presented in Eq. 4.18. The $a_\phi^+(\lambda)$ component aim to reproduce the spectral shape for $a_\phi(\lambda)$. In order to find the suitable spectrum of $a_\phi^+(\lambda)$, the calibrated dataset was used in Equations 4.19 and 4.20.

$$a_\phi(\lambda) = a_\phi(443) \times a_\phi^+(\lambda) \quad (4.18)$$

$$a_\phi^+(\lambda) = \frac{a_\phi(\lambda)_i}{a_{\phi i}} \quad (4.19)$$

$$a_{\phi i} = \frac{\int a_\phi\,(\lambda)_i d\lambda}{\lambda_{max} - \lambda_{min}} \quad (4.20)$$

where, $a_\phi(\lambda)_i$ is the spectral absorption of phytoplankton, $a_{\phi i}$ is spectrally averaged absorption coefficient of phytoplankton (350 – 800 nm), λ_{max} and λ_{min} are the maximum and minimum wavelengths. The numerator component of Eq. 4.21 was derived based on the area under the curve notion (AUC) and then divided by the spectral difference ($\lambda_{max} - \lambda_{min}$). Then, the *in situ* $a_\phi(\lambda)_i$ was divided by the latter component. A representative spectrum from Eq. 4.20 was chosen by statistic metrics (average, standard deviation, minimum, maximum and median) and for Nav's dataset, the minimum spectrum was suitable to represent the $a_\phi^+(\lambda)$. The Eq. 4.18 is used in order to remove the effect of concentration and permits the estimation of variance due uniquely to spectral shape (ROESLER et al., 1989).

As result (Figure 4.4c, Table 4.5), the agreement between measured and estimated $a_\phi(\lambda)$ from the re-parametrized model produced the lowest average values of MAPE = 46.80 % and RMSD = 0.10 m^{-1}. The band specific contribution showed that other models performed slightly better in the blue regions compared to QAA_{OMR}. For instance, QAA_{Lv6} produced the least errors in 412 and 443 nm; similarly, QAA_{M14} had a MAPE of 42.84% at 681nm. However, QAA_{OMR} showed consistent low errors across all OLCI bands without a spike in errors in a

specific band unlike other QAAs. In addition, QAA_{OMR} produced the least errors at 620, 665 and 709 nm with MAPE ranging between 45.56 – 53.29 %.

Table 4.5. Comparative band-specific errors related to the re-parametrization of $a_\phi(\lambda)$ based on MAPE (%) and RSMD (m^{-1}) metrics.

	QAA_{Lv5}		QAA_{Lv6}		QAA_{M14}		QAA_{OMR}.	
Bands (nm)	**RMSD (m^{-1})**	**MAPE (%)**	**RMSD (m^{-1})**	**MAPE (%)**	**RMSD (m^{-1})**	**MAPE (%)**	**RMSD (m^{-1})**	**MAPE (%)**
412	0.19	53.69	0.11	21.31	0.14	33.80	0.19	44.39
443	0.15	40.10	0.10	25.20	0.17	45.24	0.18	42.67
490	0.04	24.02	0.14	92.11	0.22	130.02	0.10	47.57
510	0.04	34.77	0.16	150.98	0.22	184.86	0.08	47.97
560	0.03	42.49	0.16	238.37	0.18	229.39	0.05	47.28
620	0.11	100.73	0.33	402.82	0.19	173.98	0.06	45.56
665	0.25	157.52	0.37	264.71	0.11	56.92	0.09	46.47
681	0.29	167.75	0.38	241.91	0.10	42.84	0.10	46.04
709	0.38	870.85	0.69	1858.15	0.04	63.91	0.04	53.29
Average	**0.16**	**165.77**	**0.27**	**366.17**	**0.15**	**106.77**	**0.10**	**46.80**

As depicted in Figure 4.7a both QAA_{Lv5} and QAA_{Lv6} showed low variability regarding the reference dataset at 443 nm, while QAA_{M14} and QAA_{OMR} presented high σ^* (1.55 and 1.60, respectively). Figure 4.7b, showed that QAA_{M14} overestimated a_ϕ and also produced high *uRMSD** (1.92) followed by QAA_{OMR} (2.13). To produce the best match between measured and estimated values requires a combination of low *uRMSD** and *B**, thus at 443 nm QAA_{Lv6} provided the best fit for a_ϕ followed by QAA_{Lv5} and QAA_{OMR}. At 560 nm, QAA_{Lv5} and QAA_{OMR} presented the lowest σ^* (0.14 and 0.76, respectively) while the *R* was 0.40 and -0.31, respectively (Figure 4.7c). Again, only QAA_{Lv5} and QAA_{OMR} produced low *uRMSD** and *B**, but the first one was slightly better than the latter one (Figure 4.7d). Even producing the lowest variability between reference and modeled data, QAA_{Lv6} overestimated the variance of $a_\phi(665)$ becoming not a good approach. On the other hand, QAA_{OMR}, presented the lowest *B** (-0.246) showing to be the best approach from all the ones evaluated (Figure 4.7e, f). As mentioned in the previous section, the band specific errors varied widely between models.

The modifications improved $a_\phi(\lambda)$ retrieval for an average error (MAPE) of ~47%. The difficulty in retrieving $a_\phi(\lambda)$ was probably due to the very low Chl-*a* concentration combined with the dominance of a_d in the blue and green regions followed by a_{CDOM} dominating a_t at 412 nm. Lee et al. (2010) also highlighted the great effort to estimate $a_\phi(\lambda)$ in complex waters. The authors, observed that uncertainties associated to $a_{CDM}(\lambda)$ is smaller than that of $a_\phi(\lambda)$ and therefore methods other than simple algebraic inversions are required to improve the quality

of $a_\phi(\lambda)$ derivation. Besides, refinements are expected when parametrizations regarding $a_t(\lambda_0)$, η, ζ and ξ for several regions are carried out.

Figure 4.7. Taylor diagrams for $a_\phi(\lambda)$ at (a) 443 nm, (c) 560 nm, (e) 665 nm. Target diagrams also for $a_\phi(\lambda)$ at (b) 443 nm, (d) 560 nm and (f) 665 nm. Symbols indicate the following: QAA_{Lv5} (grey dot), QAA_{Lv6} (yellow dot), QAA_{M14} (blue dot) and the QAA_{OMR} (green dot), reference observation (red dot).

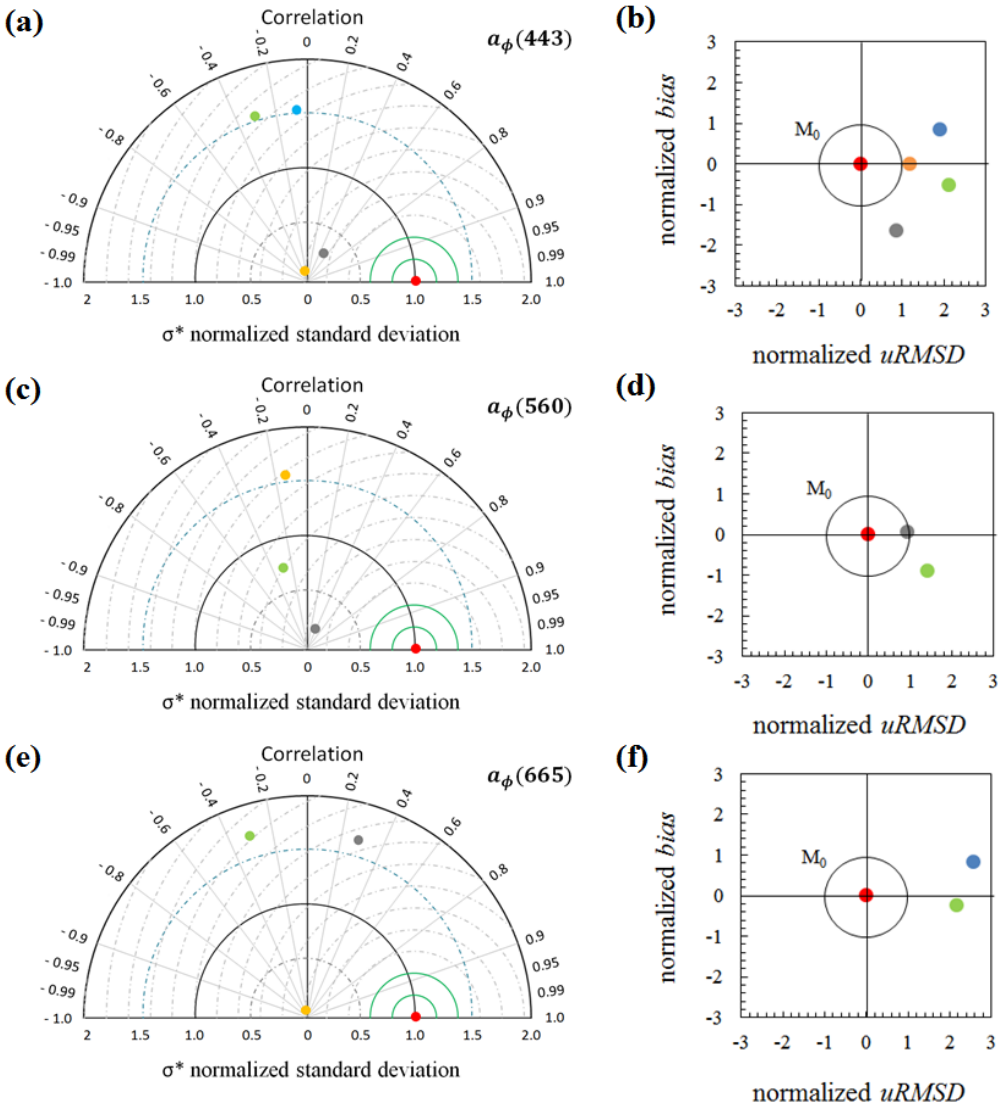

4.3.8 Model Validation

An independent dataset (n = 14) collected in September 2014 (Nav 2, see Figure 2.1 for sample location) were used to verify the performance of QAA_{OMR} by comparing *in situ* and derived measurements at OLCI spectral bands. The results related to backscattering were not

assessed due to lack of data availability. The shorter wavelengths were highly affected by inorganic and dissolved matter (Figure 4.2). Intermediary steps, such as the tuning of χ and η were also relevant to achieve the best fit for a_t. Lee et al. (2010) suggested that in order to get error free a_t, efforts must be taken to minimize the estimation error for $a_t(\lambda_0)$ and η.

Figure 4.8. Validation result showing the scatter plot between measured and estimated (a) $a_t(\lambda)$, (b) $a_{CDM}(\lambda)$, (c) $a_\phi(\lambda)$ and the comparison of spectral shape of average measured and estimated (d) $a_t(\lambda)$, (e) $a_{CDM}(\lambda)$ and (f) $a_\phi(\lambda)$.

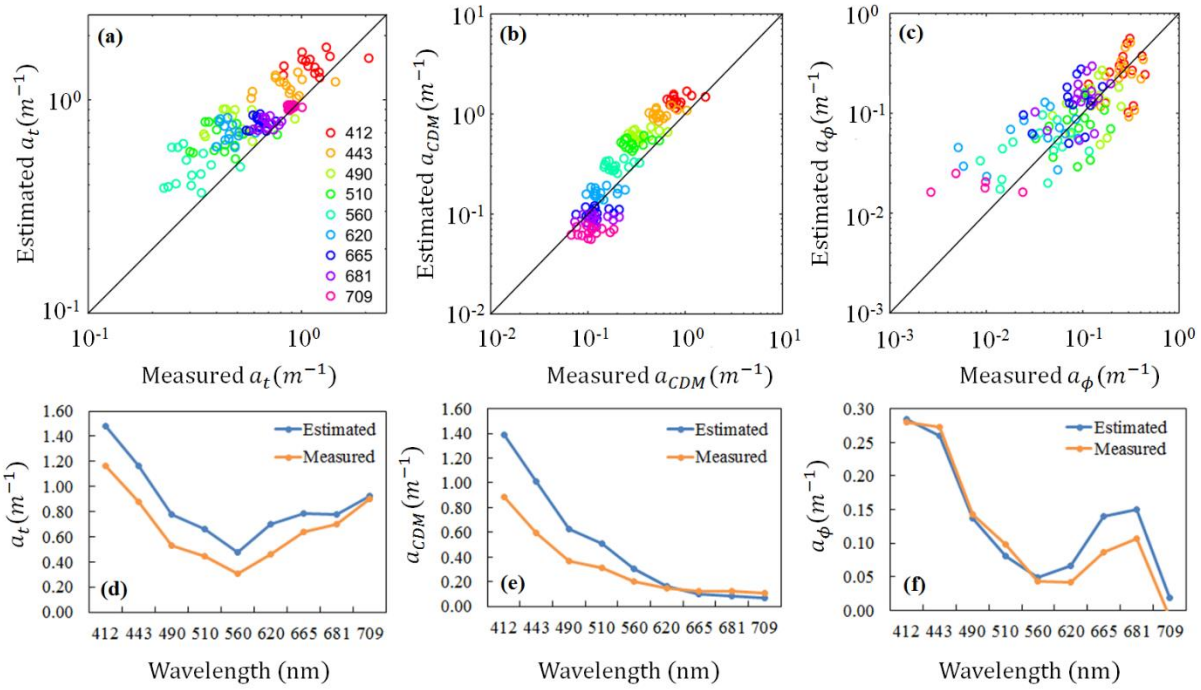

The uncertainty based on average MAPE was above 50% for a_t between 490 – 620 nm and the lowest errors were seen at 709 nm (0.45 – 9.62%, *n* = 14), 681 nm (1.67 – 27.17%, *n* = 14), 665 nm (4.38 – 43.13%, *n* = 14) and 412 nm (4.70 – 73.62%, *n* = 14). Three specific sampling stations (P9, P13 and P19) were responsible for the increase in error above 50% and after the removal of these samples, the average MAPE decreased below 50% at all OLCI wavelengths. These samples presented the lowest a_t values from all dataset considering all wavelengths suggesting that QAA_{OMR} was not able to retrieve a_t in such magnitudes. However, those samples were preserved to generate graphics in Figure 4.8. The a_{CDM} validation (Figure 4.8c and d) showed a good fit mainly in longer wavelengths. The average MAPE was 52.15% and the highest error was seen at 490 nm (79.89%), 443 nm (78.30%), 412 nm (66.21%) and 560 nm (58.89%). However, when the same three-outlier stations data were eliminated, the

average MAPE decreased to 45.11%. The accuracy of $a_{CDM}(\lambda)$ and $a_{\phi}(\lambda)$ is associated with the uncertainties in $a_t(\lambda)$ and the parameters ζ and ξ (Lee et al. 2010). The reference $a_{CDM}(443)$ was overestimated, possibly due to the mismatch between *in situ* and measured ζ and ξ. The estimation of a_{ϕ} followed a hybrid method different from the native QAA in order to avoid negative prediction and maintain the shape, which can be difficult to achieve in waters with very low Chl-*a* concentrations.

Although a_{ϕ} prediction at some sampling locations were dispersed (Figure 4.8e), the majority of them were centered on the 1:1 line and the average estimated spectrum matched well with the *in situ* measurements. This step was dependent on the uncertainties associated with $a_t(\lambda)$ and ζ and ξ parameters. High MAPE values (average 74.65%) were observed from 412 to 681 nm and the highest errors were associated at longer wavelengths, mainly at 520, 620 and 665 nm. At least four stations (P2, P9, P13 and P19) contributed to this increased error. After excluding those samples, the average error decreased to 53.17%. It is worth mentioning that *in situ* $a_{\phi}(709)$ returned negative values using the protocol described in the Section "Data and Methods", for that reason, we disregarded data from this wavelength.

Overall, the QAA_{OMR} improved the estimative of IOPs for Nav but the challenge remains focused on a_{ϕ} retrieval. Ogashawara et al. (2016) also found low accuracy studying Itumbiara reservoir (CDOM rich water) located in west center of Brazil, in the regions of 400 – 500 nm and 500 – 600 nm for a_t. For a_{CDM}, the uncertainties decreased but the errors were associated to the intervals from 500 – 600 nm and 600 – 750 nm whereas for a_{ϕ} the challenge was to improve accuracy between 400 – 500 nm and 500 – 600 nm. These results imply that different optical water quality environments can react differently with different QAA versions, however, the efforts accomplished up to now showed improvements in retrieving IOPs in oligo-to-mesotrophic water bodies. The authors also highlighted the need of additional tuning and validation exercises using broad geographic regions in order to increase IOP prediction.

4.3.9 Linking IOPs variability to physical and meteorological variation

In situ $R_{rs}(\lambda)$ data corresponding to the third field trip was used to retrieve the IOPs based on QAA_{OMR}. $a_t(443)$ data retrieved from QAA_{OMR} regarding the first, second and third field trips were averaged and then plotted on rainfall, runoff, water level and discharge graphics (Figure 4.9). Total rainfall during the months of April/2014, September/2014 and May/2016 were 60.33 mm, 169.95 mm and 197.49 mm, respectively (Figure 4.9a). There was a growing

trend from October/2013 to August/2016 and according to Coelho et al. (2015), the State of São Paulo experienced in 2014 and early 2015 a dramatic decline in rainfall rate with the interval of Dec/2013 – Mar/2014 as the one of the driest summer of the 1961-2015 record. The drought conditions affected the water availability for agriculture, hydropower generation and public use during the austral summer (December – March). Extreme events such as droughts can affect the water supply and because of that, public strategies are needed to avoid water quality decrease (KHAN et al., 2015). Besides, Cairo et al. (2016) reported the influence of the atypical dry year of 2014 in water quality. They noticed that Ibitinga reservoir, also displayed along the Tietê river cascade system, worked as an accumulator of organic matter due to the decrease of precipitation rate and increase of retention time. The water quality composition is highly affected by the rainy and dry seasons and the rising of nutrient loads as well as the worsening of water transparency can be due to allochthonous sources that are maximized during the rainy season as result of surface Runoff (SOARES and MOZETO, 2006; CUNHA et al., 2016). Regarding the $a_t(443)$ values, we can notice the growing trend from the first to the third field trips as result of rainy conditions that increased from April to September of 2014 and then in May/2016.

The runoff (Figure 4.9b) corroborated to the rainfall data, which means that in April/2014, the external contribution due to land water toward the reservoir was lower compared to September/2014 and May/2016. Nonpoint pollutants attributable to agricultural activities can be carried across the land surface by runoff and reach the reservoir, increasing the loads of nutrients leading to water quality degradation (RITTER and SHIRMOHAMMADI, 2000). As displayed in Table 4.1, the water quality parameters got worse from the first to the second field trip, showing high concentrations of TSS and Chl-*a* and decrease of water visibility due to increased turbidity. Smith et al. (2014) and Rodgher et al. (2005) found an increase of total phosphorus, nitrite and suspended materials during rainy season from upstream to downstream in Tietê River. The increase of nitrite and total phosphorus was related to soil fertilization. Numerous studies have reported similar phenomena of increased nutrient load caused by stream inputs and surface runoff (VAROL et al., 2012; PERBICHE-NEVES et al., 2011; HENRY et al., 1999). As in the rainfall graphic, $a_t(443)$ also increased with increasing runoff emphasizing the growing trend from 2014 to 2016. This means that, inputs from the watershed contribute to the increase of absorbing components, such as dissolved and particulate matter.

Figure 4.9. Graphic depicting the (a) rainfall, (b) runoff, (c) water level and (d) discharge variability along the period between October 2013 and August 2016. The green diamonds represent $a_t(443)$ retrieved based on QAA_{OMR} from the three field trips carried out in Nav during April/2014, September/2014 and May/2016. Rainfall data was acquired in NASA's GIOVANNI database based on TRMM data with 0.25° of spatial resolution (http://giovanni.sci.gsfc.nasa.gov/giovanni/). Runoff data was also acquired through NASA's GIOVANNI database. Water level as well as discharge were downloaded from the Water National Agency of Brazil through the website (http://sar.ana.gov.br/).

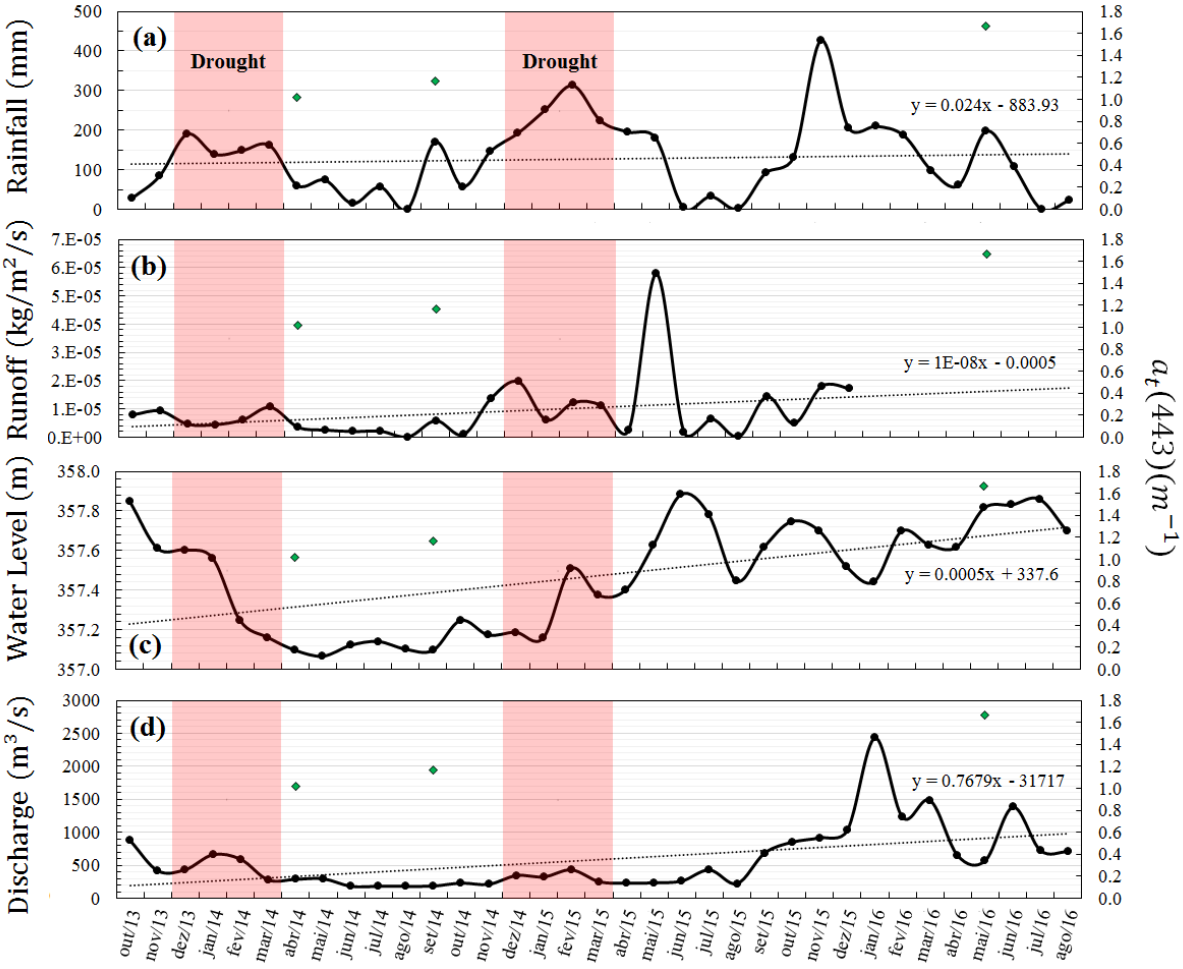

Regarding the water level of Nav reservoir (Figure 4.9c), the annual average in 2014 was 357.18 ± 0.15 m followed by 357.56 ± 0.23 m in 2015 and from January to August of 2016 the average was 357.70 ± 0.20 m showing low variability but a growing trend from 2014 to 2016. The low water level variance is because Nav is a run-of-river reservoir and therefore, there is no water storage. In addition, this kind of operation system presents short water retention time (WRT) and the shape is in general simpler and shallower (PERBICHE-NEVES and NOGUEIRA, 2013). The maximum water discharge (Figure 4.9d) occurred in January, March and June of 2016 and was in accordance with the rainfall pattern. Along the years of

2014 and 2015, the discharge virtually remained stagnant showing signs of recovery in 2016 as presented by the trend line. This was probably related to the extreme events of droughts in those two specific years. The discharge is indirectly related to WRT, which means that high discharge demands short WRT and according to Soares et al. (2008), this feature affected the longitudinal stratification period in a reservoir in Southern Brazil, while Straskraba and Tundisi (1999) discussed the impact of WRT on the vertical stability of reservoirs. Jones and Elliott (2007) observed a high phytoplankton biomass and longer algal blooms by increasing the WRT.

4.3.10 Factors influencing optical changes in the reservoir

Land use and land cover (LULC) can affect the water quality composition by supplying particulate and dissolved matter leading to the modification of optical properties. Land uses such as urban land cover and agriculture can be associated with suspended solids (MOURI et al., 2011; CUNHA et al., 2016). In São Paulo State, erosion processes contribute with soil loss in watersheds dominated by agriculture carrying to water sediments and terrestrial matter (MERTEN and MINELLA, 2013). Le et al. (2015) found that both land uses (urban + agriculture) play an important role in light attenuation in the estuaries as result of absorption by phytoplankton. The intensification of primary production can be motivated by the input of nutrients such as phosphorus increasing the $a_{\phi}(443)$. Areas covered by forests can improve water quality by reducing the erosion processes and sediment inputs (CUNHA et al., 2016).

In Tietê River, the most significant sources of pollution come from the metropolitan and industrial region of São Paulo. However, the water quality improves from the upstream reservoirs to the downstream due to auto-depuration and sedimentation of suspended matter increasing the dissolved oxygen and water clarity (BARBOSA et al., 1999). The LULC in Nav is basically composed by agriculture, especially sugarcane and pasture whereas other classes such as riparian forests are absent around the reservoir (PETESSE and PETRERE, 2012). These results are in accordance with Figure 4.2, showing that detritus and CDOM control IOPs from Nav at 443 nm. These imply that both OSCs are dominant in the reservoir and can be linked to watershed activities. The region is also comprised by high content of sand and low levels of ultisol (EMBRAPA, 1999).

According to Figures 4.10a and 4.10d, when $a_t(443)$ is analyzed based on overall dataset the correlation with TSS and Chl-*a* was very high (r = 0.80 and r = 0.79, $p < 0.001$, respectively). However, when $a_t(443)$ is based on individual campaigns, the correlation with TSS drops and only data from Nav 2 showed to be statistically significant (r = 0.54, $p < 0.05$)

whereas the correlation between $a_t(443)$ and Chl-*a* was nonsignificant ($p > 0.05$) considering campaigns individually. The $a_{CDM}(443)$ overall dataset (Figure 4.10b, e) presented a correlation of 0.66 ($p < 0.001$) with both TSS and Chl-*a*, on the other hand, the individual campaigns did not present any statistical correlation between $a_{CDM}(443)$, TSS and Chl-*a*. Regarding the overall data, the correlation between TSS and Chl-*a* (Figure 4.10c) was 0.88 ($p < 0.001$) although, from all campaigns only Nav 2 and Nav 3 were statistically significant (r = 0.62 and 0.80, respectively, $p < 0.05$). The relationship between $a_\phi(443)$ and Chl-*a* (Figure 4.10f) was weak but significant (r = 0.51, $p < 0.001$).

Figure 4.10. Relationship between optical properties and water quality parameters: (a) $a_t(443)$ versus TSS; (b) $a_{CDM}(443)$ versus TSS; (c) $a_\phi(443)$ versus TSS; (d) $a_t(443)$ versus Chl-*a*; (e) $a_{CDM}(443)$ versus Chl-*a* and (f) $a_\phi(443)$ versus Chl-*a*.

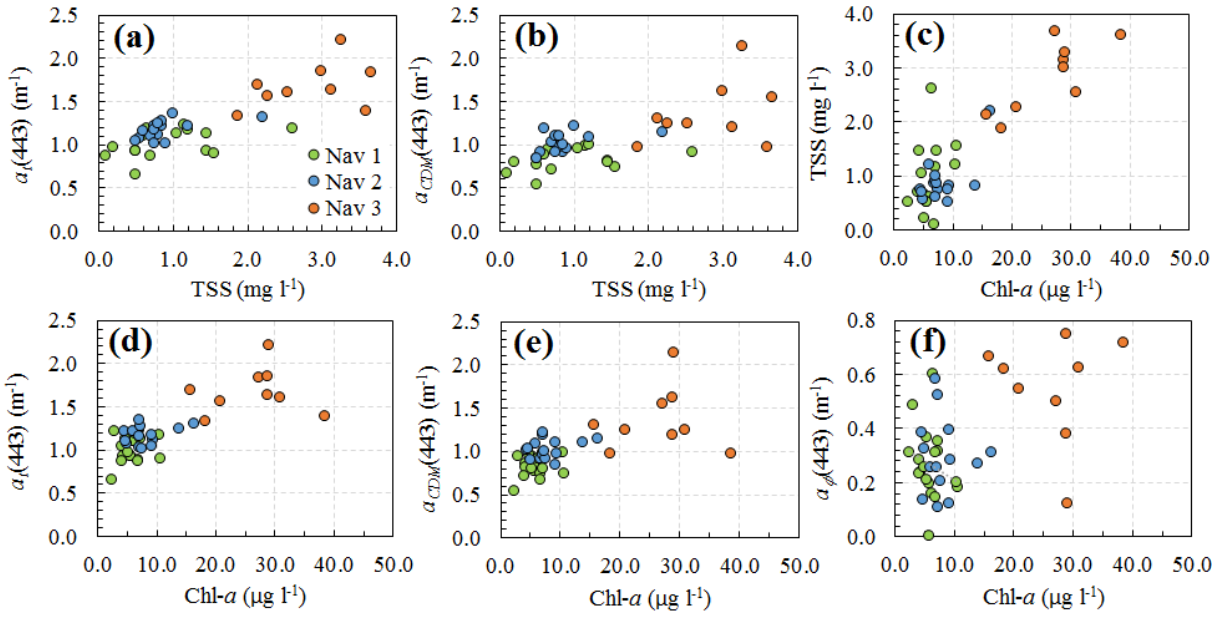

The results revealed that the poor correlation between TSS and Chl-*a* in Nav 1 (r = 0.35, $p > 0.05$) indicates that Chl-*a* was not the only parameter controlling the water optical properties thus assuming a typical case 2 water (MOREL and PRIEUR, 1977). Besides, the weak or noncorrelation allied with the low Chl-*a* concentration suggested the both TSS and CDOM were mainly originated from allochthonous sources or even sediment resuspension but not from the degradation product of phytoplankton. Wu et al. (2011) who studied an inorganic matter dominated lake (Poyang, China) found the same observation. The low agreement between $a_\phi(443)$ and Chl-*a* corroborated with previous results and together with $R_{rs}^{-1}(\lambda)$, presented in

Figure 2, we can notice the inexistence of a pronounced absorption valley at 443 nm, that is typical of phytoplankton dominated waters (YANG et al., 2013, MISHRA et al., 2014).

4.3.11 Implications of QAA_{OMR} for water resource management

Nowadays, water quality monitoring along the set of reservoirs of Tietê River has been carried out using traditional techniques with high cost and low temporal and spatial variability. The implication of this can be followed by the lack of information about the sources of water contamination and possibility to perform cross analysis with other variables such as LULC data. Understanding the water constitution, we can also understand how to proceed in decision making avoiding high cost of *in situ* data collection granting accurate information.

Up to now, the QAA is available with high accuracy for ocean and coastal waters (LEE et al., 2002, ZHU et al., 2011, ORGANELLI et al., 2016) and was evaluated for inland waters (LE et al., 2009a, LI et al., 2016). Improvements were carried out in order to adequate QAA for very turbid and productive waters (MISHRA et al., 2013, 2014, WATANABE et al., 2016a). However, in inland waters with low Chl-*a* and TSS concentrations, such as Nav, few works showed improvements but still high uncertainties (LI et al., 2016, OGASHAWARA et al., 2016). Our findings based upon *in situ* observations revealed that the enhancement of QAA could estimate the IOPs with high accuracy showing the potential of this approach in back up the water resource management in Tietê River with extension to other oligo-to-mesotrophic environments.

4.4 Conclusion

Despite the significant effort in retrieving the IOPs by QAA algorithm for open ocean, coastal and very productive waters, applications focused on non-productive inland waters and inorganic matter dominated remains a challenge. In this study, three well-known QAAs were applied and their performance was compared in an oligo-to-mesotrophic reservoir in Southeast of Brazil. The QAA_{Lv5}, QAA_{Lv6} and QAA_{M14} were developed to retrieve IOPs in open ocean, coastal water and very productive inland waters, respectively. These models did not show a good agreement between estimated and measured $a_t(\lambda)$, $a_{CDM}(\lambda)$ and $a_\phi(\lambda)$ and the main issue behind this failure was first addressed to the reference wavelength selection, which is responsible to highlight just the contribution of water in the total absorption budget.

The bad performance of previous QAAs motivated us to modify the existent code shifting the reference wavelength to 709 nm (available in both MSI/Sentinel-2 and OLCI/Sentinel-3) and then re-parametrize the $a_t(\lambda_0)$ and η in order to retrieve $a_t(\lambda)$ and $b_b(\lambda)$. This step was of paramount relevance even considered by Lee et al. (2002) as a second order of importance, because all the further steps depend on $a_t(\lambda)$ to estimate $a_{CDM}(\lambda)$, and $a_\phi(\lambda)$. Besides, the properties ζ and ξ also considered of second order of importance, showed to be significant for retrieving $a_{CDM}(\lambda_0)$, and $a_\phi(\lambda_0)$. Specifically, the changes ran through modification of band combination (443, 665, 709, 681 nm) designed to retrieve χ and further the estimation of new coefficients for $a_t(\lambda_0)$ retrieval. Also assigned as necessary, the definition of η based on bands 665 and 754 nm increased the accuracy of $a_t(\lambda)$ measure.

The main obstacle found on previous QAAs was related to $a_\phi(\lambda)$ retrieval based on simple subtraction between $a_t(\lambda)$ and $a_{CDM}(\lambda)$, however, the errors was very high surpassing 100% of uncertainties considering specific wavelengths. Therefore, we came up with a new approach recently suggested by Ogashawara et al. (2016) but with relevant modifications aiming to derive $a_\phi(443)$ based on Lee et al. (2010) and the normalized $a_\phi^+(\lambda)$ discussed by Roesler et al. (1989). As result, we achieved great improvement with uncertainties below 50% (412 – 681 nm). Using an independent dataset, a validation exercise was carried out, and QAA_{OMR} showed to be robust in retrieving the IOPs, and even assuring the necessity of use data from broader geographic regions, the model comes to give a better solution for waters characterized as oligo-to-mesotrophic and dominated by inorganic matter.

In order to understand the IOPs variability in Nav, a discussion based on physical and meteorological data was presented. Data of LULC can be the key of trophic state definition and the source of suspended matter as well as CDOM may be associated to agriculture activities. The allochthonous components integrate the aquatic system through rainfall and surface runoff. The low contribution of Chl-*a* in suspended matter was related to the weak relationship between Chl-*a* and TSS and between $a_\phi(443)$ and Chl-*a*. Validation using different locations is encouraged in order to assess the feasibility of the new parametrized coefficients. In general, the model brought a new perspective to water quality monitoring based on oligo-to-mesotrophic environments such as in tropical reservoirs and also, the scale-up of QAA_{OMR} to OLCI sensor is the next step in retrieving the IOPs once this sensor provides strategic and useful bands related to remote sensing of water supporting the water resource management.

CHAPTER 5: EVALUATION OF QAA_{OMR} AND QAA_{BBHR} PERFORMANCES IN DERIVING THE IOPS IN BOTH BB AND NAV RESERVOIRS

5.1 Introduction

The reservoirs of Tietê River set in a cascade system present trophic states ranging from oligo to hypereutrophic, which means that a single method for water resource monitoring using remote sensing technique will demand for a robust approach. The QAA for example, is a valuable method for retrieving the IOP and further applied in semi-analytical approaches for estimating the water quality (MOREL and GORDON, 1980), however, studies revealed that empirical calibration steps are required for different locations (LEE et al., 2002; LE et al., 2009a; YANG et al., 2013; MISHRA et al., 2014, LI et al., 2016, WATANABE et al., 2016a, OGASHAWARA et al., 2016). Li et al. (2016), for instance, applied the QAA_{v5} from Lee et al. (2009) and compared to a modified version of the same approach in various highly turbid waters in China, and they observed the necessary of an optimized algorithm to derive the IOPs in extremely turbid waters.

The limitation of QAA_{v5} in retrieving the absorption coefficients in turbid inland waters was described by Yang et al. (2013). They listed three limiting issues, such as: the estimation of the total absorption coefficient at a reference wavelength, $a(\lambda_0)$, based on synthetic data. Secondly, the spectral power for particle backscattering coefficient, η, was calibrated considering the data from open oceans or coastal waters. The last issue regards the use of synthetic data for estimating the phytoplankton absorption. Those steps, were listed by Lee et al. (2002) as second order of importance because they have a narrow range of variation and small influence on the output, however, the authors also mentioned that even classified as second order of importance, they affect the final product and therefore, improvements must be carried out considering regional and seasonal information, or using better algorithms (LEE et al., 2010).

Le et al. (2009a) for example, changed the reference wavelength to 710 nm in the highly turbid water of Taihu Lake and to 780 nm during summer where the water showed to be extremely turbid due to the increase of phytoplankton concentration. Besides, they also changed the band ratio used in η retrieval. Yang et al. (2013) shifted the λ_0 to longer wavelengths (753 nm), replace the empirical model for estimating η for a semi-analytical approach and developed a novel way to retrieve a_ϕ at 443 nm. Mishra et al. (2014) changed the λ_0 to 708 nm and included the band at 620 nm into the empirical step for $a(\lambda_0)$ retrieval. This procedure was due

to the presence of cyanobacteria in the study area. Watanabe et al. (2016) also included the band at 620 nm due to the same reason as previous study. They changed the band combination for ζ retrieval using the ratio $a_\phi(665)/a_\phi(709)$ and altered the a_{CDOM} slope based on in situ data. The non-modification of the a_{CDOM} slope was pointed out as the main cause for the failure of the QAA (LEE et al., 2002) in breaking down the $a(\lambda)$ into CDOM and phytoplankton absorption coefficients in Australian coastal waters (QIN et al., 2007). Ogashawara et al. (2016) re-parameterized the QAA for inland waters dominated by CDOM. For this, they used $\lambda_0(560)$ instead of 709 nm and kept the exponent values from Lee et al. (2009) to estimate $a(\lambda_0)$. A factor to attest the influence of CDOM was computed to derive $a(\lambda)$ and a drastic modification was carried out in $a_\phi(\lambda)$, by mixing both approaches from Lee et al. (2010) and Roesler et al. (1989).

In this manner, improvements in empirical steps are highly recommended for different types of water, however in terms of operational system for water management in a cascade system, where the bio-optical properties vary from upstream to downstream, multiple approaches can be time consuming and unfeasible. Therefore, aiming to assess the performance of a single QAA version to assist the water quality management in Tietê River, the versions from Watanabe et al. (2016a) parameterized to BB and the QAA_{OMR} parametrized to Nav were used and then evaluated to highlight the improvements and fragility from each version supposing to choose a single approach for future use considering the entire cascade system.

5.2 Data and Methods

For this purpose, the dataset from the first and second field trips of BB were applied summing 40 samples while for Nav, data from the three field campaigns were used totalizing 51 samples. The QAA versions from Watanabe et al. (2016a) and the one presented in Chapter 4 were evaluated. *In situ* measures of the IOPs and here represented by the absorption coefficients of phytoplankton, a_ϕ, NAP, a_{NAP}, and CDOM, a_{CDOM} were compared to the estimated values retrieved by the specific QAA version. The combination of a_{CDOM} and a_{NAP} produced the a_{CDM}, one of the QAA products. To obtain the *in situ* absorption coefficient of particulate, a_p, and the respective organic (a_ϕ) and inorganic fraction (a_{NAP}), methods from Tassan and Ferrari (1995, 2002) were applied, while for a_{CDOM}, the method from Tilstone et al. (2002) was used.

The *in situ* R_{rs} data were estimated following the procedure suggested by Mobley

(1999). For this, hyperspectral measures were acquired from the use of the RAMSES TriOS® (TriOS, Germany). The *in situ* R_{rs} were then convolved to the spectral response functions of the Ocean and Land Colour Instrument (OLCI/Sentinel-3 satellite) spectral response (PELLOQUIN and NIEKE, 2012) to derive the band-weighted reflectance data (GORDON, 1995). The simulated R_{rs} from Nav were then used in the $QAAA_{BBHR}$ and the ones from BB were used for QAA_{OMR}. The steps from each version can be found in Table 5.1.

Table 5.1 QAA steps comparing the QAA_{BBHR} from Watanabe et al. (2016a) and the QAA_{OMR} proposed in the last chapter.

QAA_{BBHR}	**QAA_{OMR}**
$r_{rs}(\lambda) = R_{rs}(\lambda)/(0.52 + 1.7R_{rs}(\lambda))$ $u(\lambda) = \frac{-0.0895 + \sqrt{(g_0)^2 + 4g_1 * r_{rs}(\lambda)}}{2 * g_1}; g_0 = 0.089, g_1 = 0.125$	
$\chi = \log\left(\frac{r_{rs}(443) + r_{rs}(665)}{r_{rs}(\lambda_0) + 5\frac{(r_{rs}(620))^2}{r_{rs}(443)}}\right)$	$\chi = \log\left(\frac{r_{rs}(443) + r_{rs}(665)}{r_{rs}(\lambda_0) + 5\frac{(r_{rs}(681))^2}{r_{rs}(443)}}\right)$
$a_t(\lambda_0) = a_w(\lambda_0) + 10^{-0.7702+0.0999\chi+0.0566\chi^2}$ where $\lambda_0 = 709$	$a_t(\lambda_0) = a_w(\lambda_0) + 10^{-1.148+2.814\chi-5.813\chi^2}$ where $\lambda_0 = 709$
$\eta = 2 \times \left(1 - 1.2 \times \exp\left(-0.9 \times \frac{r_{rs}443}{r_{rs}(555)}\right)\right)$	$\eta = 2 \times \left(1 - 1.2 \times \exp\left(-0.9 \times \frac{r_{rs}665}{r_{rs}754}\right)\right)$
$\zeta = 0.3 + \left(\frac{0.2}{0.8 + r_{rs}665/r_{rs}\lambda_0}\right)^*$	$\zeta = 0.5 + \left(\frac{0.2}{0.8 + r_{rs}443/r_{rs}\lambda_0}\right)$
$\xi = \exp[S \times (443 - 411)]$	$\xi = \exp[S \times (443 - 412)]$
$S_{CDM} = 0.014 + \left(\frac{0.002}{0.6 + (r_{rs}443/r_{rs}\lambda_0)}\right)$	$S_{CDM} = 0.0095 + \left(\frac{0.002}{0.6 + (r_{rs}490/r_{rs}\lambda_0)}\right)$
$a_{CDM}(443) = \frac{[a_t(412) - \zeta a_t(443)] - [a_w(412) - \zeta a_w(443)]}{\xi - \zeta}$	$a_{CDM}(443) = \frac{[a_t(412) - \zeta a_t(443)] - [a_w(412) - \zeta a_w(412)]}{\xi - \zeta}$
$a_{CDM}(\lambda) = a_{CDM}(443)e^{-S_{CDM}(\lambda-443)}$	$a_{CDM}(\lambda) = a_{CDM}(443)e^{-S_{CDM}(\lambda-443)}$
—	$a_\phi(443) = \frac{[\xi a_t(443) - a_t(412)] - [\xi a_w(412) - a_w(412)]}{\xi - \zeta}$
	$a_\phi(\lambda) = a_{ph}(443) \times a_\phi^+(\lambda)$
$a_\phi(\lambda) = a_t(\lambda) - a_{CDM}(\lambda) - a_w(\lambda)$	where $a_\phi^+(\lambda) = a_\phi(\lambda)/\frac{\int a_x(\lambda)d\lambda}{\lambda_{max}-\lambda_{min}}$

* the original ζ related the ratio between $a_\phi(412)$ and $a_\phi(443)$, however, QAA_{BBHR} used the relation between $a_\phi(665)$ and $a_\phi(709)$

The statistical indicators used for validation were the total root mean square difference (RMSD), the mean absolute percentage error (MAPE) and the *bias*, represented by the equations 4.4, 4.5 and 5.1, respectively.

$$bias = \frac{1}{n}\sum_{i=1}^{n}\left(x_{est,i} - x_{meas,i}\right) \quad (5.1)$$

where n is the number of samples, $x_{est,i}$ and $x_{meas,i}$ represent the estimated and measured values, respectively.

5.3 Results and Discussion

The results are organized in two sections, first presenting the outcomes from QAA_{BBHR} applied to Nav's dataset and then QAA_{OMR} used in BB's dataset.

5.3.1 Use of QAA_{BBHR} in Nav's dataset

This application showed that QAA_{BBHR} performed well for $a_t(\lambda)$ retrieval (Figure 5.1a) with average MAPE of 23.02% (Table 5.1), below the one found by Watanabe et al. (2016a) for parametrization of the current model registering an average of 28.27% using BB dataset. The algorithm exhibited limitation in estimating $a_t(\lambda)$ at 412 and 560 nm in Nav, whilst the best result was observed at 665, 681 and 709 nm, with uncertainties ranging between 5.36 and 13.50%. For QAA_{BBHR} parametrization, the authors found that the best result was observed at 681 nm, that is associated with Chl-*a* fluorescence, and here the best result was achieved at 709 nm (MAPE = 5.36%), differently from Watanabe's result, who found the worst fit at this wavelength. Is worth pointing out that 709 nm was chosen as the reference wavelength for QAA_{BBHR} due to the dominance of pure water in the absorption budget at this wavelength, so the interference of other OSCs than pure water is supposed to be minimal. On the other hand, the worst performance at shorter wavelengths might be related also to the in-water constituents, that is, in Nav, at 412 and 443 nm the influence of phytoplankton is almost inexistent when compared to NAP and CDOM absorption. In general, the model underestimated $a_t(\lambda)$ with average of -0.05.

Figure 5.1. Scatter plots in log-scale between measured and estimated $a_t(\lambda)$, $a_{CDM}(\lambda)$ and $a_\phi(\lambda)$ at OLCI spectral bands.

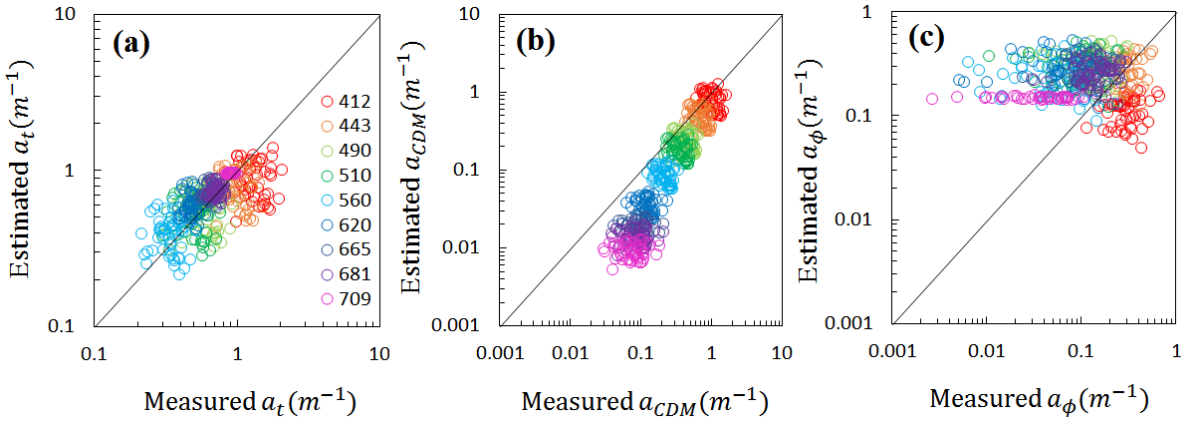

A decline of the result of QAA_{BBHR} for $a_{CDM}(\lambda)$ was observed for Nav (Figure 5.1b) with average MAPE of 59.40% (Table 5.1). Watanabe et al. (2016a) found an average of 47.41% and the best result was observed at the red spectral region when they considered the normalized root mean square error (NRMSE) as uncertainty, however, considering the MAPE, the red region presented the worst result while at shorter wavelengths, the MAPE was lower. In Nav's dataset, the result followed the same trend with MAPE above 50% in the green to NIR wavelengths (58.52 – 86.41%). Mishra et al. (2014) observed a similar trend of high error at longer wavelengths starting from 560 nm and emphasized that the magnitude of a_{CDM} at this region is small and therefore does not affect the overall performance to a large extent. In addition, is worth noting that the main spectral region associated to a_{CDOM} is placed in the blue region (443 nm as a proxy for CDOM concentration) (Lee and Hu 2006). Thus, the error related to this wavelength was 34.13%, with bias of -0.24 m^{-1} showing inclination for underestimation and the RMSD of 0.43 m^{-1} was below the average *in situ* $a_{CDM}(443)$ of 0.72 m^{-1}.

Table 5.2. Comparative band-specific errors related to the IOPs retrieved by QAA_{BBHR} based on MAPE (%), RSMD (m^{-1}) and bias (m^{-1}) metrics.

	$a_t(\lambda)$			$a_{CDM}(\lambda)$			$a_\phi(\lambda)$		
Bands (nm)	**RMSD (m^{-1})**	**MAPE (%)**	***bias*** **(m^{-1})**	**RMSD (m^{-1})**	**MAPE (%)**	***bias*** **(m^{-1})**	**RMSD (m^{-1})**	**MAPE (%)**	***bias*** **(m^{-1})**
412	0.59	33.91	-0.46	0.43	30.71	-0.25	0.24	61.85	-0.21
443	0.39	27.54	-0.25	0.33	34.13	-0.24	0.12	38.42	-0.01
490	0.21	27.44	-0.03	0.25	43.90	-0.21	0.21	197.69	0.18
510	0.17	27.86	0.00	0.22	48.33	-0.19	0.22	341.67	0.19
560	0.14	33.91	0.05	0.15	58.52	-0.13	0.21	608.97	0.18
620	0.16	28.16	0.12	0.10	70.35	-0.09	0.24	538.90	0.21
665	0.11	13.50	0.06	0.09	79.46	-0.08	0.17	156.39	0.14
681	0.09	9.54	0.03	0.09	82.74	-0.08	0.13	102.34	0.10
709	0.05	5.36	0.04	0.08	86.41	-0.07	0.11	555.91	0.10

Average	**0.21**	**23.02**	**-0.05**	**0.19**	**59.40**	**-0.15**	**0.18**	**254.83**	**0.10**

The $a_\phi(\lambda)$ retrieval for non-productive inland waters are still a challenge since now few initiatives has been developed to address this issue. Recently, Ogashawara et a. (2016) re-parameterized a QAA for CDOM dominated waters and improved the errors of $a_\phi(\lambda)$ for reasonable levels (NRMSE = 25.90% for Funil reservoir and 29.76% for Itumbiara reservoir). Their approach used an algorithm built to return the spectral features of phytoplankton (Lee et al. 2010) and they also introduced a factor to correct the effect of CDOM in the water column. On the other hand, QAA_{BBHR} used the same approach of Lee et al. (2002) who estimated $a_\phi(\lambda)$ from the subtraction of $a_t(\lambda)$, $a_{CDM}(\lambda)$ and $a_w(\lambda)$ and as result they found an average MAPE of 78.08%, highlighting the limitation of the algorithm in retrieving $a_\phi(\lambda)$ in BB, however, this outcome was better than the previous versions of QAA related to ocean and productive inland waters (LE et al., 2009a, YANG et al., 2013, MISHRA et al., 2014). The QAA_{BBHR} retrieved the lowest error for a_ϕ at 443 and 412 nm, with MAPE of 38.42% and 61.85% respectively, as also observed by Watanabe et al. (2016) who found a MAPE of 32.8% for 443 nm. The success of $a_\phi(\lambda)$ depends on the estimation of $a_t(\lambda)$ and $a_{CDM}(\lambda)$, so in the case of Nav, the low result for $a_{CDM}(\lambda)$ above 50% of average error led to the increase of a_ϕ error. Another issue that might be addressed is the shape of a_ϕ (Figure 5.2), which is not matching with the *in situ* data acquired in laboratory.

Figure 5.2. Spectral shape acquired through (a) QAA_{BBHR} and (b) Nav *in situ* a_ϕ acquired from laboratory analysis. The continuous red line stands for the average spectral a_ϕ from Nav in situ data.

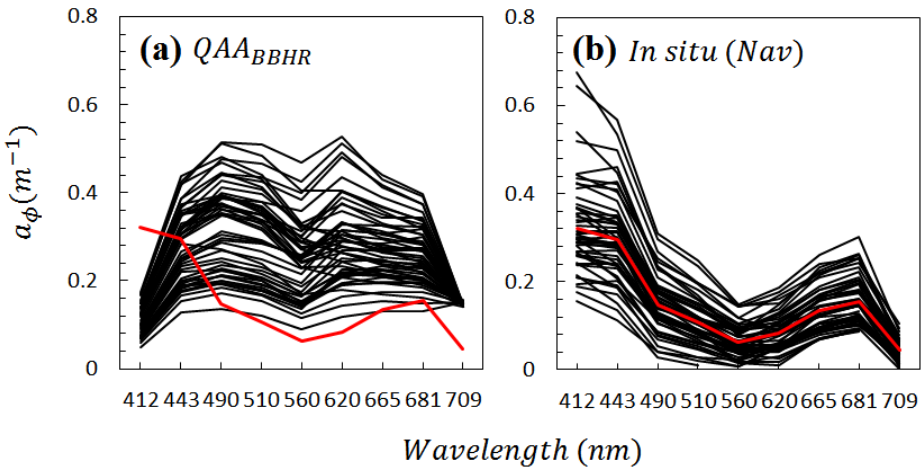

5.4.2 Use of QAA_{OMR} in BB's dataset

Now, analyzing the QAA_{OMR} applied to BB dataset we also observed a good matching between retrieved $a_t(\lambda)$ and *in situ* measurements (Figure 5.3a). The average MAPE was 38.04% and the higher errors were between 443 to 560 nm (41.34 – 47.25%, Table 5.2). For QAA_{OMR} re-parametrization, the average error was 16.35% using Nav's dataset, thus we can see that there was a decline in the $a_t(\lambda)$ performance using data from BB. On the other hand, an improvement was observed at 620 nm showing the second lowest error (30.18%) whilst the opposite was described in QAA_{OMR} parametrization, since at this wavelength the error was considered the highest one with 29.05%. The error at 709 nm retrieved the lowest error (28.80%) and the average bias showed an underestimation trend (-0.14 m^{-1}).

Figure 5.3. Scatter plots in log-scale between measured and estimated $a_t(\lambda)$, $a_{CDM}(\lambda)$ and $a_\phi(\lambda)$ at OLCI spectral bands.

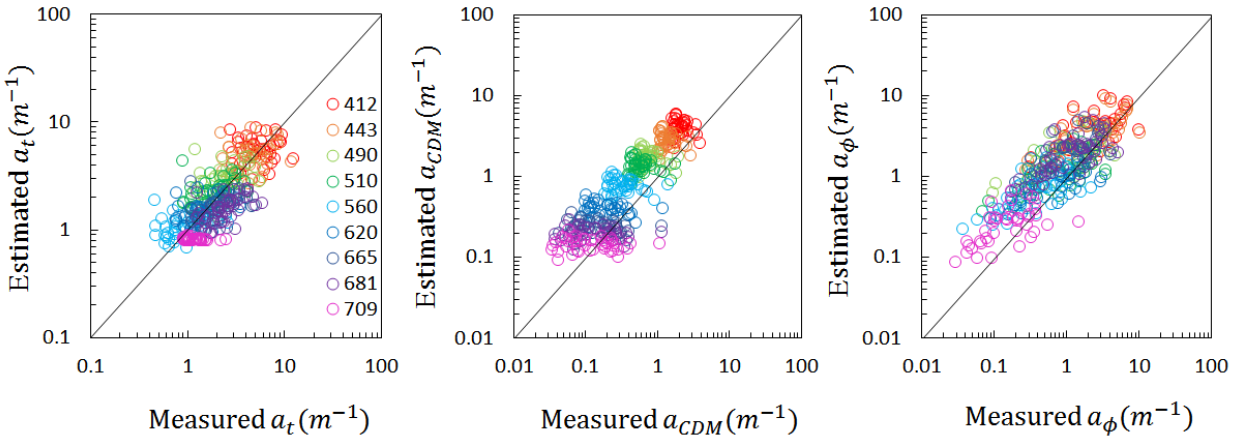

The $a_{CDM}(\lambda)$ retrieval was not satisfactory since the error was above 50% reaching 156.18% at 560 nm, meaning that QAA_{OMR} was not able to retrieve this IOP accurately. This step demanded for huge modifications in both QAA_{OMR} and QAA_{BBHR} models, mainly regarding the band combinations used in empirical steps such as the calibration of ζ and the slope of CDM (S_{CDM}). The first parameter is associated to Chl-*a* concentration or pigment absorption at a specific wavelength and in QAA_{OMR} the band combination was set at the ratio of 443 and 709 nm while QAA_{BBHR} used the band combination ratio between 665 and 709 nm. The nature of both types of waters is totally divergent, BB is phytoplankton matter dominated while Nav is inorganic matter dominated with low Chl-*a* concentration, therefore, the calibration of this step is mandatory in order to fit the model to the water characteristics. The S_{CDM} describes the composition of pigment, dissolved organic matter and detritus (CARDER

et al., 1989, SHANMUGAM et al., 2011) so it is also changeable and must be taken into consideration during $a_{CDM}(\lambda)$ retrieval.

Table 5.3. Comparative band-specific errors related to the IOPs retrieved by QAA_{OMR} based on MAPE (%), RSMD (m^{-1}) and bias (m^{-1}) metrics.

	$a_t(\lambda)$			$a_{CDM}(\lambda)$			$a_\phi(\lambda)$		
Bands (nm)	**RMSD (m^{-1})**	**MAPE (%)**	***bias*** **(m^{-1})**	**RMSD (m^{-1})**	**MAPE (%)**	***bias*** **(m^{-1})**	**RMSD (m^{-1})**	**MAPE (%)**	***bias*** **(m^{-1})**
412	2.48	37.08	-0.06	2.18	98.44	1.87	2.48	119.87	1.26
443	4.69	41.34	0.11	3.25	114.47	1.40	4.51	107.81	0.87
490	1.26	47.25	0.45	1.02	137.73	0.88	1.24	142.38	0.54
510	0.95	45.86	0.32	0.83	143.54	0.70	0.80	103.37	0.10
560	0.49	41.43	0.07	0.49	156.18	0.39	0.48	120.56	0.17
620	0.63	30.18	-0.02	0.26	147.58	0.16	0.68	88.69	0.07
665	1.07	31.91	-0.64	0.20	124.52	0.05	1.24	113.17	0.68
681	1.41	38.53	-1.07	0.19	110.45	0.01	1.32	100.83	0.57
709	0.52	28.80	-0.39	0.18	96.93	-0.02	0.26	112.81	0.06
Average	**1.50**	**38.04**	**-0.14**	**0.96**	**125.54**	**0.61**	**1.45**	**112.17**	**0.48**

For $a_\phi(\lambda)$ retrieval, a new approach was required to estimate this variable in non-productive waters and the base of the model was established by both references Roesler et al. (1989) and Lee et al. (2010), also used by Ogashawara et al. (2016), however with considerable differences. The combination from both references was adopted in order to preserve the a_ϕ shape messed up in the previous QAA versions. As result, the average MAPE found in the original QAA_{OMR} was 46.80% with errors below 50% except for 709 nm. When the model was applied to BB dataset the average error was 112.17% (Figure 5.3c, Table 5.2) and even with this magnitude of error, the shape of a_ϕ (Figure 5.4) was preserved and retrieved only positive values, differently of previous versions. In general, the model was overestimated (bias = 0.48 m^{-1}). The most useful bands used for Chl-*a* and phycocyanin concentration estimation (665 and 709 nm) presented errors of 113.17 and 112.81%, respectively, indicating the limitation of this step in retrieving accurately the $a_\phi(\lambda)$.

Figure 5.4. Spectral shape acquired through (a) QAA_{OMR} and (b) in situ a_ϕ from BB acquired from laboratory analysis. The continuous red line stands for the average spectral a_ϕ from BB in situ data.

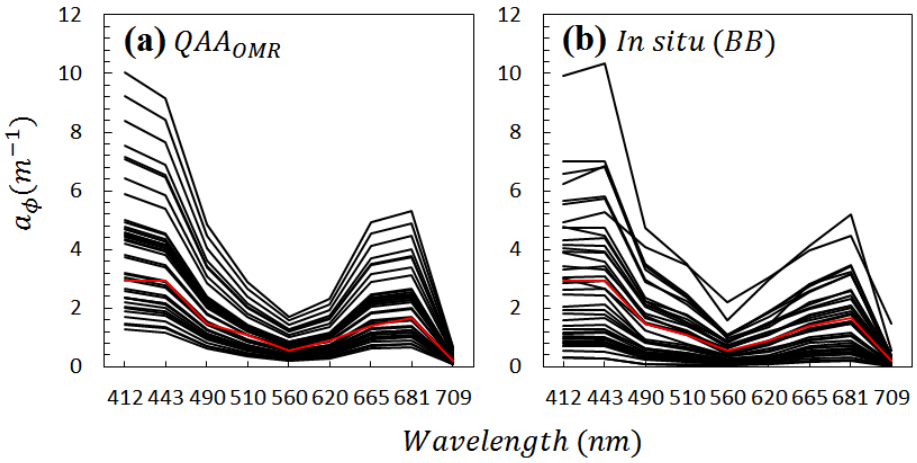

5.4. Conclusion

The results showed that $a_t(\lambda)$ retrieval was not the limiter step in the QAA approaches, returning values with errors (MAPE) below 40%. On the contrary, the following stages demanded for specific adjustments regarding the different water types. In case of Nav, the use of QAA_{BBHR} was successful for $a_{CDM}(\lambda)$ at wavelengths between 412 to 560 nm (MAPE < 50%) and at 443 nm the MAPE was 34.13% highlighting the good performance of the model for this specific dataset and considering that at this wavelength we can also estimate the dissolved organic carbon (DOC) concentration. However, the model was not able for deriving $a_\phi(\lambda)$ specially at 560, 620 and 709 nm with errors exceeding 500%. In addition, another issue was related to the inefficiency in modeling the a_ϕ shape reflecting the limitation of the model.

In case of BB, the QAA_{OMR} increased the error for modeling $a_{CDM}(\lambda)$ reaching 100% in all wavelengths except for 412 and 709 nm (MAPE < 100%), this contretemps was attributed to the need of empirical step calibration, such as the adjustment of both ζ and S_{CDM} according to the water type. As expected, the QAA_{OMR} showed high errors (MAPE > 100%, except for 620 nm that presented and error below 100%) for $a_\phi(\lambda)$ retrieval, however, the model could preserve the shape of *in situ* data, achieving the main objective of Roesler et al. (1989). Overall, both QAA versions could retrieve $a_t(\lambda)$ considering different types of water than the ones used for original parametrization with a slight advantage of QAA_{BBHR}. Therefore, we can assume that a single model can be suitable to estimate at least $a_t(\lambda)$ considering different trophic state waters. On the contrary, more efforts must be carried out for improving the $a_{CDM}(\lambda)$ and $a_\phi(\lambda)$

estimation in order to reduce the errors below 50% considering, for example, the waters from the reservoirs of the cascade system of Tietê River that presents waters ranging from oligo-to-hypereutrophic environments.

CHAPTER 6: LONG-TERM MONITORING OF TOTAL SUSPENDED MATTER IN TROPICAL RESERVOIRS WITHIN A CASCADE SYSTEM WITH WIDELY DIFFERING OPTICAL PROPERTIES

6.1 Introduction

Total suspended matter (TSM) consisting of both organic and inorganic matter is one of the most important indicators of water quality in inland waters. TSM induced turbidity has a deleterious effect on light propagation through the water column affecting the primary production (SHEN et al., 2010), besides, it plays a crucial role in the transportation of nutrients and contaminants by adsorption (WU et al., 2013). The degradation of inland waters has been widely discussed by the scientific community and is considered a public order issue (PANIGRAHI et al., 2009). The monitoring of the water quality via usual field techniques demands efforts and high cost, besides a holistic panorama is difficult to achieve by applying common field techniques (SONG et al., 2012). Satellite images have been used in water quality monitoring since 1978 with the availability of data from Coastal Zone Color Scanner (CZCS) on board of NIMBUS 7 designed to provide ocean color data (EVANS and GORDON, 1994). Since then, many studies (MOORE et al., 1999; MILLER and MCKEE, 2004; SHEN et al., 2010; TARRANT et al., 2010; MISHRA and MISHRA, 2010; WANG et al., 2012; SHI et al., 2015; KUMAR et al., 2016) have been conducted in order to retrieve TSM concentration using the next generation ocean color sensors such as Sea-Viewing Wide Field-of-View Sensor (SeaWiFS) and the Moderate Resolution Imaging Spectroradiometer (MODIS) from the National Aeronautics and Space Administration (NASA) and the Medium Resolution Imaging Spectrometer (MERIS) from the European Space Agency (ESA).

The high temporal and spectral resolution of MODIS (TERRA and AQUA) sensor has enabled the scientific community to develop numerous models over the years to retrieve TSM concentrations. Miller and McKee (2004) demonstrated the utility of MODIS Terra band 1 (645 nm) surface reflectance data for estimating TSM concentration and studying the transport of materials in coastal environments. Wang et al. (2012) also found a robust linear relationship between MODIS band 1 and TSM concentration (R^2 = 0.95, RMSE = 0.51 mg l^{-1}) in Bohai Sea of China and highlighted the strong performance of this model for monitoring the transport of materials in small water bodies. Shi et al. (2015) obtained a reasonable correlation using an exponential calibration function between MODIS Aqua band 1 and TSM (R^2 = 0.70, RMSE = 14.3 mg l^{-1}) for Lake Taihu (China), which is a turbid environment (TSM ranging from 15.8 to 218.6 mg l^{-1}). Kumar et al. (2016) re-parametrized three variants of Miller and McKee (2004)

model using MODIS 250 m data and accurately retrieved TSM concentration between the range of 6.5 to 200 mg l^{-1} for the Asia's largest brackish water estuary, Chilika Lagoon. On the contrary, Tarrant et al. (2010) found a weak relationship (R^2 = 0.28) between MODIS band 1 and TSM in several southwestern United States (US) lakes (TSM ranging between 0.30 – 20.0 mg l^{-1}) and included band 2 (858 nm) which significantly enhanced the model performance (R^2 = 0.82 and RMSE = 1.67 mg l^{-1}). Wu et al. (2013) applied this band combination to estimate TSM concentration in Poyang Lake, China, and their model explained 76% of TSM variance.

Other empirical and semi-empirical models such as band ratios have also provided suitable estimates of TSM. Tang et al. (2013) found that $R_{rs}(560)/R_{rs}(490)$ presented a good relationship for low TSM (R^2 = 0.74) concentrations (< 3.0 mg l^{-1}) and $R_{rs}(681)/R_{rs}(560)$ worked well for high TSM values (R^2 = 0.80). Han et al. (2006) developed a model using bands at 550 nm and 670 nm for Yangtze River estuary where phytoplankton and yellow substances were the main factors that control the water reflectance. These wavelengths are sensitive to suspended sediment and their combination may reduce the effect of the chlorophyll (Chl-*a*). Zhang et al. (2010) also developed a model that exploited these two spectral regions and they emphasized that the green and red bands are sensitive to TSM variations in waters with a wide range of turbidity regime.

As previously mentioned, MODIS data is widely used to estimate TSM concentrations in inland waters with different limnological and environmental conditions, thus some aspects are already consolidated. The TSM spectral behavior is noticeable in the visible to near-infrared (NIR) wavelengths showing a strong correlation in the red wavelength (MILLER and MCKEE, 2004; HAN et al., 2006; CUI et al., 2013; KUMAR et al., 2016). An increase in TSM concentration shifts the reflectance peak towards longer wavelength in the visible spectrum (HAN et al., 2006). Odermatt et al. (2012) also observed that the reflectance peak position is affected by the TSM concentration and the band at 555 nm is appropriate to retrieve concentrations below 30 mg l^{-1} (ELEVELD et al., 2008) and the band at 670 nm is more suitable for higher concentrations (HAN et al., 2006).

In addition to the empirical models (MILLER and MCKEE, 2004, HAN et al., 2006), TSM can also be retrieved using semi-analytical or semi-empirical models that relate the inherent optical properties (IOPs) and the water constituents, combined with some empirical steps (DEKKER et al., 2001; DOXARAN et al., 2002; CARDER et al., 2004; ZHANG et al., 2010). To estimate the TSM concentration in Frisian lakes, Netherlands, Dekker et al. (2001) used analytical optical modelling based on *in situ* IOPs and satellite images. They highlighted

the limitation of the model to estimate TSM > 40 mg l^{-1} due to saturation of the reflectance. Doxaran et al. (2002) developed an experimental method for determining TSM concentration in highly turbid waters (ranging between 35 – 2,000 mg l^{-1}) in Gironde estuary, France. They found an accuracy of ± 35% for concentrations up to 2000 mg l^{-1}. Nechad et al. (2010) calibrated and validated a generic algorithm for TSM retrieval in turbid waters, which was developed to be applied to any ocean color sensor such as MODIS, MERIS and SeaWiFS. The relative error for calibration was less than 30% in the spectral range 670 – 750 nm and for validation; the error was less than 40%. The semi-analytical models may show a performance advantage over empirical models, however, they need many *in situ* measurements, such as absorption (*a*) and backscattering (b_b) coefficients, remote sensing reflectance (R_{rs}), TSM, Chl-*a*, CDOM and so forth, which makes the practical application difficult (WANG et al., 2012). On the other hand, empirical models do not need IOPs thus could be readily applicable and operational.

Current monitoring and water quality management protocol in Nova Avanhandava (Nav) and Barra Bonita (BB) reservoirs situated in Southeast of Brazil, is primarily based on *in situ* collections, which can be very expensive and time consuming. It leads to a scarcity of dense temporal water quality data necessary to track the trend in water quality for effective management actions. Both reservoirs belong to the cascade system of Tietê River consisting of six reservoirs. In addition, due to the long extension of Tietê River that crosses the State of São Paulo from East to West (1.150 km) under many different land use and land cover (LULC) settings, it is extremely challenging to monitor the water quality from these reservoirs via traditional methods. Therefore, the use of remote sensing based approach is of topmost importance allowing frequent spatio-temporal monitoring with very low cost. According to Smith et al. (2014), the water quality is highly affected by this cascade setting leading to intense eutrophication in the first reservoir (BB) followed by a gradual change in trophic status from meso-oligotrophic waters.

Several studies have shown that many empirical and semi-empirical models perform satisfactorily in a single or few similar turbid water environments, however, their performance drops significantly when data from different reservoirs in a cascade system ranging from oligo-to-eutrophic environments are used together. Most of them tend to overestimate at low concentration. For that reason, this study was aimed at assessing the performance of different well-established models designed to retrieve a wide-range of TSM concentration. The performance of these models was compared to two separate model calibrated to monitor the spatio-temporal variability of TSM in two oligo-to-eutrophic tropical reservoirs, Nav and BB,

situated in the cascade system of São Paulo State, Brazil. In addition, the environmental forcing affecting the water quality in these reservoirs was examined based on the performance of these models. The long-term spatio-temporal monitoring of these reservoirs has not been done before, which is a novel aspect of this study. The continued degradation of water quality in Brazilian reservoirs has been a cause for concern, and this study lays the foundation for a regular monitoring protocol which can be used to decode the environmental forcing at play.

6.2 Data and Methods

6.2.1 Field data

The field trips occurred in two periods of the year, one coinciding with the beginning of the dry season (Nav1: April 28 – May 2 and BB1: May 5 – 9, 2104) and the other corresponding to the end of the dry season (Nav2: September 23 – 26 and BB2: October 13 – 16, 2014). A total of 63 *in situ* TSM samples and radiometric measurements were collected from both Nav and BB reservoirs, of which 50 samples were used for calibration and 13 for validation (see Figure 2.1 for sampling stations). These 13 samples were selected as validation dataset because matched with MODIS Terra images overpass. Water samples were collected just below the air-water interface and to determine TSM concentration using the method described by APHA (1998). Water samples were filtered on the same day of collection through pre-ashed and pre-weighed Whatmam fiberglass GF/F filter with a nominal porosity of 0.7 μm and then stored at low temperature in the refrigerator (-25°C) until analysis. The filters were dried in the oven at 100° C for 12 h, and then weighed using an analytical balance. The Chl-*a* was extracted with 90% acetone solution and analyzed spectrophotometrically (GOLTERMAN et al., 1978).

6.2.2 Remote sensing reflectance (R_{rs})

R_{rs} spectra were estimated from radiometric measurements taken between 10 am to 2 pm local time. This procedure was carried out in order to maintain a consistent acquisition geometry based on the time window of light availability (MOBLEY, 1999). At each sample station, below and above water radiometric data were acquired using RAMSES TriOS® (TriOS, Germany) hyperspectral radiometers operating in the spectral range between 400 – 900 nm. The radiance sensor was equipped with a 7º field-of-view and the irradiance sensor is equipped with a cosine collector. The two radiance sensors positioned above water surface measured the total

upwelling radiance ($L_t(\lambda)$; W m^{-2}nm^{-1}sr^{-1}) i.e., the upward radiance from the water surface and the incident sky radiance ($L_s(\lambda)$; W m^{-2}nm^{-1}sr^{-1}) i.e., the incoming light from the sky (Figure 6.1a). The irradiance sensor measured the downwelling irradiance ($E_d(\lambda)$; W m^{-2}nm^{-1}) i.e., the incident light onto the water surface. The single radiance sensor positioned inside the cage measured the upwelling radiance ($L_u(\lambda)$; W m^{-2}nm^{-1}sr^{-1}), while the irradiance sensors measured the upwelling irradiance ($E_u(\lambda)$; W m^{-2}nm^{-1}) and the downwelling irradiance ($E_d(\lambda)$; W m^{-2}nm^{-1}). The instruments above water surface were positioned on a steel frame and the L_t sensor was set with a viewing angle of 40º from nadir and an azimuth of 135º (oriented from the sun), and the L_s sensor was set with the same angles, 40º from zenith and 135^0 azimuth (Figure 6.1).

Figure 6.1. Schematic diagram showing the (a) viewing angle (θ_v) of the sensors to avoid specular scattering (Mobley, 1999) (b) Geometry of the sensor relative to the sun used for radiometric measurements, represented by zenith (θ_s), azimuthal (ϕ) and nadir ($\hat{n}$) angles, (c) sensors collecting total upwelling radiance $L_t(\lambda)$, the incident sky radiance $L_s(\lambda)$ and the downwelling irradiance $E_d(\lambda)$, (d) sensors collecting upwelling radiance $L_u(\lambda)$, upwelling irradiance $E_u(\lambda)$ and the downwelling irradiance $E_d(\lambda)$.

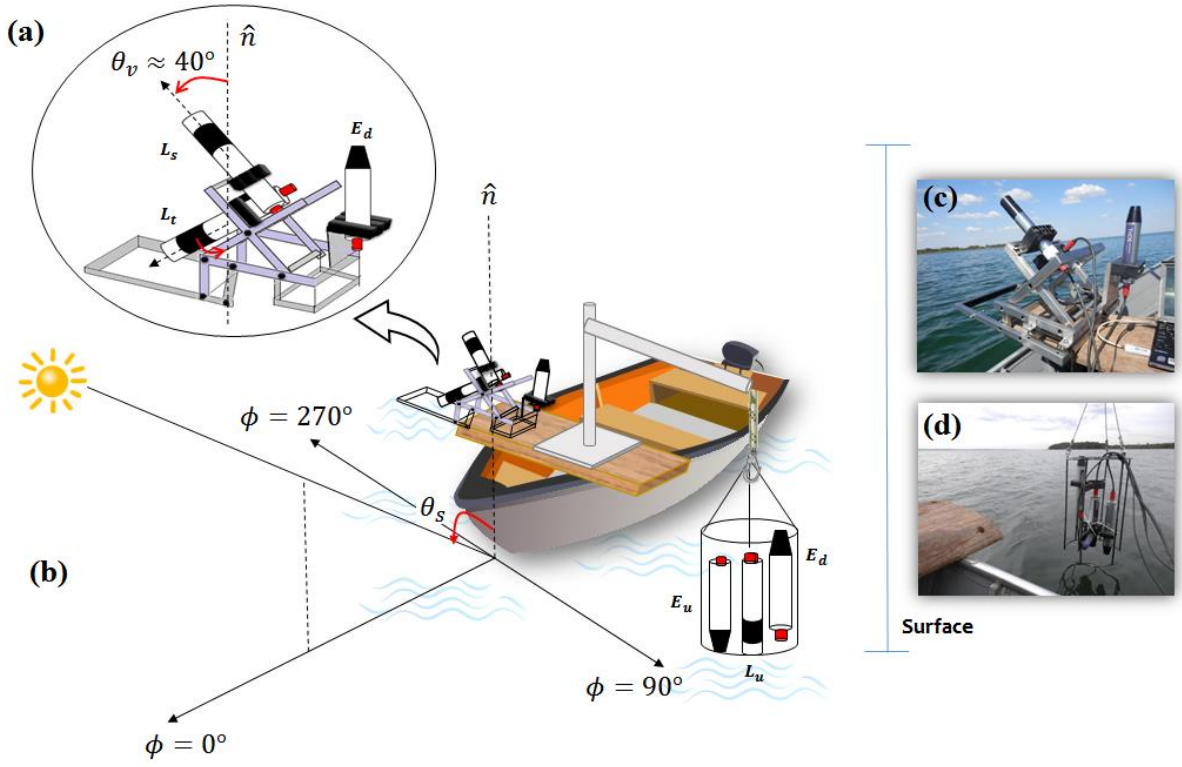

All radiometric quantities were linearly interpolated to transform the original spectral resolution of ~ 3.3 nm to 1 nm. This procedure was designed to homogenize RAMSES

measurements between the sensors with different bandwidths and band centers. This technique does not affect the shape or magnitude of the spectral curves (FAN, 2014). The acquisition geometry follows the protocol described by Mueller (2000) and Mobley (1999) and aimed at meeting requirements to avoid the effects of radiance and specular boat shading. The *in situ* remote sensing reflectance ($R_{rs}(\lambda)_{field}$) (sr^{-1}) was calculated from the radiometric profiles according to Mobley (1999), Equation 4.1.

R_{rs} is the input data for models to retrieve the OSCs concentration, however, it is necessary to match the hyperspectral data with those from satellite data by simulating the satellite sensor's bands using the spectral response function *S*(λ) of the *i*th spectral band (GORDON, 1995; BARNES et al., 1998). In our study, MODIS Terra 250m and 500m bands were simulated according to equation 4.2.

6.2.3 Inherent Optical Properties (IOPs)

Water samples were filtered through a 0.7 μm porosity GF/F fiberglass filter that was stored flat under freezing condition. The determination of the total particulate (algal and non-algal) absorption coefficient (a_p) was acquired by using an integrating sphere module presented in the double-beam Shimadzu UV-2600 UV-Vis spectrophotometer (Shimadzu, Japan), with spectral sampling from 280 nm to 800 nm. A white filter wetted with ultrapure water was used as reference. The filter containing the particulate was positioned in the integrating sphere to measure the optical density (OD). The T-R (Transmittance-Reflectance) method presented by Tassan and Ferrari (1995, 1998) was employed to obtain a_p. To acquire the phytoplankton (a_ϕ) and non-algal particle (a_{NAP}) absorption coefficients, the filter underwent depigmentation by oxidation in 10% sodium hypochlorite (NaClO), ensuring that the sample does not contain any pigment interference. Using empirical relationships described by Tassan and Ferrari (1995, 1998) the respective coefficients were determined, and to retrieve a_ϕ, the OD of the total particulate was subtracted by the non-algal particle (NAP) fraction.

To estimate the colored dissolved organic matter (CDOM) absorption coefficient (a_{CDOM}), water samples were filtered through a fiberglass Whatman GF/F with 0.7 μm pores, and then re-filtered under low vacuum pressure using a Whatman nylon membrane filter with 0.2 μm pores. The readings were acquired using the absorbance mode and the samples were placed in 10 cm quartz cuvettes. For each set of measurements, a reference reading containing Milli-Q water was performed, and for each sample (DO_{sample}), the reference absorbance value

was subtracted ($DO_{reference}$). The measured optical densities (DO_{sample}) were converted to absorption coefficient multiplying by 2.303 and dividing by the path length (l = 0.1 m for a 10 cm cuvette). Hence, the $a_{CDOM}(\lambda)$ (m^{-1}) was calculated according to equation 3.2.

6.2.4 Satellite Data and Processing

MODIS sensor on board Terra platform (MODIS/Terra) has been providing images since 1999. The orbit is near polar Sun-synchronous and it crosses the equator every 10:30 am local solar time. In addition, in 2002 another platform, MODIS sensor Aqua (MODIS/Aqua) was launched providing afternoon images (1:30 pm equator crossing time) (BARNES et al., 2003). Both satellites offer data in 36 spectral bands ranging from 0.4 μm to14.4 μm with a spatial resolution of 250 m (1 – 2 bands), 500 m (3 – 7 bands) and 1 km (8 – 36 bands) (BARNES et al., 1998). MODIS land surface reflectance products (250 m MOD09GQ and 500 m MOD09GA from Terra) are daily Level 1B product, geo-located and corrected for atmospheric gases and aerosols providing surface reflectance (SR) (VERMOTE and KOTCHENOVA, 2008; DOXARAN et al., 2009; VERMOTE et al., 2011). In particular, MODIS band 1 (640 – 670 nm) has been widely employed to map the TSM concentration in inland and coastal waters (e.g., MILLER and MCKEE, 2004, ZHANG et al., 2010, CUI et al., 2013, PARK and LATRUBESSE, 2014, KUMAR et al., 2016).

Both Terra and Aqua products are set to Sinusoidal projection and HDF-EOS format, thus a re-projection process was established to convert into geographical coordinate system (Datum: WGS 84) using SeaWiFS Data Analysis System – SeaDAS 7.2. The images from MODIS/Terra were acquired instead of MODIS/Aqua because of the lack of coincident *in situ* data for Aqua (U.S. Geological Survey; http://earthexplorer.usgs.gov/). The daily SR products (MOD09) were simulated based on the SRF, previously mentioned and used in the model calibration. This process was employed because the MODIS/Terra images acquired during field data collection were covered by clouds making it impossible build matchups between *in situ* and satellite data. However, the validation process was carried out using MOD09 SR data. This product corresponds to the water surface reflectance (R) and can be converted to water surface remote sensing reflectance ($R_{rs_{sat}}$) dividing it by π (WANG et al., 2015).

In order to increase the possibilities of using more spectral bands (MOD09GA) with a better spatial resolution (MOD09GQ), a downscaling method was implemented to resample the 500 m MODIS SR to 250 m MODIS SR (CHEN et al., 2015). Thereby, a resampling using

bilinear interpolation was applied as described in Srichandan et al (2015) and the correlation between 500 m and 250 m MODIS SR bands was verified. The downscaling process was carried out in SeaDAS. Land and clouds were masked out using band 2 as proposed by Miller & McKee (2004) with an empirical threshold algorithm.

6.2.5 Bio-optical model calibration and validation

The simulated bands from MODIS/Terra ($R_{rs_{sim}}$) were applied as input to the empirical models used to estimate the TSM concentration (Table 6.1). Samples collected in the field were compared with the $R_{rs_{sat}}$ from MODIS/Terra images of the same day and after visual examination, five valid daily images were used. Numerous existing models broadly developed for inland and coastal waters were employed in this research to analyze their performance in the oligo-to-mesotrophic cascade reservoirs.

Table 6.1. TSM empirical models: model fit, TSM concentration range (mg l^{-1}), and geographic location.

Author (s)	**Bands (nm)**	**Model Fit**	**TSM range (mg l^{-1})**	**Location**
Miller and McKee (2004)	645	Linear	0 – 60	Lake Pontchartrain, USA
Hu et al. (2004)	645-859	Exponential	2– 11	Tampa Bay, USA
Liu et al. (2006)	$(645-859)/(645+859)$	Linear	23.4 – 61.2	Middle Changjiang River, China
Sipelgas et al. (2006)	645	Linear	3 – 10	Pakri Bay, Finland
Kutser et al. (2007)	645	Linear	2 – 8	Muuga and Silanamae Port, Estonia
Chen et al. (2009)	859/645	Polynomial	1.29 – 208	Apalachicola Bay, USA
Bi et al. (2011)	645/555	Exponential		Southern Bohai Strait, China
Doxaran et al. (2009)	859/645	Exponential	77 – 2182	Gironde Estuary, France
Jiang et al. (2009)	859	Logarithmic	0 – 170	Taihu Lake, China
Tarrant et al. (2010)	645-859	Linear	0.3 – 20	USA Lakes
Wang et al. (2010)	859/645	Linear	1 – 64	Apalachicola Bay, USA
Petus et al. (2010)	645	Polynomial	0.3 – 145.6	Bay of Biscay, France
Zhao et al. (2011)	645	Exponential	0 – 87.8	Mobile Bay Estuary, Alabama
Chen et al. (2011a)	859/645	Polynomial	1.3 – 208	Apalachicola Bay, USA
Chen et al. (2011b)	859/645	Linear	1.3 – 208	Apalachicola Bay, USA

Ondrusek et al. (2012)	645	3rd order Polynomial	4.5 – 14.9	Chesapeake Bay, USA
Wang et al. (2012)	645	Linear	0.2 – 12	Bohai Sea, China
Cui et al. (2013)	645	Exponential	0 – 141.9	Poyang Lake, China
Villar et al. (2013)	859/645	Power	25 – 622	Madeira River, Brazil
Wu et al. (2013)	645-859	Exponential	0 – 173.3	Poyang Lake, China
Fan et al. (2014)	650/420	Linear	7.1 – 64.8	Patuxent River, USA
Feng et al. (2014)	645	Exponential	< 50	Yangtze Estuary, China
	859/645	Exponential	> 50	
Chen et al. (2015)	859/645	Polynomial	5.8 – 577.2	Estuary and Coast of China
Shi et al. (2015)	645	Exponential	1.7 – 343.9	Taihu Lake, China
Kumar et al. (2016)	645	Polynomial	6.5 - 200	Chilika Lagoon, India
Breunig et al. (2016)*	645	Exponential	Annual mean 7.56 (US), 733 (MS), 4.48 (LS).	Passo Real Reservoir, Brazil

* UP: upper stream, MS: middle stream and LS: lower stream.

These models were chosen due to their simplicity and the wide use in different environments. Variants of the respective models based on linear, exponential, power, quadratic and logarithmic fits were performed during calibration with least-squares technique. The best relationship between the models and the TSM data collected in the field was validated. Outliers were initially analyzed based on boxplots and then removed from the original Nav dataset (below 0.10 and above 1.45 mg l^{-1}) to avoid incorrect analysis. Data from each study site were then calibrated ($n_{BB} = 30$ and $n_{NAV} = 20$ samples) with the $R_{rs_{sim}}$ measures and validated ($n_{BB} = 8$ and $n_{NAV} = 5$) separately using the $R_{rs_{sat}}$ values. A mixed dataset was also calibrated (n = 50) and validated (n = 13) in order to assess the performance of a single model to represent the TSM variability in the two widely different study sites.

The evaluation of the re-parameterized TSM algorithms was carried out using statistical indicators such as root mean square error (RMSE), mean bias error (MBE), normalized root mean square error (NRMSE) and the coefficient of determination (R^2). The indices are therefore defined according to Equations (4.4), (5.1) and (6.1) respectively:

$$NRMSE = \frac{RMSE}{\Delta x_{meas}} \times 100 \tag{6.1}$$

where $x_{meas,i}$ is related to the estimated and measured values.

6.3 Results

6.3.1 Long-term spatio-temporal monitoring

The long-term analysis of both reservoirs was carried out for 16 years (2000 – 2015) for the months of May and October, representing the beginning and end of the dry season. At least four TSM maps were generated each month using the MODIS 8-day composite images, and for each year two composite images were chosen to represent the months of May and October. Images collected in the same week and with no radiometric problem over the study sites were the criteria to choose the images. A total of 128 images were used and 32 images were chosen to represent the spatial-temporal variability of TSM at the study sites. The MODIS/Terra 8-day products correspond to Level 3 data and contain the best possible observation during the eight days, including the absence of clouds or cloud shadows and aerosol loading (available in https://lpdaac.usgs.gov/). Five locations for Nav and eight locations for BB were extracted from each of the 16 TSM maps for developing the boxplot representing the spatial variability. The selected locations were representative of each part of the reservoirs and additional care was taken to avoid spurious values such as null pixels.

6.3.2 Water quality characterization

The distribution of TSM concentration (Figure 6.2) in both reservoirs was highly discrepant due to the water quality differences between them. A significant majority (46.7%; n = 30) of the samples collected from BB had TSM values ranging from 16 to 26 mg l^{-1}, whereas, most of the samples from Nav (38.46%; n = 26) presented TSM values ranging from 0.6 to 1.0 mg l^{-1}.

Figure 6.2. Cumulative percentage of TSM concentration and the respective frequency of the calibration dataset from BB (a) and Nav (b) reservoirs.

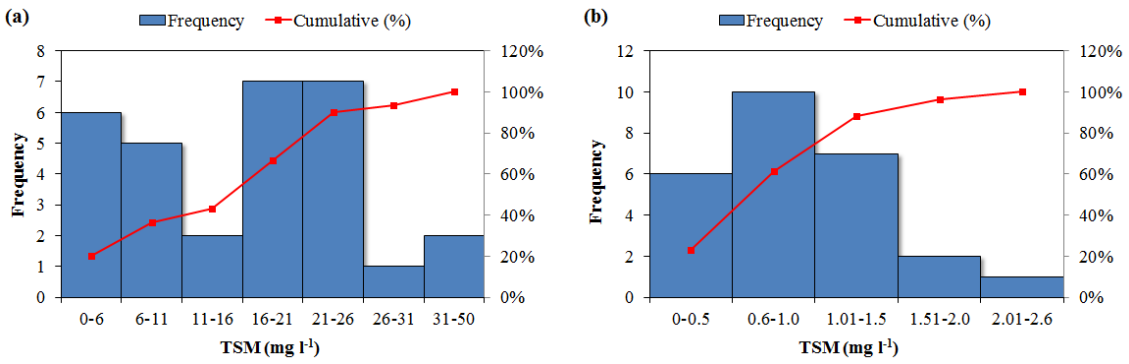

Based on the *in situ* data collected in the field (Table 6.2), the average Chl-*a* value in BB were much higher in October 413.20 mg m^{-3} than in May 133.96 mg m^{-3} compared to NAV where the average Chl-*a* did not exceed 7 mg m^{-3} in either seasons. In addition, Nav exhibited very low TSM values with an average of approximately 1 mg l^{-1} compared to BB where it showed significant seasonal variability with mean TSM of 7.40 mg l^{-1}in May and 21.91 mg l^{-1} in October.

Table 6.2. Descriptive statistics of environmental dataset in both reservoirs.

		Nav1 (Apr/May) (n = 17)	**Nav2 (Sep)** (n = 14)	**BB1 (May)** (n = 19)	**BB2 (Oct)** (n = 19)
Chl-*a* **(mg g^{-3})**	Min - Max	2.46 - 12.56	4.51 - 9.42	51.33 - 293.24	263.20 - 797.80
	Mean	6.48	6.94	133.96	413.20
	SD	2.52	1.59	62.65	138.01
TSM **(mg l^{-1})**	Min - Max	0.10 - 2.60	0.50 - 1.20	3.80 – 16.30	10.80 – 44.00
	Mean	1.01	0.81	7.40	21.91
	SD	0.62	0.20	3.15	7.04
Chl-*a*:TSM **(µg/mg)**	Min - Max	2.47 - 68.26	4.75 - 18.57	10.27 - 28.81	12.93 - 34.99
	Mean	11.49	9.18	18.84	19.56
	SD	15.63	3.66	6.18	5.65
Depth **(m)**	Min - Max	5.30 - 29.60	-	10.00 - 30.00	8.00 - 18.5
	Mean	16.37	-	15.33	12.96
	SD	7.96	-	4.18	2.80
Secchi Disk **(m)**	Min - Max	2.29 - 4.80	2.45 - 4.65	0.80 - 2.30	0.37 - 0.78
	Mean	3.13	3.35	1.47	0.56
	SD	0.66	0.56	0.42	0.09
Wind speed **(m s^{-1})**	Min - Max	2.00 - 6.40	0 - 5.60	0.80 - 4.90	0 - 5.00
	Mean	3.65	2.91	1.91	1.46
	SD	1.31	2.15	1.03	1.52

Overall, BB exhibited the characteristics of a eutrophic-hypereutrophic environment and Nav of an oligo-to-mesotrophic environment (RODGHER et al., 2005; DELLAMANO-OLIVEIRA et al., 2007). The TSM and Chl-*a* values showed a decreasing trend from BB to Nav and the concentration magnitude was affected by the rainfall rate (Figure 2.3) which remained low during the beginning of the dry season and increased near the end of the dry season. The Ch-*a*:TSM ratio exhibited low values in Nav compared to BB indicating the dominance of suspended matter in Nav and dominance of phytoplankton in BB.

The Chl-*a* showed a strong linear relationship (Figure 6.3) with TSM in BB (R^2 = 0.77, $p < 0.05$, n = 38) and poorly correlated in Nav (R^2 = 0.10, $p > 0.05$, n = 31). It indicated that the TSM in BB is mostly algal turbidity and organic in nature, whereas, mostly inorganic in Nav. In Nav, due to the low suspended sediment, the water was more transparent reaching a maximum Secchi depth of 4.80 m and a minimum of 2.29 m during the first field campaign. A maximum Secchi depth of 2.30 m was observed during first field campaign in BB and a

minimum of 0.40 m during second field campaign. Overall, the biogeochemical data presented in Table 2 and Figure 4 signifies the extreme variability observed between the two reservoirs, which makes the MODIS based TSM empirical model calibration a unique and challenging task.

Figure 6.3. Relationship between TSM (mg l^{-1}) and Chl-*a* (mg m^{-3}) in (a) BB and (b) Nav.

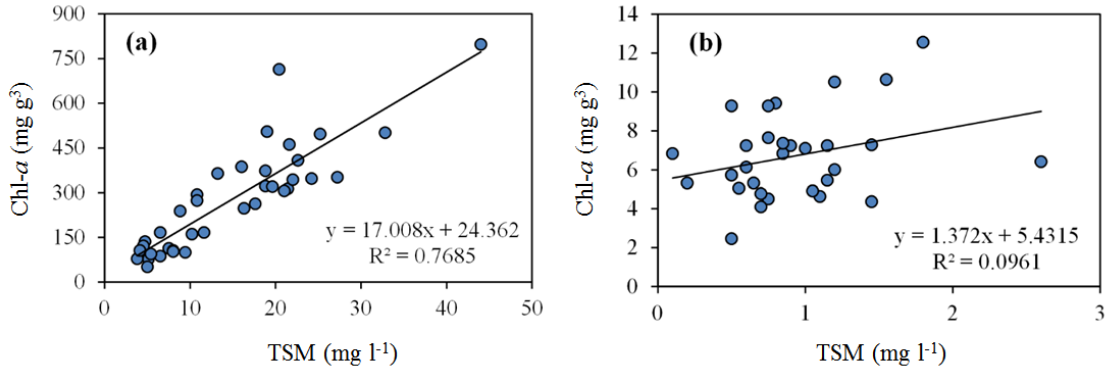

6.3.3 Bio-optical properties description

The IOPs provide information about the contribution and dominance of certain OSC in the water and can also assist in the estimation of these components using proper algorithms (MISHRA et al., 2014; RIDDICK et al., 2015). As expected, the most dominant OSC in BB was found to be phytoplankton with an average contribution of 68.19 %, 66.76 %, and 79.85 % at 443, 555, and 645 nm, respectively (Figure 6.4). In Nav, the dominance of one single OSC was not observed, and at 443 nm the CDOM dominated the total absorption coefficient except the water component (a_{t-w}) with 37.36 % followed by NAP with 46.78 % at 555 nm and 39.65 % at 645 nm.

Figure 6.4. Ternary graphs depicting the absorption budget at three wavelengths in the visible region (a) blue – 443 nm, (b) green – 555 nm and (c) red – 645 nm.

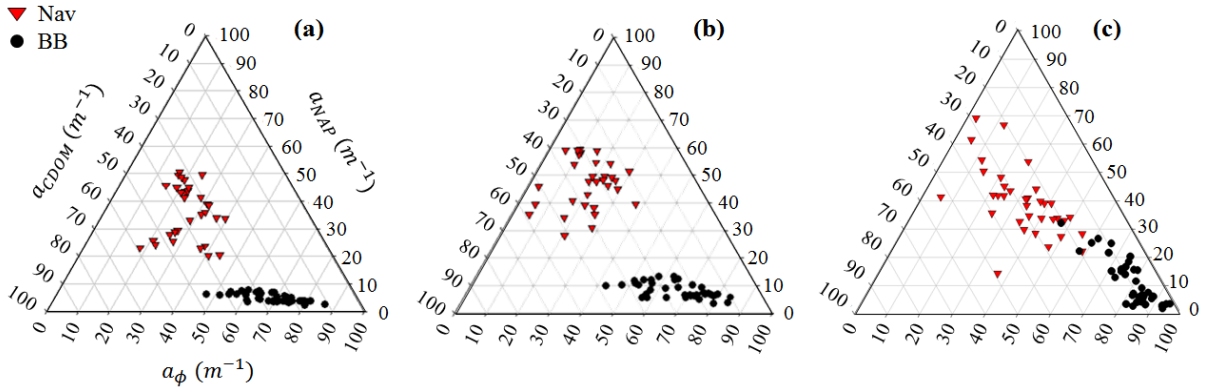

At 443 nm, the Nav samples were spread within the central zone of the ternary plot indicating that all three absorption coefficients co-varied somehow. The predominance of a_{ϕ} in BB reservoirs at 645 nm was expected and is considered as a typical diagnostic feature of phytoplankton, however, unlike BB, the feature at the blue region was not detected in Nav, possibly due to the low concentration of this OSC and the predominance of another component such as CDOM (Figure 6.4a). Wu et al. (2011) reported a similar observation in the data from Poyang Lake, China, which showed an absorption peak at 675 nm, but did not show any sign of absorption between 430 – 450 nm. They attributed this to the low concentration of phytoplankton. Doxaran et al. (2006) also noticed the same pattern in Tamar estuary, UK. These ternary graphics reiterated the fact that both study sites are optically different and the data from BB were tightly clustered with low variability while Nav data were highly scattered indicating a complex interplay of contribution of OSCs to the total absorption budget.

$R_{rs}(\lambda)_{field}$ spectra at various TSM concentrations between 0.5 mg l^{-1} to 32.8 mg l^{-1} were analyzed with respect to the MODIS/Terra SR for bands at 469, 555 and 645 nm (Figure 6.5). The spectra with 0.5, 1.2 and 2.6 mg l^{-1} (dashed lines) represent the data from Nav and the rest represent BB (solid lines). The shape and magnitude changed drastically with increasing TSM concentration. The three spectra from Nav assumed a flatter feature along the blue region with the presence of a peak between 500 – 600 nm highlighting the influence of inorganic matter (NOVO et al., 1991). The same result was also described in Nascimento (2010) studying the Itumbiara Reservoir, Brazil, showing the dominance of detritus (60%) and Chl-*a* (40%) in the total absorption budget. The spectra represented by the 5.0 mg l^{-1} concentration, also showed a flatter pattern along the blue to green wavelengths and a peak between 500 – 600 nm, however, new features raised in the red region depicting the presence of a_{ϕ} approximately at 675 nm;

and a $R_{rs}(\lambda)_{field}$ peak between 700 – 725 nm, also highlighting the presence of Chl-*a*. The magnitude of the $R_{rs}(\lambda)_{field}$ spectra showed a systematic increase with TSM concentration and at concentrations higher than 10.78 mg l^{-1}, the spectra showed signs of algal turbidity in terms of phytoplankton interaction such as the absorption maxima at 675 nm and minima at 708 nm (MISHRA and MISHRA, 2012). At high concentration, i.e., at 32.8 mg l^{-1}, it also showed a cyanobacteria signature with a characteristic absorption feature at 620 nm and a reflectance peak at 650 nm (MISHRA et al., 2009; MISHRA et al., 2013). Spectral features were absent over 750 nm in Nav indicating that the backscattering from other OSC was not present. On the other hand, in BB is very clear that light was backscattered by other OSCs.

Figure 6.5. $R_{rs}(\lambda)_{field}$ spectra representing different TSM concentrations overlapped with MODIS Terra spectral response function for bands at (A) 469 nm, (B) 555 nm and (D) 645 nm.

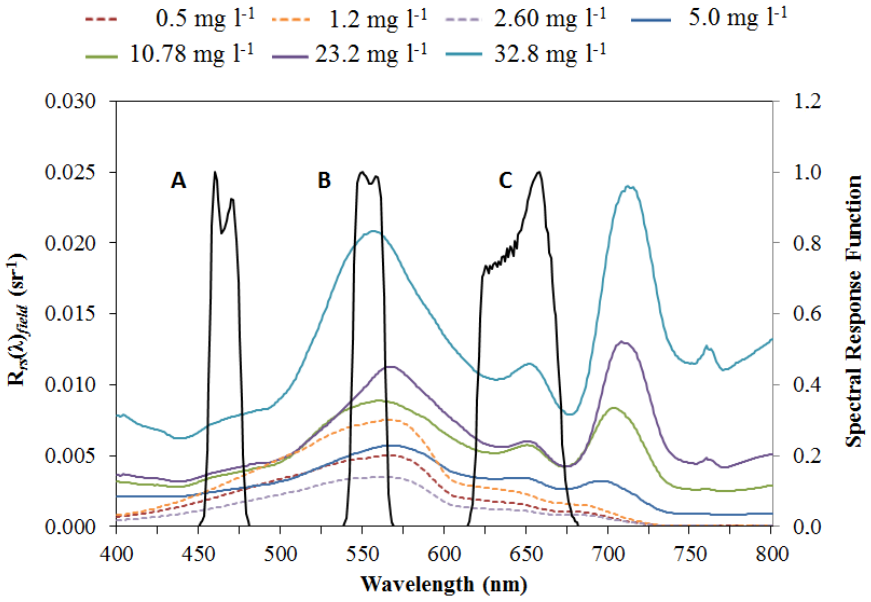

The feature at 645 nm corresponding to MODIS band 1 described different behavior for Nav and BB. As illustrated in Figure 6.4(c), in Nav, detritus contributed with ~40% to the total absorption budget, while in BB, phytoplankton contributed with ~80% justifying the appearance of a shoulder in approximately 645 nm followed by a reflectance peak at 650 nm.

6.3.4 Downscaling MODIS image procedure

MODIS MOD09GA 500 m data from bands 3 to 7 (center bands at: 469, 555, 1240, 1640 and 2130 nm, respectively) were resampled to 250 m based on MOD09GQ product in

order to increase the spatial resolution of bands 3 – 7 used in the calibration process. The bilinear interpolation method was applied aiming to divide the 500 m pixel into four 250 m pixels. Relationship between the downscaled MODIS 500 m data and the original MODIS 500 m was verified in order to assure that after resampling procedure, the pixels still represent the spectral characteristic of the respective bands. A strong correlation ($R^2 = 0.96$. p-value < 0.05) was observed between downscaled MODIS 500 m (band 3) and the original MODIS 500 m (band 3) related to May, 2014 associated to the first field dataset (Figure 6.6). The same result was also observed for band 3 related to October, 2014 corresponding to the second field dataset ($R^2 = 0.83$, p-value < 0.05).

Figure 6.6. Correlation between the original 500 m MODIS B3 and the downscaled 250 m MODIS B3 for (a) May and (b) October, 2014.

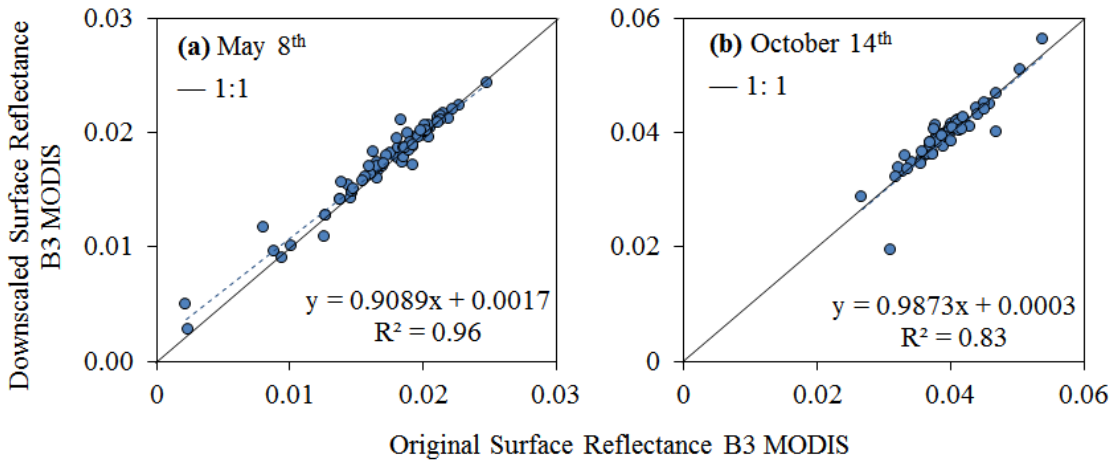

6.3.5 TSM algorithm calibration and validation

The algorithms based on single band and band ratio were analyzed using the band 1 from MODIS/Terra 250 m product and bands 3 and 4 rescaled to 250 m after resampling procedure. Besides the wide and easy applicability of the empirical models, some studies (KONG et al., 2015a, b) have shown better results from these models at low TSM concentrations compared to semi-analytical models. Miller and McKee (2004) single band model based solely on BB data (Table 6.3) achieved a strong exponential correlation ($R^2 = 0.83$, $p < 0.005$, $n = 30$) followed by the power ($R^2 = 0.82$, $p < 0.0001$, $n = 30$), quadratic ($R^2 = 0.78$, $p < 0.0001$, $n = 30$) and linear ($R^2 = 0.75$, $p < 0.0001$, $n = 30$) fits. Similar calibration for Nav was statistically significant ($p < 0.05$), however, the model based on Miller and McKee had a

poor performance when compared with BB. Both linear and quadratic models for Nav, displayed similar determinant coefficients presenting $R^2 = 0.51$ and $R^2 = 0.52$, respectively.

Table 6.3. Calibration results of the models using the single and two band indexes. Models with R^2 below 0.50 were not displayed here.

Study Site	Model	Model Fit	R^2	*s.e.**	*p-value***	*n*
BB reservoir	B1	[TSM] = 1.763 exp(261.95$B1$)	0.83	0.30	<0.005	30
		[TSM] = 68056 $B1$ ^ 1.735	0.82	0.31	<0.0001	
		[TSM] = 264559 $B1^2$ - 423.54$B1$ + 2.3818	0.78	4.76	<0.0001	
		[TSM] = 3445.6 $B1$ - 10.196	0.75	4.93	<0.0001	
Nav reservoir	B1	[TSM] = 60.199 $B1$ + 0.4396	0.51	0.17	0.0004	20
		[TSM] = 1952.8 $B1^2$ + 31.708 $B1$ + 0.5285	0.52	0.17	0.002	
Mixed Data	B1/B3	Log10[TSM] = -4.4239 $B1/B3^2$ + 11.176 $B1/B3$ - 5.9308	0.76	2.04	<0.0001	50
		Log10[TSM] = 1.9701ln($B1/B3$) + 0.5732	0.69	2.29	<0.0001	
		Log10[TSM] = 1.8876 $B1/B3$ - 1.3814	0.64	2.46	<0.0001	

* Standard error, **A significance level of 5%

Studies have shown a good correlation between TSM and single band models based on wavelengths ranging from red to NIR in different environments (MILLER and MCKEE, 2004; SIPELGAS et al., 2006; KUTSER et al., 2007; RODRÍGUEZ-GUZMÁN and GILBES-SANTAELLA, 2009; PETUS et al., 2010; ZHANG et al., 2010; ONDRUSEK et al., 2012; PARK and LATRUBESSE, 2014; KUMAR et al., 2016). The potential of these wavelengths in retrieving TSM can be explained by the bio-optical properties of the water. In turbid inland waters with low phytoplankton concentration, the absorption coefficient tends to decrease with increasing wavelength getting close to zero at the red and NIR regions whilst the backscattering coefficient of suspended sediment increases in those regions (DOXARAN et al., 2006, CUI et al., 2013). However, according to Figure 6.4, it is clear that BB is highly affected by phytoplankton absorption in the red wavelength and Nav is dominated by particulate and water itself. A significant quadratic correlation between the band ratio $R_{rs_{sim}}(645)/R_{rs_{sim}}(469)$ and *in situ* TSM in log scale ($R^2 = 0.76$, $p < 0.0001$) was obtained using the mixed dataset from Nav and BB ($n = 50$), followed by the logarithmic ($R^2 = 0.69$, $p < 0.0001$) and linear ($R^2 = 0.64$, $p < 0.0001$) models. Previous studies have shown a good relationship between log transformed water quality data (TSM and Chl-*a*) and R_{rs} for productive waters such as those on Florida's northwest coast (WANG et al., 2010; CHEN et al., 2011). Olmanson et al. (2013) highlighted that the water quality data could behave normally or near normal when they are log transformed, agreeing with assumptions of regression. Fan (2014) who retrieved TSM concentration using *in situ* hyperspectral data also achieved a good relationship using a linear model based on the

spectral ratio of 650/420 in Patuxent River, tributary of Chesapeake Bay, USA. It is noteworthy that a statistically significant relationship does not always result in small errors, thus all the models and their respective variations were validated.

To validate the calibrated models, $R_{rs_{sat}}$ extracted from MODIS images were used. Among all the tested models, the approach using two calibration equations, one for each reservoir retrieved the lowest error instead of applying a single model to the mixed data. The model based on exponential fit of band 1 showed a RMSE = 3.66 mg l^{-1} and a NRMSE = 31.54% for BB, and for Nav, both linear and quadratic models had very similar results with a slight improvement of the linear fit (RMSE = 0.37 mg l^{-1} and NRMSE = 29.43%) over the quadratic fit (RMSE = 0.37 mg l^{-1} and NRMSE = 29.48%). The model related to the mixed data presented the highest RMSE with the linear fit (RMSE = 64.70 mg l^{-1} and NRMSE = 401.89%) and the lowest error with the logarithm equation (RMSE = 5.48 mg l^{-1} and NRMSE = 34.04%) but even so, overestimating the TSM values for Nav. The NMRSE was also high compared to the approach using different models for each study site. For that reason, the exponential model based on band 1 was used to map BB and the linear equation also based on band 1 was used to map Nav.

The predicted TSM from BB was, in general, underestimated (*bias* = -1.98 mg l^{-1}) but the residuals did not present any trend. According to Dogliotti et al. (2015), high errors at 645 nm are associated with phytoplankton absorption considering productive environments with Chl-*a* > 30 mg m^{-3}. Thus, the underestimation might be related to the phytoplankton absorption, which is masking the reflectance and therefore the model's performance. TSM predicted from Nav was overestimated (*bias* = 0.14 mg l^{-1}) and no clear trend in residual was observed. This overestimation can be explained by the increment of combined effect of both water and phytoplankton absorption in the red spectral region. Cui et al. (2013) also draw attention to the fact that shallow waters and submerged vegetation might be the reason of this overestimation. Nav is affected by submerged vegetation mainly at the edges of the reservoir and Rotta et al. (2016) studied the effect of radiation availability on development and growth of this type of vegetation in a tributary of Nav reservoir. The predicted TSM produced by the mixed data overestimated the low concentrations but did not present any trend. These results emphasize the poor performance of one single model to describe the TSM variability in two widely different environments in terms of limnology and optical properties. On the other hand, the separate approach showed to be suitable to map the TSM variability.

This type of poor performance by a single model was not found by Chen et al. (2015), who used a quadratic log-ratio model based on red and NIR MODIS-250 m bands to study a wide range of TSM concentration (5.8 – 577.2 mg l^{-1}) in China's estuaries and coastal waters. After validation, they found a RMSE = 37.9 mg l^{-1} for TSM > 31 mg l^{-1} and a RMSE = 3.25 mg l^{-1} for TSM ≤ 31 mg l^{-1}, however, when applied to the data from Nav and BB (mixed data), the RMSE was 18.60 mg l^{-1} showing the site-specific limitation of this model in retrieving TSM in an environment different from the one used to calibrate the original model. Han et al. (2016) also worked with a wide-range TSM concentration (0.15 – 2,626 mg l^{-1}) from clear to very turbid waters around the world but used a semi-analytical (SAA) way to retrieve this parameter with a RMSE > 1.8 mg l^{-1}. The authors make it clear that splitting the data into clear to medium turbid and highly turbid waters, increases the accuracy of TSM retrieval. Thus, they created TSM-range dependent algorithms considering concentrations lower and higher than 100 mg l^{-1} and then introduced a weighting function aiming to avoid artificial spatial pattern in TSM distribution. The SAA algorithm when applied to the low TSM range produced a RMSE of 11.07 mg l^{-1} for Nav and BB data, which is high considering the range found in both reservoirs. Factors such as optical properties and water composition shown to be greatly responsible for the inefficiency of a single model built to map a range between very low (values predominantly lower than 1.00 mg l^{-1}) to moderate TSM concentration (< 44.00 mg l^{-1}) such as in Nav and BB, respectively.

Binding et al. (2010) highlighted that the choice of the model and suitable band depends on the optical characteristic of the water and the range of TSM concentration. According to Figure 6.4, inorganic matter and CDOM basically control the optical characteristics of the water in Nav. Presence of CDOM and phytoplankton affects the visible bands (wavelengths shorter than 550 nm), constraining the use of a band with shorter wavelength for determining TSM concentration in optically complex waters (BINDING et al., 2010). Binding et al. (2005) showed that high mineral suspended solid (MSS) concentration increases the reflectance in longer wavelengths and the minimal influence of CDOM in this region suggest the use of red channel to map MSS. These findings support the fact that at 645 nm, the model based on Nav's dataset, performed better than other models. On the other hand, in BB, TSM is primarily phytoplankton dominated, which means that R_{rs} will be low in the visible spectral region due to high absorption by pigments. This increase in chl-*a* concentration (> 100 µg l^{-1}) can affect the TSM reflectance between 400 and 700 nm, and the chl-*a* behavior starts to overshadow the TSM reflectance characteristics (SVÁB et al., 2005). Song et al. (2014) showed a high

correlation coefficient between TSM and reflectance at approximately 700 nm in turbid water dominated by algal and non-algal particles, insinuating that for productive inland waters, the best approach may be to use the longer wavelengths. However, for BB the band 1 based non-linear model achieved the best performance compared to both linear and non-linear fits using the band at 859 nm.

The nature of the water composition can be explained by the LULC of the watershed, which is responsible for the inputs of OSCs affecting the optical properties. LULC such as urban and agriculture can act as a source for nutrients enrichment in water systems. High loads of nutrients can lead to the increase of primary production and consequently the increase of $a_{\phi}(443)$. Particle matter content can also influence $a_{NAP}(443)$ (LE et al., 2015). Bernardes et al. (2004) found that high values of delta thirteen carbon ($\delta^{13}C$) in the ultrafiltered dissolved organic matter were correlated to areas covered with pasture in the Ji-Paraná Basin, Amazon, which means that the replacement of primary forests by pastures for cattle feeding has changed the composition of the riverine organic matter. Further discussion about this topic can be found in the following sections.

6.3.6 TSM spatio-temporal variability

Images from May (beginning of the dry season) and October (end of the dry season) for the period from 2000 to 2015 were chosen to analyze the spatio-temporal variability of TSM using the most accurate model for each reservoir. The models based on visible wavelengths proved to be more applicable for moderate ranges of TSM instead of band ratio, which showed to be more correlated to environments dominated by MSS (DOXARAN et al., 2002, BINDING et al., 2003). Song et al. (2014) observed a high correlation between band ratios and TSM for turbid productive waters at the Chl-*a* absorption bands in the lake Taihu, China. Such band ratios (e.g., MODIS B1/B3) were not able to retrieve TSM accurately in these reservoirs with widely varying optical properties. The pattern of TSM distribution across both seasons was consistent with previous studies (CAVENAGHI et al., 2003; PANHOTA and BIANCHINI Jr., 2003; ZANATA, 2005). The spatio-temporal distribution of TSM in Nav showed very low concentrations in the entire reservoir in May with majority of the pixels ranging between 0 – 1.2 mg l^{-1} (Figure 6.7). In October, the TSM concentration increased slightly but homogeneously in the entire reservoir with most of the pixels concentrated between 0.6 – 2.6 mg l^{-1}. In BB, TSM ranged from 5.01 to 10 mg l^{-1} in May and 35 to 50 mg l^{-1} in October. In general, BB is much more turbid than Nav (Figure 6.8).

Figure 6.7. Spatio-temporal distribution of TSM over the main body of Nav based on MODIS 8-day composite images for months of May and October from 2000 to 2015.

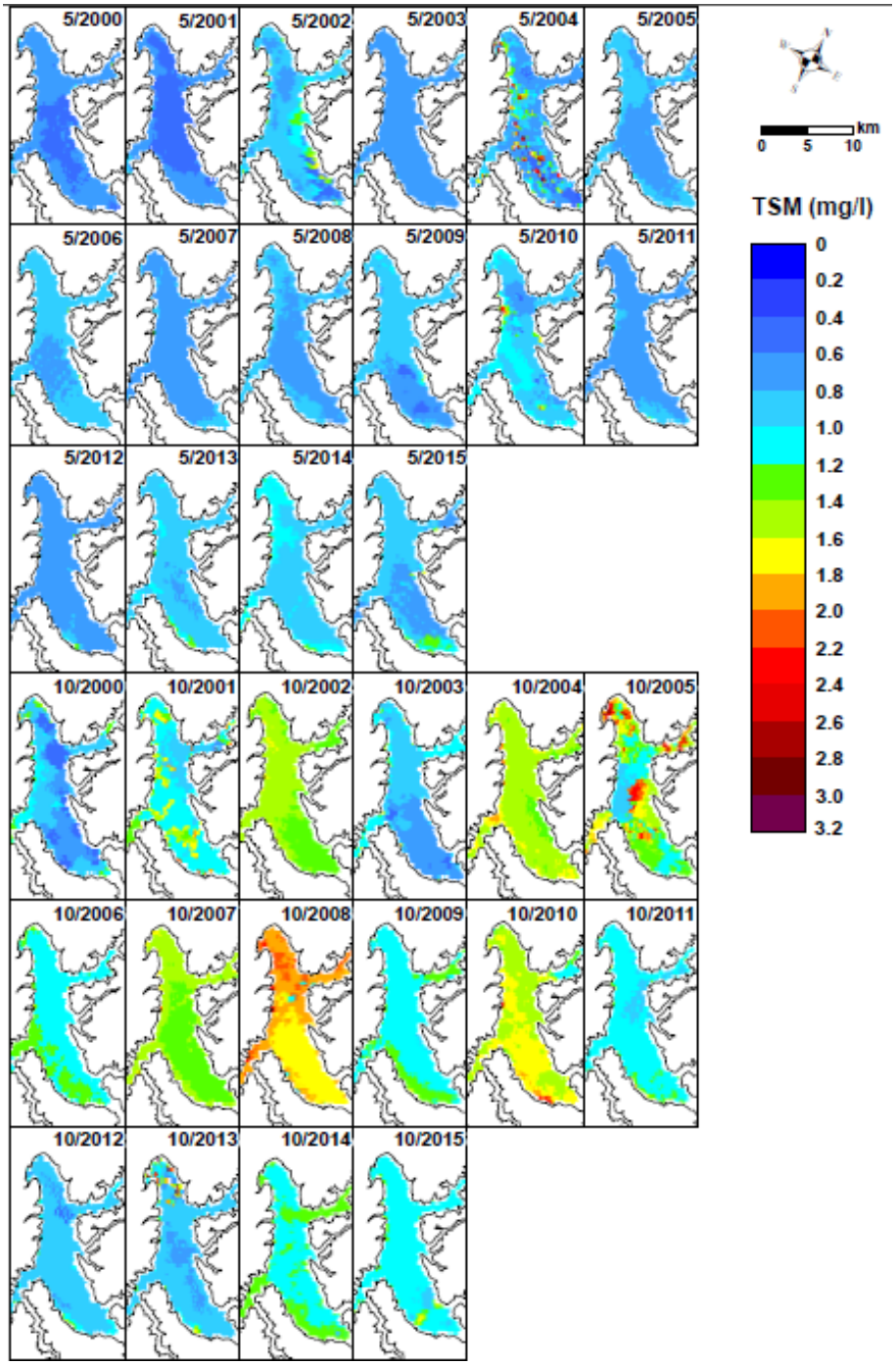

Figure 6.8. Spatio-temporal distribution of TSM over the main body of BB based on MODIS 8-day composite images for the months of May and October from 2000 to 2015. The blank region represent the locations where the model extrapolated the TSM values over 150 m l^{-1}.

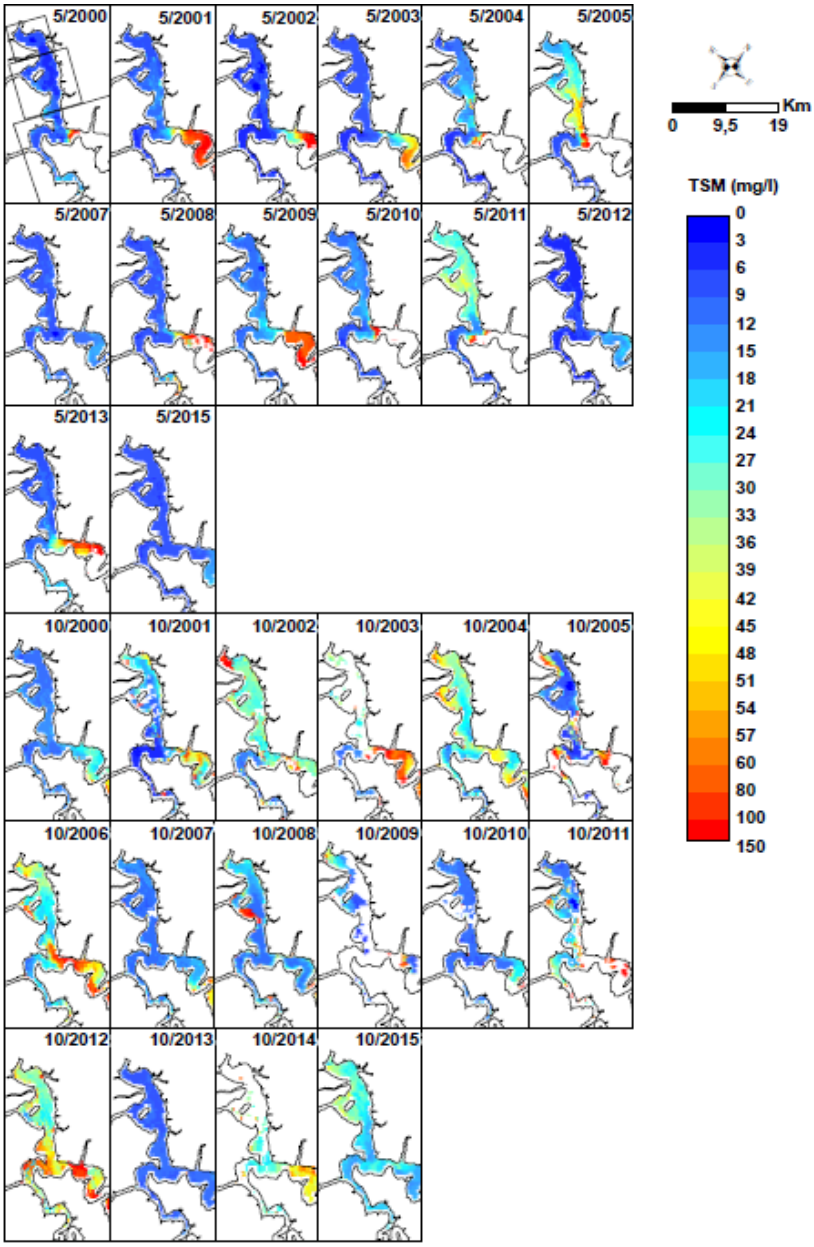

Factors such as geomorphology, LULC setting, location, wind, river flow, climatic conditions and topography tend to impact the range and variability of TSM in a reservoir (WANG et al., 2010). Therefore, the high TSM in October compared to May in both reservoirs is probably because of the high rainfall induced runoff from the upland watersheds that transports sediment and other materials into the reservoirs. The spatial distribution of TSM in Nav showed a homogeneous dispersion along the reservoir and can be related to the type of operation of the dam, which is a run-of-river, and the shape of this reservoir that is elongated

and continuous. These features lead to low variation of the water level, high frequency and behaving as a semi-lotic environment with intermediate fluvial characteristics (PERBICHE-NEVES et al., 2011; PERBICHE-NEVES and NOGUEIRA, 2013). On the other hand, TSM in BB varied spatially showing high values around the island that is connected to the Araquá River (see Figure 2.1 for location) in May mainly because of contributions from anthropogenic sources such as sugarcane plantations. In addition, this region is very susceptible to the proliferation of floating macrophytes and as stated in Cavenaghi et al. (2003), the presence of these floating vegetation was related to the sedimentation process located in the reservoir`s edge and coming from the confluents. Overall, higher values of TSM were found in October and the water coming from the Tietê River contributed less than Piracicaba River.

The overestimation found in BB map can be associated to the limitation of the model to represent concentrations over 50 mg l^{-1}. Cui et al. (2013) also noticed a saturation problem using the red band from MODIS/Terra indicating that the exponential model may introduce high errors when applied in very turbid waters. Wu et al. (2013) faced the same problem using non-linear models based on red band from MODIS/Terra and to overcome this issue, they used a NIR based linear model, but after validation, the accuracy was very low (correlation of 0.54). Feng et al. (2014) highlighted the same concern of saturation for high TSM concentrations when applying blue and red bands based models and they came up with a model based on two equations: one for TSM < 50 mg l^{-1} (using the red band from MODIS) and other for TSM > 150 mg l^{-1} (using the band ratio between NIR over red), both using the exponential fit. Low concentrations of TSM can be problematic for mapping. Kumar et al. (2016) found that in Chilika Lake, the MODIS-based model was not suitable for retrieving TSM concentrations below 6.54 mg l^{-1}. Han et al. (2016) tested Nechad et al. (2010) model using their wide-range TSM and noticed that values lower than 1.2 mg l^{-1} were overestimated. Therefore, it can be concluded that all MODIS based TSM algorithms tested in this study are somewhat site or region specific. A truly scalable TSM algorithm that fits all water bodies is not available. That explains why there are so many variations of semi-empirical TSM models in the literature. Many of them applied in this study proved that they are in fact not highly scalable across broad geographic regions and turbidity regimes.

Another issue that also affects the model performance is related to the quality of the image, especially with regards to atmospheric correction. Wang et al. (2015) improved the signal of R_{rs} by subtracting the average response from SWIR bands (centered in 1640 and 2130 nm) in order to offset the deficiency in the original atmospheric correction of MOD09 product.

This approach was used in Lake Taihu, China, which is very turbid and productive system, however, the performance of this approach was not satisfactory to less turbid systems such as Nav and BB. Therefore, the correction proposed by Wang et al. (2015) produced negative values after subtraction by SWIR bands and was not included in this paper.

The TSM variability in different sectors of the reservoirs can be seen in Figure 6.9. In Nav, samples picked at five different locations along the reservoir showed a homogeneous behavior from 2000 to 2015 in May. In October, the magnitude of TSM increased, however, none of the sectors stood out from the rest, highlighting the homogenous distribution in Nav.

Figure 6.9. TSM variability during the (a) beginning of the dry season and (b) end of the dry season in Nav; (c) beginning of the dry season and (d) end of the dry season in BB at different locations along the reservoir. SBS: Santa Barbara Stream, BR: Bonito River, PR: Piracicaba River, TR: Tietê River, TZ1: Tranzition Zone 1, TZ2: Transition Zone 2. (e) TSM (mg l^{-1}) concentration from field campaigns carried out in Tietê River (Barra Bonita – BB, Bariri – B, Ibitinga – I, Promissão – P, Nova Avanhandava – Nav) except for Três Irmãos (TI) reservoir in 2000 (CAVENAGHI et al., 2003) (solid lines); including all reservoirs along the Tietê River during the years 2001 and 2002 (ZANATA, 2005) (dotted lines) and in the lower Tietê basin during 2008 and 2009 (dashed lines) (SANTOS, 2010).

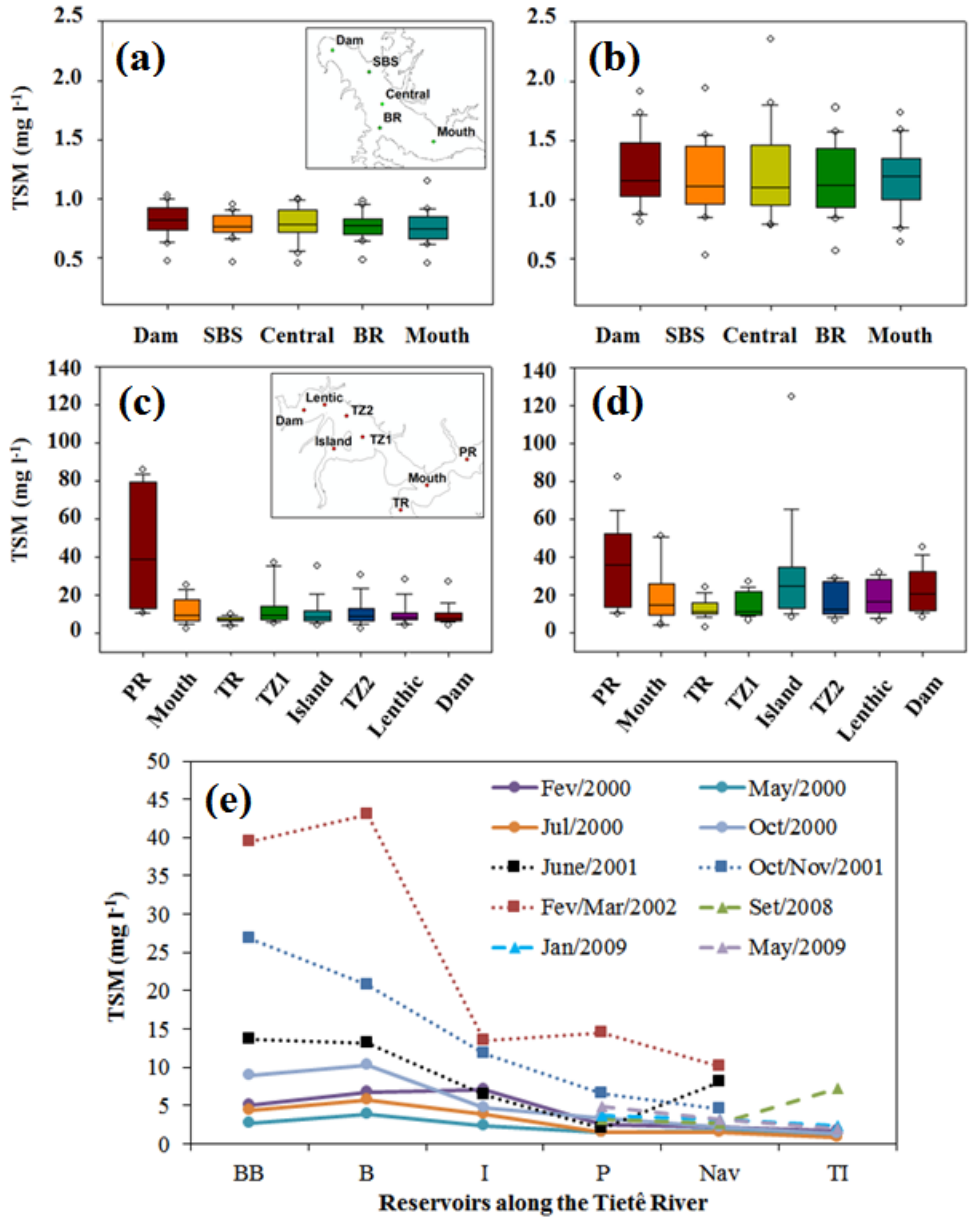

Overall, the MODIS/Terra based maps showed the seasonal influence in TSM concentration. The rainy season contributes to the entry of autochthonous matter from the watershed increasing the concentration of particulate matter. *In situ* TSM data based on

different studies carried out in Tietê River basin in different dates are presented to support the analysis (Figure 6.9e). TSM tend to increase during October and the opposite was observed for April and May. The same trend was found in other studies for the site (BARBOSA et al., 1999, CAVENAGHI et al., 2003) and the gradient of TSM decreases from the upstream to downstream reservoirs, becoming less pronounced in the low basin reservoirs, Promissão, Nav and Três Irmãos. As highlighted by Rodgher et al. (2005), the suspended matter originated from Tietê and Piracicaba Rivers in the rainy season is very high when compared to that of the dry season. The turbidity composed by inorganic fraction diminished significantly in BB, however, this change is less noticeable in the downstream reservoirs (BARBOSA et al., 1999).

6.3.7 Factors affecting optical changes in the reservoirs

The poor accuracy of the mixed model can be attributed to the differences in the water quality composition of both sites. BB is phytoplankton dominated while Nav is inorganic matter dominated with contribution of CDOM at 443 nm. Although the same river is the source for both reservoirs, the LULC compositions of the watershed are different and as stated by Sandes (1990), it is necessary to consider the input of pollutants by diffuse and punctual sources in each reservoir. The BB watershed is covered by urban centers, bare soil, agriculture fields, and shrubland also represented by planted crops. Nav is occupied in general by agriculture with low influence of urban centers. Urban and agriculture activities contribute with the fluctuations of inorganic nutrients levels changing the primary producers (TONG and CHEN, 2002; ROBINSON et al., 2014). Ahearn et al. (2005) found a good correlation between agriculture and nitrate-N loading as well as Coulter et al. (2004) who also observed agriculture as a greater source of nutrients when compared with urban land uses that yielded high suspended sediment concentrations. Tu (2011; 2013) and Zhao et al. (2015) pointed out that agriculture can be a source of pollution in less-urbanized watersheds, however, the contrary is true when agriculture is interleaved in a highly-urbanized watershed. This is because in highly urbanized areas the pollution coming from agriculture is negligible and often masked by urban sources. Li et al. (2008) studying the Han River, China, observed that both urban and agriculture areas have dominant control on TSM concentration. Besides, the authors also noticed that vegetated coverage was related to water temperature, nitrogen and the high vegetation cover presented low turbidity, suspended particulate matter, nutrients and total dissolved solids. The Tietê River catchment basin is highly affected by anthropogenic activities that are considered a pollution source. As stated by Petesse et al. (2014), the catchment portion in the upstream of the BB

reservoir is densely populated with twenty-six million people (90.5% of the total Tietê River basin population). A similar study by Im et al. (2015) revealed that wastewater coming from the city was the major source of water quality deterioration on Cheung Ek Lake, Thailand. Busse et al. (2006) also concluded that algal biomass increases with urbanization and during summer, chlorophyll concentrations were correlated to light and nutrient levels. Activities such as industry and agriculture are also highly active in this region mainly related to sugarcane plantation. Barra Bonita municipality has a biomass power plant which produces vinasse as residue and further used as fertilizer for sugarcane plantations. This byproduct of the sugarcane industry is composed by nutrients (potassium calcium, nitrogenous, sulfur and magnesium) and is absorbed by plants and also drained through the soil reaching the aquatic system (PRADO, 2004).

Agriculture is also predominant around Nav sub-basin; however, the water quality is better than that of BB (BARBOSA et al., 1999) suggesting that other factors, in addition to agriculture, could be more important for the poor water quality in BB. Tietê and Piracicaba rivers are susceptible to domestic and industrial contamination due to the proximity to urban centers along its course. Carvalho et al. (2005) highlighted that the occurrence of floating vegetation in BB is due to high turbidity and, on the other hand, submerged vegetation is frequent in low turbidity environments such as Nav. According to Cavenaghi et al. (2003), the phosphate values are higher in BB reservoir (average value of 170 μg l^{-1} in 2001 and 2002) than those further downstream such as Nav (25.42 μg l^{-1}). A similar decreasing pattern is also observed for suspended solids, turbidity and electrical conductivity. As discussed here, the LULC have a direct effect on the water quality increasing the eutrophication process in manmade water bodies and ultimately changing in optical water quality. Different water composition and a wide TSM range can induce systematic error in red and NIR based TSM models.

6.4 Conclusion

Optical and water quality *in situ* data were collected from two widely different reservoirs, eutrophic Barra Bonita and oligo-mesotrophic Nova Avanhandava, along Tietê River's cascade reservoir system. The data were used to calibrate a TSM algorithm for the MODIS/Terra satellite surface reflectance products. Several empirical TSM models were tested for the reservoirs (TSM range: 0–44 mg l^{-1}) using simulated remote sensing reflectance ($R_{rs_{sim}}$)

for calibration and remote sensing reflectance of the satellite ($R_{rs_{sat}}$) for validation. Considering the variability of TSM values at both sites, the site-specific models had a good fit and represented the spatial pattern of this optically significant component well. The source and nature of water quality parameters were crucial to understand the limitations of a single empirical model in characterize optically different environments. Besides, the bio-optical models showed to be constrained by the watershed composition.

BB reservoir receives sediment contribution from two rivers: Tietê and Piracicaba and during the beginning of the dry season, it was noticed that high values of TSM is associated with the flow from Tietê River. This high sediment load creates a favorable condition for emergent macrophytes that float downstream toward the dam. On the other hand, TSM spatial distribution in Nav was very homogeneous along the whole reservoir and besides, the variability during the water collections was not outstanding; mainly due to the type of operation of that reservoir, that is run-of-river.

The spatial analysis results from this study corroborate with other studies regarding the improvement of water quality from upstream to downstream in a cascade system, showing the difference in water composition for both sites. The TSM from BB showed a strong relationship with phytoplankton and the TSM from Nav was influenced by inorganic matter. Use of a single model to resolve the TSM of different origins was not possible and site-specific approach worked best to resolve the spatial variability of TSM in these reservoirs. The monitoring of the water quality in a cascade system such as this using an accurate single model is very challenging because of the wide variability of water quality and optical properties along the same river across a varying LULC gradient. Understanding of the environmental forcing that affect each reservoir's water quality could be the key to designing a robust monitoring approach.

CHAPTER 7: CONCLUSION AND FUTURE RECOMMENDATIONS

7.1 Conclusion

The results achieved in this thesis confirmed the hypothesis that organic and inorganic dominated waters such as BB and Nav, respectively, decrease the performance of a single empirical model to estimate TSS; however, after recalibrating the empirical steps of QAA, the performance of the model increased and could estimate a_t accurately, considering both reservoirs.

The OSCs collected between 2014 to 2016 showed considerable changes between BB and Nav. The first one was more turbid and phytoplankton dominated, while Nav was less productive and presented more clear water. The OSC concentration varied in magnitude according to the field trips showing high dependence of rainfall condition. The year of 2014 showed atypical rainfall condition leading to modifications in water quality mainly in BB which is a storage system, therefore accumulates water during the dry season. The average Chl-*a* concentration increased from 120.4 µg l^{-1} in May/2014 to 428.7 µg l^{-1} in October/2014. However, in Nav the Chl-*a* concentration did not vary showing averages of 6.2 µg l^{-1} and 9.0 µg l^{-1} in April-May/2014 and September/2014, respectively. This was probably related to the operation system, in this case, a run-of-river reservoir, so the water flows continuously not storing for dry periods. A third data collection was carried out in Nav (May/2016) but the lowest rainfall rate in the previous months, even less than 2014, led to the increase of primary production and consequently the increase of the average Chl-*a* concentration (26.4 µg l^{-1}). The same pattern happened for TSS, also affecting the water transparency.

This water quality scenario echoed to the optical properties. Nav, for example, showed high variance in the absorption at 443 nm with a_{NAP} in Nav1 and CDOM, a_{CDOM} in Nav2. The Nav3 was dominated by a_{NAP}. At 560 nm, a_{NAP} varied with other components but was dominant at all field trips and at 665 nm the phytoplankton (a_ϕ) was dominant, except for Nav2 that varied with other components. As expected BB was fully dominated by phytoplankton with percentages reaching 87% in BB2 at 665 nm, however at 443 and 560 nm its dominance was below 50% for BB1, highlighting the interference of other components. The implication of these findings to the bio-optical modeling is important, because we now understand that Nav is highly affected by NAP and CDOM at the blue and green regions rather than phytoplankton.

BB, on the other hand, was dominated by a_ϕ at 665 nm, not varying with other components, so this wavelength must be recommended for Chl-*a* estimation.

The IOPs showed to be useful for water characterization, and they are used in several semi-analytical models, therefore the use of remote sensing approaches seems to be valuable for water quality monitoring. Nav is categorized as inland water, however, is not productive which is different from the previous waters used in QAA parametrization. All these versions failed leading to the definition of new steps for QAA and here named as QAA_{OMR}. The main issue behind this failure was first addressed to the reference wavelength selection, which is responsible to highlight just the contribution of water in the total absorption budget. The obstacle found on previous QAAs was related to $a_\phi(\lambda)$ retrieval based on simple subtraction between $a_t(\lambda)$ and $a_{CDM}(\lambda)$, however, the errors was very high surpassing 100% of uncertainties considering specific wavelengths. Therefore, we came up with a new approach recently suggested by Ogashawara et al. (2016) but with relevant modifications aiming to derive a_ϕ (443) based on Lee et al. (2010) and the normalized $a_\phi^+(\lambda)$ discussed by Roesler et al. (1989). A great improvement was achieved with uncertainties below 50% (412 – 681 nm). An independent dataset was used for validation and the QAA_{OMR} showed to be robust in retrieving the IOPs, and even assuring the necessity of use data from broader geographic regions, the model comes to give a better solution for waters characterized as oligo-to-mesotrophic and dominated by inorganic matter.

As previously described, both reservoirs are optically different, however, for water management purposes is very important to use a single approach to retrieve optical water properties covering the whole cascade system. The QAA from Watanabe et al. (2016), QAA_{BBHR}, was parametrized using data from BB and the results was very satisfactory, however it showed limitations in retrieving $a_\phi(\lambda)$, therefore, we evaluated the performance of each QAA in retrieving $a_t(\lambda)$, $a_{CDM}(\lambda)$ and $a_\phi(\lambda)$ pointing out the main issues surrounding their estimative. Both QAA versions (QAA_{BBHR} and QAA_{OMR}) could retrieve $a_t(\lambda)$ considering different types of water with a slight advantage of QAA_{BBHR}. Therefore, a single model can be suitable to estimate at least $a_t(\lambda)$, considering different trophic state waters. On the contrary, more efforts must be carried out for improving the $a_{CDM}(\lambda)$ and $a_\phi(\lambda)$ estimation aiming to reduce the errors below 50%.

Regarding the performance of an empirical model for TSM retrieval considering the data from both reservoirs, several empirical models were tested considering the TSM range of 0 and 44 mg l^{-1} using simulated remote sensing reflectance ($R_{rs_{sim}}$) for calibration and remote

sensing reflectance of the satellite ($R_{rs_{sat}}$) for validation. However, none of those models could cover the range of the study sites. For very low concentration, the single model tended to overestimate sediment concentration and the use of the linear adjustment based on the red band could improve the result significantly. On the other hand, the moderate concentration was successfully retrieved using the exponential fit of red band. The main issue concerning the use of single model was related to the bio-optical properties from both reservoirs. As previously mentioned, the sediment composition of BB is primarily composed by phytoplankton whilst Nav is inorganic dominated water. These properties limit the use of a single approach aiming to cover very low to moderate TSM concentrations. To address this issue, semi-analytical approaches could be a potential way to model wide range of sediment concentration and it will be considered for future works.

7.2 Future Recommendations

The current results showed great improvements in remote sensing of inland waters researches, although this was just the start of a series of issues that need to be addressed. Understanding the bio-optical diversity of individual environments such as the reservoirs of the Tietê River is very important, however, when we consider the entire cascade the bio-optical modeling approach quite changes. So, for future works it is worth to include as many data as possible from all the elements of the cascade to turn the study area more representative.

Besides, it is also relevant to analyze not only the longitudinal modifications along the system but also the relationship between the anthropogenic activities, such as agriculture, industries and urban centers, that surround the reservoirs and they are part of the watershed dynamic. Few works have relating the impact of the LULC on the IOPs, but they already know that the watershed is the source of OSC, that affects the optical properties of inland waters.

In terms of OSC retrieval in wide range of concentrations, empirical models have shown their limitation in cover both low and high concentrations, so the development of semi-analytical approaches based not only on radiance or reflectance, but also the IOPs may be a good way out for this situation. In the case of Tietê River, split the cascade according to the trophic state can possibly be a first step for water monitoring. The reservoirs from the Low basin present a better water quality than those upstream in the Middle basin, therefore they can be merged and worked initially together.

The QAA_{OMR} showed great enhancements for IOPs retrieval and it showed to be the only one, which, up to now, was parameterized in inland water with limited primary production

and dominated by inorganic matter. However, the estimation of $a_\phi(\lambda)$ still needs attention. For future works, data of absorption, scattering and backscattering coefficients collected in the field by robust instruments such as the ac-s and the ECO-BB9 from WETLabs, needs to be included in the process of validation and tuning of empirical steps of QAA.

REFERENCES

AHEARN, D. S. et al. Land use and land cover influence on water quality in the last free-flowing river draining the western Sierra Nevada, California. **Journal of Hydrology**, v. 313, n. 3–4, p. 234–247, 2005.

AHN, C.; CHUNG, A.; OH, H. Rainfall, phycocyanin and N:P ratios related to cyanobacterial blooms in a Korea large reservoir. **Hydrobiologia**, v. 474, p. 117–124, 2002.

ALCÂNTARA, E. et al. Field measurements of the backscattering coefficient in a cascading reservoir system: first results from Nova Avanhandava and Barra Bonita Reservoirs (São Paulo, Brazil), **Remote Sensing Letters**, v. 7, n. 5, p. 417-426, 2016.

ANDERSON, D. M.; GLIBERT, P. M.; BURKHOLDER, J. M. Harmful Algal Blooms and Eutrophication Nutrient Sources, Composition, and Consequences. **Estuaries**, v. 25, n. 4b, p. 704–726, 2002.

APHA/AWWA/WEF. 1998. **Standard methods for the examination of water and wastewater**. Washington, DC.

BABIN, M. et al. Variations in the light absorption coefficients of phytoplankton, nonalgal particles, and dissolved organic matter in coastal waters around Europe. **Journal of Geophysical Research**, v. 108, n. C7, p. 1–20, 2003.

BARBOSA, F. A R. et al. The cascading reservoir continuum concept (CRCC) and its application to the river Tietê-basin, São Paulo State, Brazil. Theoretical reservoir ecology and its applications1, p. 425–437, 1999.

BARNES, W. L.; PAGANO, T. S.; SALOMONSON, V. V. Prelaunch Characteristics of the Moderate Resolution. **IEEE Transactions on Geoscience and Remote Sensing**, v. 36, n. 4, p. 1088–1100, 1998.

BARNES, W. L.; XIONG, X.; SALOMONSON, V. V. Status of terra MODIS and aqua MODIS. **Advances in Space Research**, v. 32, n. 11, p. 2099-2106, 2003.

BELZILE, C.; GUO, L. Optical properties of low molecular weight and colloidal organic matter: Application of the ultrafiltration permeation model to DOM absorption and fluorescence. **Marine Chemistry**, v. 98, n. 2–4, p. 183–196, 2006.

BERNARDES, M. C. et al. Riverine organic matter composition as a function of land use changes, southwest Amazon. **Ecological Applications**, v. 14, n. 4 SUPPL., p. S263–S279, 2004.

BI, N. et al. Seasonal variation of suspended-sediment transport through the southern Bohai Strait. **Estuarine, Coastal and Shelf Science**, v. 93, n. 3, p. 239–247, 2011.

BINDING, C. E. et al. Suspended particulate matter in Lake Erie derived from MODIS aquatic colour imagery. **International Journal of Remote Sensing**, v. 31, n. 19, p. 5239–5255, 2010.

BINDING, C. E.; BOWERS, D. G.; MITCHELSON-JACOB, E. G. An algorithm for the retrieval of suspended sediment concentrations in the Irish Sea from SeaWiFS ocean colour satellite imagery. **International Journal of Remote Sensing**, v. 24, n. 19, p. 3791–3806, 2003.

BINDING, C. E.; BOWERS, D. G.; MITCHELSON-JACOB, E. G. Estimating suspended sediment concentrations from ocean colour measurements in moderately turbid waters; the impact of variable particle scattering properties. **Remote Sensing of Environment**, v. 94, n. 3, p. 373–383, 2005.

BINDING, C. E. et al. Spectral absorption properties of dissolved and particulate matter in Lake Erie. **Remote Sensing of Environment**, v. 112, n. 4, p. 1702-1711, 2008.

BRANDO, V. E. et al. Adaptive semianalytical inversion of ocean color radiometry in optically complex waters. **Applied Optics**, v. 51, n. 15, p. 2808–2833, 2012.

BREUNIG, F. M. et al. Assessing the Long-Term Variability of TSS and Chlorophyll in Subtropical Reservoirs Using MODIS Data. **IEEE Journal of Selected Topics in Applied Earth Observations and Remote Sensing**, v. PP, n. 99, p. 1–7, 2016.

BRICAUD, A.; MOREL, A.; PRIEUR, L. Absorption by dissolved organic matter of the sea (yellow substance) in the UV and visible domains. **Limnology and oceanography**, v. 26, n. 1, p. 43-53, 1981.

BRICAUD, A. et al. Variability in the chlorophyll-specific absorption coefficients of natural phytoplankton: Analysis and parameterization. **Journal of Geophysical Research: Oceans**, v. 100, n. C7, p. 13321-13332, 1995.

BRICAUD, A. et al. Variations of light absorption by suspended particles with chlorophyll a concentration in oceanic (case 1) waters: Analysis and implications for bio-optical models. **Journal of Geophysical Research**, v. 103, n. C13, p. 31033–31044, 1998.

BRICAUD, A. et al. Light absorption properties and absorption budget of Southeast Pacific waters. **Journal of Geophysical Research: Oceans**, v. 115, n. 8, p. 1–19, 2010.

BRÖNMARK, C.; HANSSON, L.-A. Environmental issues in lakes and ponds: current state and perspectives. **Environmental Conservation**, v. 29, n. 3, p. 290–306, 2002.

BUKATA, R. P. **Satellite monitoring of inland and coastal water quality: retrospection, introspection, future directions**. CRC Press, 2005.

BUSSE, L. B.; SIMPSON, J. C.; COOPER, S. D. Relationships among nutrients, algae, and land use in urbanized southern California streams. **Canadian Journal of Fisheries and Aquatic Sciences**, v. 63, n. 12, p. 2621–2638, 2006.

CAIRO, C. T. et al. Spatial and seasonal variation in diffuse attenuation coefficients of downward irradiance at Ibitinga Reservoir, São Paulo, Brazil. **Hydrobiologia**, 2016.

CALLISTO, M. et al. Biodiversity assessment of benthic macroinvertebrates along a reservoir cascade in the lower São Francisco river (northeastern Brazil). **Brazilian journal of biology = Revista brasileira de biologia**, v. 65, n. 2, p. 229–40, 2005.

CALIJURI, M. DO C.; DOS SANTOS, A. C. A.; JATI, S. Temporal changes in the phytoplankton community structure in a tropical and eutrophic reservoir (Barra Bonita, S.P.—Brazil). **Journal of Plankton Research**, v. 24, n. 7, p. 617–634, 2002.

CAMPBELL, G.; PHINN, S. R.; DANIEL, P. The specific inherent optical properties of three sub-tropical and tropical water reservoirs in Queensland, Australia. **Hydrobiologia**, v. 658, n. 1, p. 233-252, 2011.

CARDER, K. L. et al. Marine humic and fulvic acids: their effects on remote sensing of ocean chlorophyll. **Limnology and oceanography**, v. 34, n. 1, p. 68-81, 1989.

CARDER, K. L. et al. Reflectance model for quantifying chlorophyll a in the presence of productivity degradation products. **Journal of Geophysical Research: Oceans**, v. 96, n. C11, p. 20599-20611, 1991.

CARDER, K. L. et al. Semianalytic Moderate-Resolution Imaging Spectrometer algorithms for chlorophyll a and absorption with bio-optical domains based on nitrate-depletion temperatures. **Journal of Geophysical Research**, v. 104, p. 5403, 1999.

CARDER, K. L. et al. Performance of the MODIS semi-analytical ocean color algorithm for chlorophyll-a. **Advances in Space Research**, v. 33, n. 7, p. 1152-1159, 2004.

CARVALHO, F. T. et al. Influência da turbidez da água do rio Tietê na ocorrência de plantas aquáticas. **Planta Daninha**, v. 23, n. 2, p. 359–362, 2005.

CAVENAGHI, A. L. et al. Caracterização da qualidade de água e sedimento relacionados com a ocorrência de plantas aquáticas em cinco reservatórios da bacia do rio Tietê. **Planta Daninha**, v. 21, p. 43–52, 2003.

CBH-BT/CETEC: Comitê da Bacia Hidrográfica do Baixo Tietê. Centro Tecnológico da Fundação Paulista de Tecnologia e Educação. **Situação dos Recursos Hídricos do Baixo Tietê – Minuta preliminar do relatório técnico final**, Lins, CBH-BT, 1999. Available: <http://www.sigrh.sp.gov.br/sigrh/ARQS/RELATORIO/CRH/CBH- BT/232/relbtseg.pdf>. Access in: 8 may 2013.

CHEN, S. et al. Remote sensing assessment of sediment re-suspension during Hurricane Frances in Apalachicola Bay, USA. **Remote Sensing of Environment**, v. 113, n. 12, p. 2670–2681, 2009.

CHEN, S. et al. Remote sensing analysis of rainstorm effects on sediment concentrations in Apalachicola Bay, USA. **Ecological Informatics**, v. 6, n. 2, p. 147–155, 2011a.

CHEN, S. et al. An enhanced MODIS remote sensing model for detecting rainfall effects on sediment plume in the coastal waters of Apalachicola Bay. **Marine Environmental Research**, v. 72, n. 5, p. 265–272, 2011b.

CHEN, S. et al. Estimating wide range Total Suspended Solids concentrations from MODIS 250-m imageries: An improved method. **ISPRS Journal of Photogrammetry and Remote Sensing**, v. 99, p. 58–69, 2015.

CHENG, C. et al. Estimation of Chlorophyll-a Concentration in Turbid Lake Using Spectral Smoothing and Derivative Analysis. **International Journal of Environmental Research and Public Health**, p. 2979–2994, 2013.

CICERELLI, E. **Estudo da ocorrência de cianobactérias no reservatório de Nova Avanhandava-SP por meio da inferência do pigmento ficocianina**. 2013. 174 p. Doctoral thesis (Cartographic Science) São Paulo State University, Presidente Prudente, SP.

COELHO, C. A. S.; CARDOSO, D. H. F.; FIRPO, M. A. F. Precipitation diagnostics of an exceptionally dry event in São Paulo, Brazil. **Theoretical and Applied Climatology**, p. 1–16, 2015.

COLLETT, L.J., GOULEVITCH, B.M., DANAHER, T.J. 1998. SLATS Radiometric Correction: A Semi-automated, Multi-stage Process for the Standardisation of Temporal and Spatial Radiometric Differences, Queensland Department of Natural Resources. Paper presented ate the 9th Australasian Remote Sensing and Photogrammetry Conference, Sydney, NSW, Australia, July 24, 1998.

COULTER, C. B.; KOLKA, R. K.; THOMPSON, J. A. Water Quality in Agricultural, Urban, and Mixed Land Use Watersheds. **Journal of the American Water Resources Association**, v. 40, n. 6, p. 1593–1601, 2004.

CUI, L. et al. Using remotely sensed suspended sediment concentration variation to improve management of Poyang Lake, China. **Lake and Reservoir Management**, v. 29, n. 1, p. 47-60, 2013.

CUNHA, D. G. F.; SABOGAL-PAZ, L. P.; KENNEDY, W. Land use influence on raw surface water quality and treatment costs for drinking supply in São Paulo State (Brazil). **Ecological Engineering**, v. 94, p. 516–524, 2016.

DALL'OLMO, G.; GITELSON, A. A.; RUNDQUIST, D. C. Towards a unified approach for remote estimation of chlorophyll-a in both terrestrial vegetation and turbid productive waters. **Geophysical Research Letters**, v. 30, n. 18, 2003.

DALL'OLMO, G.; GITELSON, A. A. Effect of bio-optical parameter variability on the remote estimation of chlorophyll-a concentration in turbid productive waters: experimental results. **Applied optics**, v. 44, n. 3, p. 412-422, 2005.

DEKKER, A. G. **Detection of optical water quality parameters for eutrophic waters by high resolution remote sensing**. 1993. 222 p. Doctoral thesis, University of Amsterdam.

DEKKER, A. G.; VOS, R. J.; PETERS, S. W. M. Comparison of remote sensing data, model results and in situ data for total suspended matter (TSM) in the southern Frisian lakes. **Science of the Total Environment**, v. 268, n. 1, p. 197-214, 2001.

DEKKER, A. G.; VOS, R. J.; PETERS, S. W. M. Analytical algorithms for lake water TSM estimation for retrospective analyses of TM and SPOT sensor data. **International Journal of Remote Sensing,** v. 23, n. 1, p. 15–35, 2002.

DELLAMANO-OLIVEIRA, M. J. et al. Carboidratos dissolvidos do reservatório de Barra Bonita (Estado de São Paulo, Brasil) e sua relação com as algas fitoplanctônicas abundantes. **Biota Neotropica**, v. 7, p. 59–66, 2007.

DOERFFER, R.; FISCHER, J. Concentrations of chlorophyll, suspended matter, and gelbstoff in case II waters derived from satellite coastal zone color scanner data with inverse modeling methods. **Journal of Geophysical Research: Oceans**, v. 99, n. C4, p. 7457-7466, 1994.

DOGLIOTTI, A. I. et al. A single algorithm to retrieve turbidity from remotely-sensed data in all coastal and estuarine waters. **Remote Sensing of Environment**, v. 156, p. 157–168, 2015.

DOXARAN, D. et al. Spectral signature of highly turbid waters Application with SPOT data to quantify suspended particulate matter concentrations. **Remote Sensing of Environment**, v. 81, p. 149–161, 2002.

DOXARAN, D.; CHERUKURU, N.; LAVENDER, S. J. Apparent and inherent optical properties of turbid estuarine waters: measurements, empirical quantification relationships, and modeling. **Applied Optics**, v. 45, n. 10, p. 2310–2324, 2006.

DOXARAN, D. et al. Estuarine, Coastal and Shelf Science Dynamics of the turbidity maximum zone in a macrotidal estuary (the Gironde, France): Observations from field and MODIS satellite data. **Estuarine, Coastal and Shelf Science**, v. 81, n. 3, p. 321–332, 2009.

D'SA, E. J.; MILLER, R. L. Bio-optical properties in waters influenced by the Mississippi River during low flow conditions. **Remote sensing of environment**, v. 84, n. 4, p. 538-549, 2003.

EGRÉ, D.; MILEWSKI, J. C. The diversity of hydropower projects. **Energy Policy**, v. 30, n. 14, p. 1225–1230, 2002.

ELEVELD, M. A. et al. Remotely sensed seasonality in the spatial distribution of sea-surface suspended particulate matter in the southern North Sea. **Estuarine, Coastal and Shelf Science**, v. 80, n. 1, p. 103–113, 2008.

EMPRESA BRASILEIRA DE PESQUISA AGROPECUÁRIA - EMBRAPA. 1999. **Sistema brasileiro de classificação de solos**. Rio de 882 Janeiro: 412 p.

EVANS, R. H.; GORDON, H. R. Coastal zone color scanner "system calibration": A retrospective examination. **Journal of Geophysical Research**, v. 99, n. C4, p. 7293, 1994.

FAN, C. Spectral Analysis of Water Reflectance for Hyperspectral Remote Sensing of Water Quailty in Estuarine Water. **Journal of Geoscience and Environment Protection**, v. 2, n. 2, p. 19–27, 2014.

FENG, L. et al. Remote Sensing of Environment Influence of the Three Gorges Dam on total suspended matters in the Yangtze Estuary and its adjacent coastal waters: Observations from MODIS. **Remote Sensing of Environment**, v. 140, p. 779–788, 2014.

GARVER, S. A.; SIEGEL, D. A. Inherent optical property inversion of ocean color spectra and its biogeochemical interpretation: 1. Time series from the Sargasso Sea. **Journal of Geophysical Research: Oceans**, v. 102, n. C8, p. 18607-18625, 1997.

GIARDINO, C. et al. Application of remote sensing in water resource management: the case study of Lake Trasimeno, Italy. **Water Resources Management**, v. 24, n. 14, p. 3885-3899, 2010.

GITELSON, A. The peak near 700 nm on radiance spectra of algae and water: relationships of its magnitude and position with chlorophyll concentration. **International Journal of Remote Sensing**, v. 13, n. 17, p. 3367–3373, 1992.

GOLTERMAN, H. L.; CLYMO, R. S.; OHNSTAD, M. A. M. **Methods for physical and chemical analysis of freshwater**. Oxford: Blackwell Scientific Publications. 213p, 1978.

GONS, H. J.; AUER, M. T. Some notes on water color in Keweenaw Bay (Lake Superior). **Journal of Great Lakes Research**, v. 30, p. 481-489, 2004.

GONS, H. J.; AUER, M. T.; EFFLER, S. W. MERIS satellite chlorophyll mapping of oligotrophic and eutrophic waters in the Laurentian Great Lakes. **Remote Sensing of Environment**, v. 112, n. 11, p. 4098-4106, 2008.

GORDON, H. R., MOREL, A. Y. **Remote Assessment of Ocean Color for Interpretation of Satellite Visible Imagery: A Review**, 114 pp., Springer-Verlag, New York, 1983.

GORDON, H. R. et al. A semianalytic radiance model of ocean color. **Journal of Geophysical Research: Atmospheres**, v. 93, n. D9, p. 10909-10924, 1988.

GORDON, H. R. a methodology for dealing with broad spectral. **Applied Optics**, v. 34, n. 36, p. 8363–8374, 1995.

GORDON, H. R.; BROWN, O. B.; JACOBS, M. M. Computed Relationships Between the Inherent and Apparent Optical Properties of a Flat Homogeneous Ocean. **Applied Optics**, v. 14, n. 2, p. 417–427, 1975.

GOULD, R. W.; ARNONE, R. A.; SYDORT, M. Absorption, Scattering, and Remote-Sensing Reflectance Relationships in Coastal Waters: Testing a New Inversion Algorithm. **Journal of Coastal Research**, v. 17, n. 2, p. 328–341, 2001.

GREEN, S. A.; BLOUGH, N. V. Optical absorption and fluorescence properties of chromophoric dissolved organic matter in natural waters. **Atlantic**, v. 39, 1994.

HAN, B. et al. Development of a Semi-Analytical Algorithm for the Retrieval of Suspended Particulate Matter from Remote Sensing over Clear to Very Turbid Waters. **Remote Sensing**, v. 8, n. 3, p. 211, 2016.

HAN, Z.; JIN, Y. -Q.; YUN, C. -X. Suspended sediment concentrations in the Yangtze River estuary retrieved from the CMODIS data. **International Journal of Remote Sensing**, v. 27, n. 19, p. 4329–4336, 2006.

HELMS, J. R. et al. Absorption spectral slopes and slope ratios as indicators of molecular weight, source, and photobleaching of chromophoric dissolved organic matter. **Limnology and Oceanography**, v. 53, n. 3, p. 955-969, 2008.

HENRY, R. et al. Primary production and effects of enrichment with nitrate and phosphate on phytoplankton in the Barra Bonita Reservoir (State of São Paulo, Brazil). **Internationale Revue der gesamten Hydrobiologie und Hydrographie**, v. 70, n. 4, p. 561-573, 1985.

HU, C. et al. Assessment of estuarine water-quality indicators using MODIS medium-resolution bands: Initial results from Tampa Bay, FL. **Remote Sensing of Environment**, v. 93, n. 3, p. 423–441, 2004.

IM, N. et al. Monitoring Land Use and Land Cover Effects on Water Quality in Cheung Ek Lake using ASTER Images. **American Journal of Environmental Sciences**, v. 11, n. 1, p. 1, 2015.

JIANG, X. et al. Application of MODIS data in monitoring suspended sediment of Taihu Lake, China. **Chinese Journal of Oceanology and Limnology**, v. 27, n. 3, p. 614–620, 2009.

JOLLIFF, J. K. et al. Summary diagrams for coupled hydrodynamic-ecosystem model skill assessment. **Journal of Marine Systems**, v. 76, n. 1–2, p. 64–82, 2009.

JONES, I. D.; ELLIOTT, J. A. Modelling the effects of changing retention time on abundance and composition of phytoplankton species in a small lake. **Freshwater Biology**, v. 52, n. 6, p. 988–997, 2007.

JORGENSEN, Sven Erik; TUNDISI, Jose Galizia; TUNDISI, Takako Matsumura. **Handbook of inland aquatic ecosystem management**. CRC Press, 2012.

KHAN, S. J. et al. Extreme weather events: Should drinking water quality management systems adapt to changing risk profiles? **Water Research**, v. 85, p. 124–136, 2015.

KIRK, J. T. **Light and photosynthesis in aquatic ecosystems**. Cambridge university press, 1994.

KONG, J. et al. A Semi-Analytical Model for Remote Sensing Retrieval of Suspended Sediment Concentration in the Gulf of Bohai, China. **Remote Sensing**, v. 7, n. 5, p. 5373–5397, 28 abr. 2015a.

KONG, J. et al. An optimal model for estimating suspended sediment concentration from Landsat TM images in the Caofeidian coastal waters. **International Journal of Remote Sensing**, v. 36, n. 19–20, p. 5257–5272, 18 out. 2015b.

KUMAR, A. et al. Remote monitoring of sediment dynamics in a coastal lagoon: Long-term spatio-temporal variability of suspended sediment in Chilika. **Estuarine, Coastal and Shelf Science**, v. 170, p. 155-172, 2016.

KUTSER, T. et al. Operative monitoring of the extent of dredging plumes in coastal ecosystems using MODIS satellite imagery. **Journal of Coastal Research**, v. 50, p. 180-184, 2007.

KUTSER, T. The possibility of using the Landsat image archive for monitoring long time trends in coloured dissolved organic matter concentration in lake waters. **Remote Sensing of Environment**, v. 123, p. 334–338, 2012.

LE, C. et al. Inherent and apparent optical properties of the complex estuarine waters of Tampa Bay: What controls light? **Estuarine, Coastal and Shelf Science**, v. 117, p. 54–69, 2013.

LE, C. et al. Relation between inherent optical properties and land use and land cover across Gulf Coast estuaries. **Limnology and Oceanography**, v. 60, n. 3, p. 920–933, 2015.

LE, C. F. et al. Validation of a quasi-analytical algorithm for highly turbid eutrophic water of meiliang bay in Taihu Lake, China. **IEEE Transactions on Geoscience and Remote Sensing**, v. 47, n. 8, p. 2492–2500, 2009a.

LE, C. et al. Specific absorption coefficient and the phytoplankton package effect in Lake Taihu, China. **Hydrobiologia**, v. 619, n. 1, p. 27–37, 2009b.

LEE, Z. et al. **An update of the quasi-analytical algorithm (QAA_v5).** International Ocean Color Group Software Report, p. 1-9, 2009. Available in: <http://www.ioccg.org/groups/Software_OCA/QAA_v5.pdf.> Access in: 15 jan 2015.

LEE, Z. et al. Model for the interpretation of hyperspectral remote-sensing reflectance. **Applied optics**, v. 33, n. 24, p. 5721–5732, 1994.

LEE, Z. et al. Hyperspectral remote sensing for shallow waters. I. A semianalytical model. **Applied optics**, v. 37, n. 27, p. 6329–6338, 1998.

LEE, Z. et al. Uncertainties of optical parameters and their propagations in an analytical ocean color inversion algorithm. **Applied Optics**, v. 49, n. 3, p. 369–381, 2010.

LEE, Z. et al. **Update of the Quasi-Analytical Algorithm (QAA_v6)**. 2014. Available in: <http://www.ioccg.org/groups/Software_OCA/QAA_v6_2014209.pdf).>. Access in: 05 jan 2015.

LEE, Z. et al. Secchi disk depth: A new theory and mechanistic model for underwater visibility. **Remote Sensing of Environment**, v. 169, p. 139-149, 2015.

LEE, Z.; CARDER, K. L.; ARNONE, R. A. Deriving inherent optical properties from water color: a multiband quasi-analytical algorithm for optically deep waters. **Applied Optics**, v. 41, n. 27, p. 5755–5772, 2002.

LEE, Z.; HU, C. Global distribution of Case-1 waters: An analysis from SeaWiFS measurements. **Remote Sensing of Environment**, v. 101, n. 2, p. 270–276, 2006.

LI, S. et al. Water quality in relation to land use and land cover in the upper Han River Basin, China. **Catena**, v. 75, n. 2, p. 216–222, 2008.

LI, S. et al. Evaluation of the Quasi-Analytical Algorithm (QAA) for Estimating Total Absorption Coefficient of Turbid Inland Waters in Northeast China. **IEEE Journal of Selected Topics in Applied Earth Observations and Remote Sensing**, p. 1–15, 2016.

LIU, C. et al. Quantitative modeling of suspended sediment in middle Changjiang River from Modis. **Chinese Geographical Science**, v. 16, n. 1, p. 79–82, 2006.

LOISELLE, S. A. et al. The optical characterization of chromophoric dissolved organic matter using wavelength distribution of absorption spectral slopes. **Limnology and Oceanography**, v. 54, n. 2, p. 590-597, 2009.

LOOS, E. A. **Optical Properties of the Waters of the Strait of Georgia, BC, Canada**. 2009. 124 p. Doctoral thesis (Geography), University of Victoria, Victoria.

LUZIA, A. P. **Limnologia e grau de trofia dos reservatórios em cascata do rio Tietê (médio e baixo Tietê, São Paulo).** 2004. 120 p. Master dissertation (Environmental Engineer). Universidade de São Paulo, São Carlos, SP.

MARITORENA, S.; SIEGEL, D. A.; PETERSON, A. R. Optimization of a semianalytical ocean color model for global-scale applications. **Applied Optics**, v. 41, n. 15, p. 2705-2714, 2002.

MATTHEWS, M. W.; BERNARD, S. Characterizing the absorption properties for remote sensing of three small optically-diverse South African reservoirs. **Remote Sensing**, v. 5, n. 9, p. 4370-4404, 2013.

MCFEETERS, S. K. The use of the Normalized Difference Water Index (NDWI) in the delineation of open water features. **International Journal of Remote Sensing**, v. 17, n. 7, p. 1425–1432, 1996.

MELER, J.; OSTROWSKA, M.; STOŃ-EGIERT, J. Seasonal and spatial variability of phytoplankton and non-algal absorption in the surface layer of the Baltic. **Estuarine, Coastal and Shelf Science**, v. 180, p. 123–135, 2016.

MERTEN, G. H.; MINELLA, J. PG. The expansion of Brazilian agriculture: soil erosion scenarios. **International Soil and Water Conservation Research**, v. 1, n. 3, p. 37-48, 2013.

MILLER, R. L.; MCKEE, B. A. Using MODIS Terra 250 m imagery to map concentrations of total suspended matter in coastal waters. **Remote sensing of Environment**, v. 93, n. 1, p. 259-266, 2004.

MISHRA, D. R.; MISHRA, S. Plume and bloom: effect of the Mississippi River diversion on the water quality of Lake Pontchartrain. **Geocarto International**, v. 25, n. 7, p. 555-568, 2010.

MISHRA, S. et al. Quantifying cyanobacterial phycocyanin concentration in turbid productive waters: A quasi-analytical approach. **Remote Sensing of Environment**, v. 133, p. 141–151, 2013.

MISHRA, S.; MISHRA, D. R. Normalized difference chlorophyll index: A novel model for remote estimation of chlorophyll-a concentration in turbid productive waters. **Remote Sensing of Environment**, v. 117, p. 394–406, 2012.

MISHRA, S.; MISHRA, D. R.; LEE, Z. Bio-Optical Inversion in Highly Turbid and Cyanobacteria-Dominated Waters. **IEEE Transactions on Geoscience and Remote Sensing**, v. 52, n. 1, p. 375–388, 2014.

MOBLEY, C. D. Estimation of the remote-sensing reflectance from above-surface measurements. **Applied Optics**, v. 38, n. 36, p. 7442–7455, 1999.

MOORE, G. F.; AIKEN, J.; LAVENDER, S. J. The atmospheric correction of water colour and the quantitative retrieval of suspended particulate matter in Case II waters: application to MERIS. **International Journal of Remote Sensing**, v. 20, n. 9, p. 1713-1733, 1999.

MOREL, A.; PRIEUR, L. Analysis of variations in ocean color. **Limnology and oceanography**, v. 22, n. 4, p. 709-722, 1977.

MOREL, A. Y.; GORDON, H. R. Report of the working group on water color. **Boundary-Layer Meteorology**, v. 18, n. 3, p. 343-355, 1980.

MOREL, A. In-water and remote measurements of ocean color. **Boundary-Layer Meteorology**, v. 18, n. 2, p. 177-201, 1980.

MOREL, A.; BRICAUD, A. Inherent optical properties of algal cells including picoplankton: theoretical and experimental results. **Can. Bull. Fish. Aquat. Sci**, v. 214, p. 521-559, 1986.

MOREL, A.; MARITORENA, S. Bio-optical properties of oceanic waters- A reappraisal. **Journal of Geophysical research**, v. 106, n. C4, p. 7163-7180, 2001.

MOURI, G.; TAKIZAWA, S.; OKI, T. Spatial and temporal variation in nutrient parameters in stream water in a rural-urban catchment, Shikoku, Japan: Effects of land cover and human impact. **Journal of Environmental Management**, v. 92, n. 7, p. 1837-1848, 2011.

MUELLER, J. L., 2000. In-water radiometric profile measurements and data analysis protocols. In: Fargion, G.S., Mueller, 944 J.L. (Eds.), **Ocean Optics Protocols for Satellite Ocean Color Sensor Validation**. Goddard Space Flight Center, 945 Greenbelt, Maryland, pp. 87–97, 2000.

NAIK, P. et al. Light absorption properties of southeastern Bering Sea waters: Analysis, parameterization and implications for remote sensing. **Remote Sensing of Environment**, v. 134, p. 120–134, 2013.

NASCIMENTO, R. F. F. **Utilização de dados MERIS e in situ para a caracterização bio-óptica do reservatório de Itumbiara, GO**. 2010. 115p. (Master on Remote Sensing). National Institute for Space Research, Sao Jose dos Campos, SP.

NECHAD, B.; RUDDICK, K. G.; PARK, Y. Remote Sensing of Environment Calibration and validation of a generic multisensor algorithm for mapping of total suspended matter in turbid waters. **Remote Sensing of Environment**, v. 114, n. 4, p. 854–866, 2010.

NOVO, E. M. L. M.; STEFFEN, C. A.; ZUCCARI FERNANDES BRAGA, C. Results of a laboratory experiment relating spectral reflectance to total suspended solids. **Remote Sensing of Environment**, v. 36, n. 1, p. 67–72, 1991.

ODERMATT, D. et al. Remote Sensing of Environment Review of constituent retrieval in optically deep and complex waters from satellite imagery. **Remote Sensing of Environment**, v. 118, p. 116–126, 2012.

OGASHAWARA, I. et al. A performance review of reflectance based algorithms for predicting phycocyanin concentrations in inland waters. **Remote Sensing**, v. 5, n. 10, p. 4774-4798, 2013.

OGASHAWARA, I. et al. Performance Analysis of MODIS 500-m Spatial Resolution Products for Estimating Chlorophyll-a Concentrations in Oligo- to Meso-Trophic Waters Case Study: Itumbiara Reservoir, Brazil. **Remote Sensing**, v. 6, n. 2, p. 1634–1653, 2014.

OGASHAWARA, I. Terminology and classification of bio-optical algorithms. **Remote Sensing Letters**, v. 6, n. 8, p. 613–617, 2015.

OGASHAWARA, I. et al. Re-parameterization of a quasi-analytical algorithm for colored dissolved organic matter dominant inland waters. **International Journal of Applied Earth Observation and Geoinformation**, v. 53, p. 128–145, 2016.

OLMANSON, L.G.; BREZONIK, P.L.; BAUER, M.E. Evaluation of medium to low resolution satellite imagery for regional lake water quality assessments. **Water Resources Research**, v. 47, n. 9, p. 1–14, 2011.

OLMANSON, L. G.; BREZONIK, P. L.; BAUER, M. E. Airborne hyperspectral remote sensing to assess spatial distribution of water quality characteristics in large rivers: The Mississippi River and its tributaries in Minnesota. **Remote Sensing of Environment**, v. 130, p. 254–265, 2013.

ONDRUSEK, M. et al. The development of a new optical total suspended matter algorithm for the Chesapeake Bay. **Remote Sensing of Environment**, v. 119, p. 243-254, 2012.

ORGANELLI, E. et al. Remote Sensing of Environment Retrieval of Colored Detrital Matter (CDM) light absorption coefficients in the Mediterranean Sea using field and satellite ocean color radiometry: Evaluation of bio-optical inversion models. **Remote Sensing of Environment**, v. 186, p. 297–310, 2016.

PAERL, H. W. et al. Controlling harmful cyanobacterial blooms in a hyper-eutrophic lake (Lake Taihu, China): The need for a dual nutrient (N & P) management strategy. **Water Research**, v. 45, n. 5, p. 1973–1983, 2011.

PALMER, S. C. J.; KUTSER, T.; HUNTER, P. D. Remote Sensing of Environment Remote sensing of inland waters: Challenges, progress and future directions. **Remote Sensing of Environment**, v. 157, p. 1–8, 2015.

PANHOTA, R. S.; BIANCHINI JR., I. Potential cycling of organic matter in a eutrophic reservoir (Barra Bonita, SP - Brazil). **Acta Limnologica Brasiliensia**, v. 15, n. 2, p. 1–11, 2003.

PANIGRAHI, S. et al. Variability of nutrients and phytoplankton biomass in a shallow brackish water ecosystem (Chilika Lagoon, India). **Limnology**, v. 10, n. 2, p. 73–85, 24 ago. 2009.

PARK, E.; LATRUBESSE, E. M. Modeling suspended sediment distribution patterns of the Amazon River using MODIS data. **Remote Sensing of Environment**, v. 147, p. 232-242, 2014.

PELLOQUIN, C., NIEKE, J. SENTINEL-3 spectral response functions for optical instruments (version CDR). 970 Technical Note. 1–4, 2012.

PERBICHE-NEVES, G.; FERREIRA, R.; NOGUEIRA, M. Phytoplankton structure in two contrasting cascade reservoirs (Paranapanema River, Southeast Brazil). **Biologia**, v. 66, n. 6, 2011.

PERBICHE-NEVES, G.; NOGUEIRA, M. G. Reservoir design and operation: effects on aquatic biota—a case study of planktonic copepods. **Hydrobiologia**, v. 707, n. 1, p. 187–198, 2013.

PEREIRA FILHO, W. et al. Influência de reservatórios em cascata nos dados de reflectância e de limnologia - Reservatórios de Passo Real e Dona Francisca, Rio Jacuí – RS. Anais XIV Simpósio Brasileiro de Sensoriamento Remoto. **Anais**...Natal: 2009

PERKINS, M. et al. Light absorbing components in the Finger Lakes of New York. **Fundamental and Applied Limnology/Archiv für Hydrobiologie**, v. 173, n. 4, p. 305-320, 2009.

PETESSE, M. L.; PETRERE JR, M.; AGOSTINHO, Â. A. Defining a fish bio-assessment tool to monitoring the biological condition of a cascade reservoirs system in tropical area. **Ecological Engineering**, v. 69, p. 139–150, ago. 2014.

PETUS, C. et al. Estimating turbidity and total suspended matter in the Adour River plume (South Bay of Biscay) using MODIS 250-m imagery. **Continental Shelf Research**, v. 30, n. 5, p. 379-392, 2010.

POPE, R. M.; FRY, E. S. Pure water. II. Integrating cavity measurements. **Applied Optics**, 1997.

PRADO, R.B. **Geotecnologias aplicadas à análise espaço temporal do uso e cobertura da terra e qualidade da água do reservatório de Barra Bonita, SP, como suporte à gestão de recursos hídricos**. 2004. 197 p. (Doctoral dissertation in Engineer) – University of São Paulo, São Carlos.

QIN, Y. et al. Validity of SeaDAS water constituent's retrieval algorithms in Australian tropical coastal waters. **Geophysical Research Letters**, v. 34, n. 21, 2007.

RIBEIRO FILHO, R. A. et al. Itaipu Reservoir limnology: eutrophication degree and the horizontal distribution of its limnological variables. **Brazilian Journal of Biology**, v. 71, n. 4, p. 889-902, 2011.

RIDDICK, C. A. et al. Spatial variability of absorption coefficients over a biogeochemical gradient in a large and optically complex shallow lake. **Journal of Geophysical Research: Oceans**, v. 120, n. 10, p. 7040-7066, 2015.

RITCHIE, J. C.; ZIMBA, P. V; EVERITT, J. H. Remote Sensing Techniques to Assess Water Quality. **Photogrammetric Engineering & Remote Sensing**, v. 69, n. 6, p. 695–704, 2003.

RITTER, W. F.; SHIRMOHAMMADI, A. (Ed.). **Agricultural nonpoint source pollution: watershed management and hydrology**. CRC Press, 2000.

ROBINSON, C. T. et al. Spatial relationships between land-use, habitat, water quality and lotic macroinvertebrates in two Swiss catchments. **Aquatic Sciences**, v. 76, n. 3, p. 375–392, 2014.

RODGHER, S. et al. Limnological and ecotoxicological studies in the cascade of reservoirs in the Tietê River (São Paulo, Brazil). **Brazilian journal of biology = Revista brasileira de biologia**, v. 65, n. 4, p. 697–710, 2005.

RODRIGUES, T. et al. Spatial and temporal variations of the inherent optical properties in a tropical cascading reservoir system. **Modeling Earth Systems and Environment**, v. 2, n. 2, p. 1-9, 2016a.

RODRIGUES, T. W. P. et al. Sampling design in reservoirs based on Landsat-8/OLI images: a case study in Nova Avanhandava reservoir (São Paulo State, Brazil). **Boletim de Ciências Geodésicas**, v. 22, n. 2, p. 303, 2016b.

RODRÍGUEZ-GUZMÁN, V.; GILBES-SANTAELLA, F. Using MODIS 250 m imagery to estimate total suspended sediment in a tropical open bay. **International journal of systems applications, engineering & developmen**t, v. 1, n. 3, p. 36-44, 2009.

ROESLER, C. S.; PERRY, M. J.; CARDER, K. L. Modeling in situ phytoplankton absorption from total absorption spectra in productive inland marine waters. **Limnology and Oceanography**, v. 34, n. 8, p. 1510–1523, 1989.

ROTTA, L. H. S. et al. Analyzing the status of submerged aquatic vegetation using novel optical parameters. **International Journal of Remote Sensing**, v. 37, n. 16, p. 3786–3810, 2016.

SANDES, M. A. L. **Flutuações de fatores ecológicos, composição e biomassa do fitoplâncton em curto período de tempo no reservatório Álvaro de Souza Lima (Bariri, SP)**. 1990. 133 p. Master dissertation. University of São Paulo, São Carlos, SP.

SANTOS, R. M. **Estrutura das comunidades fitoplanctônica e zooplanctônica, com ênfase na produção secundária do zooplâncton, e fatores ambientais relacionados nos reservatórios do Baixo Rio Tietê, SP**. 2010. 382 p. Master dissertation (Ecology and Natural Resources), Federal University of São Carlos, São Carlos, SP.

SASAKI, H. et al. Seasonal variation of absorption by particles and colored dissolved organic matter (CDOM) in Funka Bay, southwestern Hokkaido, Japan. **Estuarine, Coastal and Shelf Science**, v. 64, n. 2–3, p. 447–458, 2005.

SATHYENDRANATH, S. et al. Remote sensing of phytoplankton pigments: A comparison of empirical and theoretical approaches. **International Journal of Remote Sensing**, v. 22, n. 2–3, p. 249–273, 2001.

SATHYENDRANATH, S.; LAZZARA, L.; PRIEUR, L. Variations in the spectral values of specific absorption of phytoplankton. **Limnology and Oceanography**, v. 32, n. 2, p. 403–415, 1987.

SHANMUGAM, P. et al. An Evaluation of Inversion Models for Retrieval of Inherent Optical Properties from Ocean Color in Coastal and Open Sea Waters around Korea. **Journal of Oceanography**, v. 66, p. 815–830, 2010.

SHANMUGAM, P. et al. A New Inversion Model to Retrieve the Particulate Backscattering in Coastal/Ocean Waters. **IEEE Transactions on Geoscience and Remote Sensing**, v. 49, n. 6, p. 2463–2475, 2011.

SHEN, F. et al. Satellite Estimates of Wide-Range Suspended Sediment Concentrations in Changjiang (Yangtze) Estuary Using MERIS Data. **Estuaries and Coasts**, v. 33, n. 6, p. 1420–1429, 2010.

SHI, K. et al. Long-term remote monitoring of total suspended matter concentration in Lake Taihu using 250m MODIS-Aqua data. **Remote Sensing of Environment**, v. 164, p. 43-56, 2015.

SIMIS, S. G. H.; PETERS, S. W. M.; GONS, H. J. Remote sensing of the cyanobacterial pigment phycocyanin in turbid inland water. **Limnology and Oceanography**, v. 50, n. 1, p. 237–245, 2005.

SIPELGAS, L.; RAUDSEPP, U.; KÕUTS, T. Operational monitoring of suspended matter distribution using MODIS images and numerical modelling. **Advances in Space Research**, v. 38, n. 10, p. 2182-2188, 2006.

SMITH, R. C.; BAKER, K. S. Optical properties of the clearest natural waters (200-800 nm). **Applied Optics**, v. 20, n. 2, p. 177–184, 1981.

SMITH, W. S.; ESPÍNDOLA, E. L. G.; ROCHA, O. Environmental gradient in reservoirs of the medium and low Tietê River: limnological differences through the habitat sequence. **Acta Limnologica Brasiliensia**, v. 26, n. 1, p. 73–88, mar. 2014.

SOARES, A; MOZETO, A A. Water Quality in the Tietê River Reservoirs (Billings, Barra Bonita, Bariri and Promissão, SP-Brazil) and Nutrient Fluxes across the Sediment-Water Interface (Barra Bonita). **Acta Limnologica Brasiliensia**, v. 18, n. 3, p. 247–266, 2006.

SOARES, M. C. S. et al. The effects of water retention time and watershed features on the limnology of two tropical reservoirs in Brazil. **Lakes and Reservoirs: Research and Management**, v. 13, n. 4, p. 257–269, 2008.

SONG, K. et al. Retrieval of total suspended matter (TSM) and chlorophyll-a (Chl-a) concentration from remote-sensing data for drinking water resources. **Environmental Monitoring and Assessment**, v. 184, n. 3, p. 1449–1470, 2012.

SONG, K. S. et al. Remote quantification of total suspended matter through empirical approaches for inland waters. **Journal of Environmental Informatics**, v. 23, n. 1, p. 23–36, 2014.

SOTERO-SANTOS, R. B. et al. Toxicity of a cyanobacteria bloom in Barra Bonita Reservoir (Middle Tietê River, São Paulo, Brazil). **Ecotoxicology and Environmental Safety**, v. 64, n. 2, p. 163–170, 2006.

SRICHANDAN, S. et al. Interannual and cyclone-driven variability in phytoplankton communities of a tropical coastal lagoon. **Marine pollution bulletin**, v. 101, n. 1, p. 39-52, 2015.

STRASKRABA, M. Vltava cascade as teaching grounds for reservoir limnology. **Water Science & Technology**, v. 30, n. 10, p. 289–297, 1994.

STRASKRABA, M.; TUNDISI, J. (Eds). 1999. Lake Biwa, Japan. **Reservoir Water Quality management** (1999). UNEP/ILEC Guidelines of Lake Management series, Vol. 9: 229 pp.

SVÁB, E. et al. Characterizing the spectral reflectance of algae in lake waters with high suspended sediment concentrations. **International Journal of Remote Sensing**, v. 26, n. 5, p. 919–928, 2005.

TANG, S. et al. Regional algorithms for remote-sensing estimates of total suspended matter in the Beaufort Sea. **International Journal of Remote Sensing**, v. 34, n. 19, p. 6562–6576, 2013.

TARRANT, P. E.; AMACHER, J. A.; NEUER, S. Assessing the potential of Medium-Resolution Imaging Spectrometer (MERIS) and Moderate-Resolution Imaging Spectroradiometer (MODIS) data for monitoring total suspended matter in small and intermediate sized lakes and reservoirs. **Water Resources Research**, v. 46, n. 9, 2010.

TASSAN, S.; FERRARI, G. M. An alternative approach to absorption measurements of aquatic particles retained on filters. **Limnology and Oceanography**, v. 40, n. 8, p. 1358–1368, 1995.

TASSAN, S.; FERRARI, G. M. Measurement of light absorption by aquatic particles retained on filters: determination of the optical pathlength amplification by the "transmittance-reflectance" method. **Journal of Plankton Research**, v. 20, n. 9, p. 1699–1709, 1998.

TASSAN, S.; FERRARI, G. M. A sensitivity analysis of the "Transmittance-Reflectance" method for measuring light absorption by aquatic particles. **Journal of Plankton Research**, v. 24, p. 757–774, 2002.

TAYLOR, K. E. Summarizing multiple aspects of model performance in a single diagram. **Journal of Geophysical Research: Atmospheres**, v. 106, n. D7, p. 7183-7192, 2001.

TILSTONE, G. et al. REVAMP, Regional Validation of MERIS Chlorophyll products in North Sea coastal waters, protocols. European Union FPV: EVG1 CT 2001 00049, 68 p, 2002.

TONG, S. T. Y.; CHEN, W. Modeling the relationship between land use and surface water quality. **Journal of Environmental Management**, v. 66, n. 4, p. 377–393, 2002.

TORLONI, C.E.C. et al. Produção pesqueira. Produção pesqueira e composição das capturas em reservatórios sob concessão da CESP nos rios Tietê, Paraná e Grande, no período de 1986 a 1991. CESP, São Paulo, 1993.

TU, J. Spatially varying relationships between land use and water quality across an urbanization gradient explored by geographically weighted regression. **Applied Geography**, v. 31, n. 1, p. 376–392, 2011.

TU, J. Spatial variations in the relationships between land use and water quality across an urbanization gradient in the watersheds of northern Georgia, USA. **Environmental Management**, v. 51, n. 1, p. 1–17, 2013.

TUNDISI, J. G.; MATSUMURA TUNDISI, T. **Limnology**. CRC Press, 2011.
TWARDOWSKI, M. S. et al. Modeling the spectral shape of absorption by chromophoric dissolved organic matter. **Marine Chemistry**, v. 89, n. 1–4, p. 69–88, 2004.

United States Geological Survey. Landsat Processing Details. 2014. Available in: <http://landsat.usgs.gov>. Access in: 10 jun 2015.

United States Geological Survey. Using the USGS Landsat 8 Product. 2013. Available in: <http://landsat.usgs.gov/Landsat8_Using_Product.php>. Access in:10 may 2015

VAROL, M. et al. Spatial and temporal variations in surface water quality of the dam reservoirs in the Tigris River basin, Turkey. **Catena**, v. 92, p. 11–21, 2012.

VERMOTE, E. F.; KOTCHENOVA, S. Atmospheric correction for the monitoring of land surfaces. **Journal of Geophysical Research**, v. 113, n. D23, p. 1–12, 2008.

VERMOTE, E. F.; KOTCHENOVA, S. Y.; RAY, J. P. M**ODIS surface reflectance user's guide. MODIS Land Surface Reflectance Science Computing Facility**, version, v. 1, 2011.

VILLAR, R. E. et al. A study of sediment transport in the Madeira River, Brazil, using MODIS remote-sensing images. **Journal of South American Earth Sciences**, v. 44, p. 45-54, 2013.

WACHHOLZ, F.; PEREIRA FILHO, W.; FILHO, A. P. Compartimentação aquática espectral dos reservatórios em cascata no alto Jacuí – RS Flávio. **Anais** XIV Simpósio Brasileiro de Sensoriamento Remoto. Anais...Natal: 2009

WANG, H. et al. Detecting the spatial and temporal variability of chlorophyll- a concentration and total suspended solids in Apalachicola Bay, Florida using MODIS imagery. **International Journal of Remote Sensing**, v. 31, n. 2, p. 439–453, 2010.

WANG, L. et al. Retrieval of total suspended matter from MODIS 250 m imagery in the Bohai Sea of China. **Journal of oceanography**, v. 68, n. 5, p. 719-725, 2012.

WANG, S. et al. MODIS-Based Radiometric Color Extraction and Classification of Inland Water with the Forel-Ule Scale: A Case Study of Lake Taihu. **IEEE Journal of Selected Topics in Applied Earth Observations and Remote Sensing**, v. 8, n. 2, p. 907–918, 2015.

WATANABE, F. et al. Parametrization and calibration of a quasi-analytical algorithm for tropical eutrophic waters. **ISPRS Journal of Photogrammetry and Remote Sensing**, v. 121, p. 28–47, 2016a.

WATANABE, F. et al. Drought can cause phytoplankton growth intensification in Barra Bonita reservoir. **Modeling Earth Systems and Environment**, v. 2, n. 3, p. 134, 2016b.

WELCH, E.B., LINDELL, T. **Ecological effects of wastewater: applied limnology and pollutant effects**, 2nd edition. 1030 Chapman & Hall, New York, 1992.

WU, G. et al. Absorption and backscattering coefficients and their relations to water constituents of Poyang Lake, China. **Applied Optics**, v. 50, n. 34, p. 6358–6368, 2011.

WU, G. et al. Comparison of MODIS-based models for retrieving suspended particulate matter concentrations in Poyang Lake, China. Int**ernational Journal of Applied Earth Observation and Geoinformation**, v. 24, p. 63–72, 2013.

YACOBI, Y. Z. et al. NIR-red reflectance-based algorithms for chlorophyll-a estimation in mesotrophic inland and coastal waters: Lake Kinneret case study. **Water Research**, v. 45, n. 7, p. 2428–2436, 2011.

YANG, W. et al. Retrieval of Inherent Optical Properties for Turbid Inland Waters from Remote-Sensing Reflectance. **IEEE Transactions on Geoscience and Remote Sensing**, v. 51, n. 6, p. 3761–3773, 2013.

YLÖSTALO, P.; KALLIO, K.; SEPPÄLÄ, J. Absorption properties of in-water constituents and their variation among various lake types in the boreal region. **Remote Sensing of Environment**, v. 148, p. 190-205, 2014.

XU, H. Modification of normalised difference water index (NDWI) to enhance open water features in remotely sensed imagery. **International Journal of Remote Sensing**, v. 27, n. 14, p. 3025–3033, 2006.

ZANATA, L. H. **Distribuição das populações de Cladocera (Branchiopoda) nos reservatórios do Médio e Baixo rio Tietê: uma análise espacial e temporal**. 2005. 304 p. Doctoral thesis (Environmental Engineer). University of São Paulo, São Carlos, SP.

ZAWADA, D. G. et al. Remote sensing of particle backscattering in Chesapeake Bay: A 6-year SeaWiFS retrospective view. **Estuarine, Coastal and Shelf Science**, v. 73, n. 3–4, p. 792–806, 2007.

ZHANG, M. et al. Retrieval of total suspended matter concentration in the Yellow and East China Seas from MODIS imagery. **Remote Sensing of Environment**, v. 114, n. 2, p. 392–403, 2010.

ZHANG, Y. et al. A study of absorption characteristics of chromophoric dissolved organic matter and particles in Lake Taihu, China. **Hydrobiologia**, v. 592, n. 1, p. 105–120, 2007.

ZHANG, Y. et al. Modeling Remote-Sensing Reflectance and Retrieving Chlorophyll-a Concentration in. **IEEE Transactions on Geoscience and Remote Sensing**, v. 47, n. 7, p. 1937–1948, 2009a.

ZHANG, Y. L. et al. Bio-optical properties and estimation of the optically active substances in Lake Tianmuhu in summer. **International Journal of Remote Sensing**, v. 30, n. 11, p. 2837–2857, 2009b.

ZHANG, Y. et al. The contribution of phytoplankton degradation to chromophoric dissolved organic matter (CDOM) in eutrophic shallow lakes: field and experimental evidence. **Water Research**, v. 43, n. 18, p. 4685-4697, 2009c.

ZHAO, H. et al. A study of sediment transport in a shallow estuary using MODIS imagery and particle tracking simulation. **International Journal of Remote Sensing**, v. 32, n. 21, p. 6653–6671, 2011.

ZHAO, J. et al. Influences of land use on water quality in a reticular river network area: A case study in Shanghai, China. **Landscape and Urban Planning**, v. 137, p. 20–29, 2015.

ZHU, W. et al. Estimation of chromophoric dissolved organic matter in the Mississippi and Atchafalaya river plume regions using above-surface hyperspectral remote sensing. **Journal of Geophysical Research**, v. 116, n. C2, p. C02011, 2011.